Optical fibre tweezers for trapping and manipulation of sub-micrometre particles

Sandra M. Rodrigues
Mestrado Integrado em Engenharia Física
Departamento de Física e Astronomia
2019

Orientador
Prof. Dr. Pedro A. S. Jorge, Faculdade de Ciências da Universidade do Porto e INESC TEC

Coorientador
Prof. Dr. Paulo V. S. Marques, Faculdade de Ciências da Universidade do Porto e INESC TEC
Prof. Dr. João P. S. Cunha, Faculdade de Engenharia da Universidade do Porto e INESC TEC

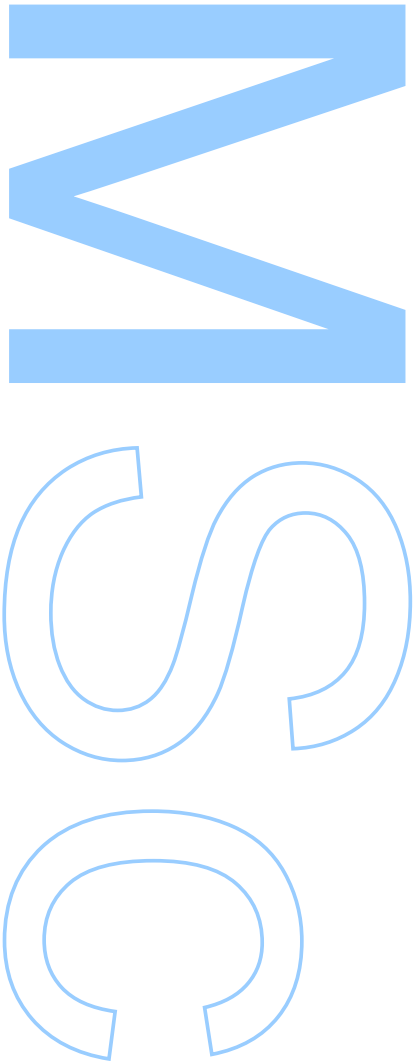
U.PORTO

FACULDADE DE CIÊNCIAS
UNIVERSIDADE DO PORTO

Todas as correções determinadas pelo júri, e só essas, foram efetuadas.

O Presidente do Júri,

Porto, _____/_____/_____



UNIVERSIDADE DO PORTO

MASTER THESIS

Optical fibre tweezers for trapping and manipulation of sub-micrometre particles

Author:
Sandra M. RODRIGUES

Supervisor:
Pedro JORGE

Co-supervisors:
Paulo MARQUES
João Paulo CUNHA

A thesis submitted in fulfilment of the requirements
for the degree of MSc. Engineering Physics

at the

Faculdade de Ciências da Universidade do Porto
Departamento de Física e Astronomia

December 9, 2019

" If you hold close to nature, to what is simple in it, to the small things people hardly see and which all of a sudden can become great and immeasurable; if you have this love for what is slight; and quite unassumingly, as a servent, seek to win the confidence of what seems poor - then everything will grow easier, more unified and somehow more conciliatory, not perhaps in intellect, which, amazed, remains a step behind, but in your deepest conciousness, whatchfulness and knowledge. "

Rainer Maria Rilke

Acknowledgements

This past year of my life has been heavily marked by this thesis. Having deprived me of a good amount of sleeping hours, it could have been much worse, if not for a wonderful group of people surrounding me, whom I would like to thank.

First of all, to Rita Ribeiro for walking me through the first steps I took in this world, way before this thesis was even a project. She showed me how amazing optical trapping can be and was always there when I needed.

To my supervisor, Dr Pedro Jorge, for always believing me, even when I did not. His guidance and perseverance allowed me to achieve my goals, while always leaving room for me to make my own choices on the path to follow. I would also like to thank my co-supervisors, Dr Paulo Marques and Dr João Paulo Cunha. To professor Paulo Marques thank you for the lessons, advice and frontality ever since the advanced lab classes.

To Joana Paiva, for although her name does not appear on the cover of this thesis, she was always there to guide me through this work and to debate many ideas. For her unshakable trust in me, words cannot thank you enough.

To Luís Coelho, for the restless support he provided me throughout this year. The advice, usually accompanied by a roast session, were many and crucial to this work. Thank you for all the time you took out of your day to help me and to fix the same equipment multiple times.

To Filipe Silva, for the tremendous help at the beginning of the experiments, the chemistry lessons and the nonsense conversations.

To all my colleagues from the Center of Applied Photonics at INESC-TEC with whom I shared the laboratories, and especially a big thanks to Luísa Mendonça, for always having a smile for me when I needed her.

To Raquel Queirós, that so kindly made herself available to guide me through my day at INL. To Enrique Carbó-Argibay and Oleksandr Bondarchuk from INL, for the kindness and patience they showed while helping me complete the fabrication of my tweezers.

To my parents, for all the sacrifices they have made so I could be where I am today. For always proving that hard work pays off and showing me the meaning of unconditional love.

To my brother, for the constant faith and support. You taught me to look further, to go beyond, to travel the world.

To my great uncles, Ana and Cândido, for everything they did for me these last couple of months.

And last, but by no means least, I could never go by without a little help from my friends. For all of you who have been there, putting up with me, for the many singing sessions, dinners, beers, concerts, sunsets and endless random conversations. I love you all.

UNIVERSIDADE DO PORTO

Abstract

Faculdade de Ciências da Universidade do Porto
Departamento de Física e Astronomia

MSc. Engineering Physics

Optical fibre tweezers for trapping and manipulation of sub-micrometre particles

by Sandra M. RODRIGUES

Over the last few decades, optical trapping has gained a central role, not only in the physics domain but especially in the natural sciences area. The majority of the optical instruments used nowadays to observe living cells are equipped with a trapping component. However, the majority of such components and professional setups are based on bulky and expensive equipment. The investigation group where this thesis was developed has been working, in the past years, on ways to make these tools smaller and cheaper and they have been successful so far. A versatile optical fibre based tool has been developed, making use of a polymeric lens-like structure built at the top of a cleaved fibre. Nonetheless, science always presents itself with new challenges, and with the recent discovery that exosomes can be used to diagnose and identify types of tumours, the group wanted to apply its expertise to the challenge of differentiation of these extracellular vesicles. Although the polymeric tweezers have proven effective in identifying the exosomes in solution by the collection of backscattered radiation, they cannot trap them as they have only a few tens to some hundreds of nanometres. So the idea for this thesis comes along to try to answer this limitation. To try to bring into the group a new technique that would allow the trapping of sub-micrometre particles. The hope was that we could apply such technique in the near future to the optical trapping and backscattered radiation collection of the exosomes, to try to improve the robustness of the differentiation technique.

A significant amount of techniques have already been developed to trap very small particles, most of them, however, focus on a standing planar configuration. As we wished to develop a fibre-based tool, that could be used in the setup already assembled at the lab, we opted for the development of SNOM like tips based on optical fibre to perform the

optical trap. These SNOM like tips were fabricated by tapering the extremity of an optical fibre, then coating it with gold and opening up a nanometre aperture at the taper's apex, through where the light could be transmitted.

We begin by presenting a state of the art of optical trapping at a nanoscale. First focusing on the theoretical principles of the trapping itself and then focusing on the different techniques and configurations that have been applied so far. As our main interest lays within the optical fibre application, the chapter ends with the presentation of some promising works in that area. Descriptions of the experimental methods used in the fabrication of the tweezers and the optical forces calculation are presented in chapter 2.

We present a computational study of the influence of the final tweezer geometry on the optical trapping capabilities, trying to predict which configurations will be better to trap the desired specimens. Using these configurations we were then able to trap polystyrene particles with diameters of $1\mu m$ and 500 nm. Optical forces and trap stiffnesses were measured.

A reasonable agreement was found between simulation and experimental results. However, we hope to be able to conduct more tests in the near future to better fundament these conclusions.

UNIVERSIDADE DO PORTO

Resumo

Faculdade de Ciências da Universidade do Porto
Departamento de Física e Astronomia

Mestrado Integrado em Engenharia Física

Pinças óticas em fibra para *trapping* e manipulação de partículas sub-micrometricas

por Sandra M. RODRIGUES

Ao longo das últimas décadas o aprisionamento óptico tem vindo a ganhar um papel central, não apenas no que às áreas da física diz respeito, mas especialmente no domínio das ciências naturais. A maioria dos instrumentos ópticos utilizados actualmente na observação de células vivas, vem já equipados com uma componente capaz de aprisionar uma célula individual. Contudo, a grande parte destas componentes, ou dos setups especializados são baseados em componentes caros e de elevadas dimensões. O grupo de investigação onde esta tese foi desenvolvida tem vindo, ao longo dos últimos anos, a desenvolver técnicas capazes de reduzir o tamanho desta tecnologia tornando-a simultaneamente mais barata. Neste sentido, foi desenvolvida uma ferramenta que consiste na fabricação de uma estrutura polimérica, que se assemelha a uma lente, no topo de uma fibra óptica clivada. Ferramenta esta capaz de aprisionar partículas. Ainda assim, a ciência traz sempre novos desafios, e com a recente descoberta de que os exossomas podem ser usados no diagnóstico de diferentes tumores, o grupo decidiu aplicar o seu conhecimento na análise e diferenciação destas vesículas extracelulares. Apesar das pontas poliméricas terem já demonstrado a sua capacidade de diferenciação dos exossomas, pela recolha e análise da radiação reflectida, quando estes estão em solução, as mesmas não são capazes de os imobilizar, de forma a recolher radiação de um espécime isolado, uma vez que estes têm apenas algumas dezenas, ou centenas de nanometros de diâmetro. Desta forma, a ideia desta tese surge para tentar dar resposta a esta limitação. Tentar introduzir no grupo uma técnica que nos permitisse aprisionar partículas mais pequenas, realizando simultaneamente a recolha da radiação reflectida.

Existe já uma quantidade significativa de técnicas desenvolvidas capazes de aprisionar partículas de dimensões inferiores a $1\mu m$, a maior parte delas baseadas em configurações

fixas e planares. O nosso objetivo era desenvolver uma ferramenta em fibra óptica, que nos permitisse continuar a usar o setup experimental que já tinha sido desenvolvido. Optamos então pelo desenvolvimento de pinças em tudo semelhantes às sondas utilizadas na microscopia de varrimento de campo próximo. O fabrico destas pinças consistiu então no etching de fibras óticas para que estas assumissem uma forma cónica. As fibras eram posteriormente cobertas com uma pequena camada de ouro, e mais tarde uma abertura nanométrica era produzida na extremidade do cone, de forma a que a luz pudesse ser transmitida.

Começamos então por apresentar o estado da arte da manipulação e aprisionamento óptico a uma escala nanométrica. Focando primeiro nos princípios teóricos do trapping e analisando depois diferentes técnicas e configurações aplicadas. Uma vez que o nosso principal interesse recai sobre a aplicação das fibras ópticas, o capítulo acaba com a apresentação de alguns trabalhos interessantes nessa área. Descrições dos métodos experimentais usados na fabricação das pinças e no cálculo das forças ópticas são apresentadas no capítulo 2.

Apresentamos um estudo computacional da influência da geometria das pinças nas capacidades de trapping, tentando prever quais serão as melhores configurações para aprisionar as partículas desejadas. Usando essas configurações fomos depois capazes de aprisionar e manipular partículas de poliestireno com diâmetros de $1\mu m$ e 500 nm. As forças ópticas exercidas nas partículas e a rigidez do trapping foram medidas.

Foi encontrada uma coincidência razoável entre simulações e resultados experimentais. Contudo, esperamos que no futuro seja possível a realização de mais testes, para melhor fundamentar esta concordância.

Contents

Acknowledgements v

Abstract vii

Resumo ix

Contents xi

List of Figures xiii

Glossary xvii

1 Introduction 1
- 1.1 The principles of optical trapping . . . 3
  - 1.1.1 Force calibration - stiffness determination . . . 5
- 1.2 Optical forces at a nanoscale . . . 6
- 1.3 Nano optical trapping . . . 8
  - 1.3.1 The first echos . . . 8
  - 1.3.2 Plasmonic nano optical tweezers . . . 9
    - 1.3.2.1 The self-induced back-action mechanism . . . 12
    - 1.3.2.2 Optical trapping with nanoholes . . . 13
    - 1.3.2.3 Thermal considerations . . . 17
  - 1.3.3 Other techniques . . . 18
  - 1.3.4 Optical fibre nanotweezers . . . 19
- 1.4 Outline of this work . . . 23

2 Experimental methods and tools 25
- 2.1 Chemical etching with HF acid . . . 25
  - 2.1.1 Sample preparation and experimental configuration . . . 27
- 2.2 E-beam evaporation . . . 28
  - 2.2.1 Sample preparation and assembling . . . 29
- 2.3 Focused ion-beam milling and scanning electron microscope system . . . 31
  - 2.3.1 Scanning electron microscope . . . 31
  - 2.3.2 Focused ion-beam milling . . . 32
  - 2.3.3 Sample preparation and assembling . . . 33
- 2.4 Measurement of optical trapping forces - the drag force method . . . 34

2.4.1 Data acquisition and processing . . . 35

3 A simulation-based study of the trapping forces at a nanoscale 37
3.1 COMSOL Multiphysics . . . 37
3.2 Force calculation method . . . 39
3.2.1 Python scripts . . . 40
3.3 A 3D view of the problem . . . 41
3.4 A 2D evaluation of the problem . . . 43
3.4.1 The influence of the taper angle on the transmitted field . . . 44
3.4.2 Results for 20º angled tapers . . . 46
3.4.2.1 A comparison with polymeric tips . . . 49
3.4.3 A detailed study of a 20º taper configuration . . . 50
3.4.3.1 P-polarization vs. s-polarization . . . 51
3.4.3.2 Comparing the force maps for different geometries . . . 53
3.4.4 How will the Cr layer afect the results? . . . 57
3.5 Discussion . . . 60

4 Tapered optical fibre tweezers 61
4.1 Fabrication . . . 61
4.1.1 The optimization of the etching process . . . 61
4.1.1.1 The tube etching method . . . 61
4.1.1.2 The Turner's method . . . 65
4.1.2 The gold coating . . . 68
4.1.3 Aperture milling . . . 72
4.2 Tweezers characterization . . . 75
4.2.1 Some observations on transmission . . . 77
4.2.2 Backscattering collection . . . 78
4.3 Optical trapping . . . 80
4.3.1 Optical trapping and signal acquisition setup . . . 80
4.3.2 Preliminary experiments . . . 81
4.3.2.1 Checking for thermal effects . . . 81
4.3.2.2 No trapping with large apertures - the dominance of the scattering force . . . 82
4.3.3 Optical trapping of polystyrene beads . . . 83
4.3.3.1 Experimental optical force measurement and stiffness determination . . . 86
4.4 Discussion . . . 91

5 Final remarks and future work 93

A Laser specifications 95

Bibliography 97

List of Figures

1.1 Geometrical representation of optical trapping forces. . . . 4
1.2 Schematics of a bulk optical tweezers setup. . . . 5
1.3 Scheme of the dipole. . . . 6
1.4 Spatial distributions of light intensity and forces as in reference [34]. . . . 9
1.5 Force distribution for a 50 nm dielectric particle from reference [36]. . . . 10
1.6 Different experimental configurations used for nano optical trapping. . . . 11
1.7 Exemples of nanostructured substrates fabricated with different techniques. 12
1.8 Aperture configuration and intensity results from reference [45]. . . . 13
1.9 Fluorescence emission from one single nano aperture and representation of a fluidic chamber from [49]. . . . 14
1.10 SEM images of the double-nanohole studied in reference [50]. . . . 15
1.11 Optical trapping setup and fluidic chamber from reference [50]. . . . 15
1.12 Optical transmission measurements from different types of nanoholes [50]. 16
1.13 Optical power transmitted through a double nanoaperture during the trapping of a single protein [27]. . . . 17
1.14 Other nano optical trapping techniques. . . . 18
1.15 Mode propagation in a tapered metal-coated optical fiber for an arbitrary wavelength [61]. . . . 20
1.16 Schematics of a SNOM and SIBA probes as in reference [64]. . . . 21
1.17 Bowtie nano apertures from references [65] and [66]. . . . 22
1.18 Schematics of the stripping process described in reference [71]. . . . 22

2.1 Scheme of optical fiber taper evolution during the etching process. . . . 26
2.2 Cone angle and cone length as a function of HF concentration [77]. . . . 27
2.3 Experimental configuration used for etching. . . . 28
2.4 Schematic representation of an e-beam vacuum evaporation chamber. . . . 28
2.5 Rotatory sample holder. . . . 29
2.6 Edwards Auto 306 electron beam evaporation system. . . . 30
2.7 FIB machine Helios NanoLab 450S DualBeam, from FEI company. . . . 31
2.8 Schemes of a SEM column and the interactions between particles. . . . 32
2.9 Scheme of the interaction between the ions and the sample. . . . 33
2.10 Preparation and assembling of the sample. . . . 34

3.1 COMSOL geometry used in simulations. . . . 38
3.2 3D electric field norm for a taper with d=a=600 nm. . . . 41
3.3 Electric field norm for planes xz and yz. . . . 42
3.4 Representation of the polarization vectors at the entrance of the taper. . . . 42

3.5 $|E|^2$ in the aperture exist plane: (left) two-dimensional-model SNOM and (right) ideal circular aperture [89]. . . . 43
3.6 Scheme of the taper's geometry. . . . 44
3.7 Intensity and intensity gradient for 20º tapers in both polarization planes. . 45
3.8 Electric field norm (s-pol) for tapers with $d = 1\mu m$, $a = 300nm$ and $d = 1\mu m$, $a = 850nm$. . . . 45
3.9 Electric field norm (p-pol) for tapers with $d = 1\mu m$, $a = 300nm$ and $d = 1\mu m$, $a = 850nm$. . . . 46
3.10 Intensity and intensity gradient for 30º tapers in both polarization planes. . 47
3.11 Intensity and intensity gradient for 40º tapers in both polarization planes. . 48
3.12 Intensity as a function of cone angle for a taper with $d = a = 200nm$. . . . 49
3.13 Electric field norm for a taper with $d = a = 200nm$ and cone angles of 30º and 40º. . . . 49
3.14 Electric field norm for a polymeric tip with $2.9\mu m$ radius. . . . 50
3.15 Electric field norm and force field map (s-pol) for a 20º taper with $d = a = 600nm$ for a polystyrene particle of 100nm. . . . 51
3.16 Electric field norm and force field map (p-pol) for a 20º taper with $d = a = 600nm$ for a polystyrene particle of 100nm. . . . 52
3.17 Electric field norm and force field map (s-pol) for a 20º taper with $d = a = 700nm$ for a polystyrene particle of 100nm. . . . 52
3.18 Electric field norm and force field map (p-pol) for a 20º taper with $d = a = 700nm$ for a polystyrene particle of 100nm. . . . 53
3.19 Force field maps for 500 nm polystyrene particles using tapers with $d = a = 600nm$ and $d = a = 700nm$. . . . 53
3.20 Electric field norm, in the s-polarized plane, for a 20º angled taper with apex and aperture diameters of 500 nm. . . . 54
3.21 Force field maps for a taper of $d = a = 500nm$ acting on 100 nm and 500 nm polystyrene particles. . . . 54
3.22 Electric field norm, in the s-polarized plane, for a 20º angled taper with apex and aperture diameters of 800 nm. . . . 55
3.23 Force field maps for a taper of $d = a = 800nm$ acting on 100 nm and 500 nm polystyrene particles. . . . 55
3.24 Electric field norm, in the s-polarized plane, for a 20º angled taper with apex and aperture diameters of 900 nm. . . . 56
3.25 Force field maps for a taper of $d = a = 900nm$ acting on 100 nm and 500 nm polystyrene particles. . . . 56
3.26 Electric field norm, in the s-polarized plane, for a 20º angled taper with apex and aperture diameters of 1000 nm. . . . 57
3.27 Force field maps for a taper of $d = a = 1000nm$ acting on 100 nm and 500 nm polystyrene particles. . . . 58
3.28 Electric field norm, in the s-polarized plane, for a 20º angled taper with apex and aperture diameters of 1000 nm and 250 nm, respectively. . . . 58
3.29 Force field maps for a taper of $d = 1000nm$ and $a = 250nm$ acting on 100 nm and 500 nm polystyrene particles. . . . 58
3.30 Electric field norm (s-pol) for a 20º taper with (A) $d = a = 900nm$ and (B) $d = a = 1000nm$ with a chromium layer. . . . 59
3.31 Electric field norm (p-pol) for a 20º taper with (A) $d = a = 600nm$ and (B) $d = a = 700nm$ with a chromium layer. . . . 59

4.1 Optical fibre taper obtained from the first etching test. . . . 62
4.2 Etching time study for 48% HF. . . . 62
4.3 Etching time study for 30% HF. . . . 63
4.4 Etching time study for 30% HF: tube etch *vs* Tuner's method. . . . 64
4.5 Set of tapers fabricated under the same conditions. . . . 65
4.6 Evolution of taper angles with different oils. . . . 66
4.7 Oddly shaped optical fibres resulting from chemical etching. . . . 67
4.8 Tapers fabricated with the optimized etching process. . . . 68
4.9 SEM images of gold coated taper labeled as number 41. . . . 69
4.10 EDS results for zones 1 (A) and 4 (B) of taper 41. . . . 70
4.11 SEM images of gold coated taper labeled as number 37. . . . 70
4.12 EDS results for zones 1 (A) and 2 (B) of taper 37. . . . 71
4.13 SEM images of gold coated tapers. . . . 72
4.14 SEM images of a femtosecond laser beam cut to a taper. . . . 73
4.15 EDS spectrum of zone 1 identified in figure 4.14 (C). . . . 73
4.16 SEM images of FIB milling results. . . . 74
4.17 SEM images of the tweezers used in the optical trapping tests. . . . 75
4.18 SEM and EDS results from taper 41. . . . 76
4.19 Tweezers maximum intensity outputs as a function of wavelength. . . . 77
4.20 Collected power as a function of tweezer's angle of incidence in the solution. 79
4.21 Optical trapping setup. . . . 80
4.22 Sequence of particle displacement. . . . 82
4.23 Sequence of particle displacement. . . . 83
4.24 Output optical field of tweezer 6. . . . 83
4.25 Sequence of images of the optical trapping of a $1\mu m$ polystyrene bead. . . . 84
4.26 Signal collected during the optical trapping of a $1\mu m$ polystyrene bead. . . . 85
4.27 Cluster of particles in front of the tweezer. . . . 85
4.28 Sequence of images of the optical trapping of a 500 nm polystyrene bead. . . . 86
4.29 Signal collected during the optical trapping of a 500 nm polystyrene bead. . . . 87
4.30 Laser characterization. . . . 88
4.31 Trajectory's Langevin fit and optical force plots. . . . 88
4.32 Optical force as a function of the displacement relative to the stable trapping position. . . . 89
4.33 Exemples of collected signal. . . . 90
4.34 Collected signal of a trapping event and its exponential fit. . . . 91

A.1 Laser specifications. . . . 95

Glossary

NFT	Near Field Trapping
SPR	Surface Plasmon Resonance
SPP	Surface Plasmon Polariton
LSP	Localized Surface Plasmon
FIB	Focused Ion Beam
SIBA	Self-Induced Back-Action
SNOM	Scanning Near-field Optical Microscopy
HF	Hydrofluoric Acid
EOT	Extraordinary Optical Transmission
SEM	Scanning Electron Microscope
LMIS	Liquid Metal Ion Source
EDS	Energy Dispersive Spectroscopy

Chapter 1

Introduction

From the invention of the microscope to the development of the first laser source [1], some discoveries paved the way to the question "What if we could use light to control and manipulate other objects?".

Arthur Ashkin was the pioneer in the field of optical trapping. In his paper from 1970 [2], he reported the trapping and acceleration of a microparticle between two counter-propagating laser beams. It took him yet another 16 years to achieve the same result using a single tightly focused laser beam [3]. A technique known today as *optical tweezers*. Thanks to its contributions to the field of optical trapping and all the possibilities that it has opened, Dr Ashkin was awarded the 2018 Nobel prize in Physics.

Motivation

In the decades that have passed since it was first discovered, optical trapping has evolved and became a standard technique in a variety of fields, especially in medical-related ones. The manipulation of single cells without any mechanical contact greatly diminishes the risk of cell damage during tests. However, the setups available nowadays are based on bulky optics, making them big, expensive and hard to displace. In the efforts to develop a more compact and less expensive solution, some groups began exploring optical fibres as a way to guide the light to the particle, to trap it. Our team, at the Center of Applied Photonics (CAP) at INESC TEC was one of those groups, and in the past years has been working on ways to use optical fibre with a polymeric lens-like structure built on top [4–6]. That structure is responsible for focusing the light travelling on the fibre and thus enabling the trapping of micrometre-sized particles. With the advance of the research, the group was also able to use the same structure to collect the backscattered light

coming from the particle and, with the collaboration of the Center for Biomedical Engineering Research (C-BER) at INESC TEC, devised a method to differentiate and identify trapped particles [7, 8], which may represent a great advantage in new methods for disease diagnosis.

As the joint CAP/C-BER research kept moving forward we came across a challenge: the need to trap and acquire the backscattered signal from exosomes. Exosomes are extracellular vesicles of nanometer dimensions, that have a huge potential as translational biomarkers for diagnosis [9]. Their diameter ranges from 30 to 300 nm. These vesicles have gained bigger importance over the past few years, since evidence appeared that the cells of a specific kind of tumour release specific exosomes [10–12]. This way if a non-invasive technique exists that can analyse and distinguish these exosomes, it can greatly contribute to early cancer detection, benefiting the patient's treatment. However, the fact that their size falls into the nanometer scale makes it impossible to optically trap, at least using the techniques we had at our disposal at the time. This is the case because optical tweezers using a polymeric structure at the top of the fibre is a diffraction-limited technique, which in practice means that the resolution is limited to about the dimension of the wavelength. We use a wavelength of 980 nm throughout our experiments, and so it was verified that once we reach a 1 μm scale, i. e. a particle with 1 μm of diameter, it is no longer possible to trap it this way.

Objectives

Like every other adversity we came across, we tried to find a solution for it, and so the idea of this thesis came to life. We needed to study and develop non-diffraction-limited techniques that would allow the trap of nanometer-sized particles. If we could achieve this result we would be able to perform a much better study of the exosomes, and of every other particle, we may need to analyse.

Although optical trapping at a nanometer scale is a field where there are already some fairly well-developed techniques, no one at the group had any experience with it. So a wide study of the field was demanded, to help us understand what techniques we could use and adapt to our needs, in order to achieve our goals.

1.1 The principles of optical trapping

When a dielectric particle is exposed to a radiation source, such as a laser beam, it will experience an optical force acting on it. This force is present due to the momentum transfer that occurs between the scattered and incident photons and can always be decomposed in two components - the scattering force and the gradient force.

The scattering force is proportional to the beam intensity and has the same direction as that of propagation. It is quite intuitive to understand why that happens. If we consider a laser beam being incident on the particle from one direction, we know that the radiation, if not absorbed, will be scattered in several directions, resulting in the momentum transfer between particle and photons, that originates the forces. Now, if the particle is isotropic, these forces will cancel each other out in all directions but one, the propagation direction [13]. As for the gradient force, as the name suggests, it is proportional to the intensity gradient and has the same direction as the gradient field - opposite to the propagation direction. A balance between these two components must happen, for stable trapping to occur.

The description of these optical forces will ultimately depend on the ratio between the particle diameter and the wavelength of the beam. As such, different trapping regimes can be distinguished. When the particle to be trapped has a much larger radius than the wavelength of the laser ($a \gg \lambda$) it is in the Mie scattering regime. Here, a description based on ray optics can be provided, and the interaction between particle and laser beam can be seen in terms of pairs of rays, that limit the converging beam [14]. The refraction of these rays corresponds to the momentum change in light, which, by Newton's 3rd law, results in an equal and opposite momentum change in the particle.

In figure 1.1 a geometrical representation of such rays can be seen. The vector sum of the F_a and F_b forces represents the resulting restoring force acting on the particle. This force points in the direction of the focus, leading the particle to a stable trapping position. As it is noticeable from the figure, we can also speak of gradient and scattering forces in this regime. For that, we denote the component of the force that points in the direction of light propagation as the scattering force component, F_s, and the component of the force pointing in the gradient direction as the gradient force component, F_g. The directions of these forces depend on the position of the particle relative to the focus.

Once the particle's dimensions decrease to a point where the radius is much smaller than the wavelength ($a \ll \lambda$) we enter a new regime - the Rayleigh scattering regime. In

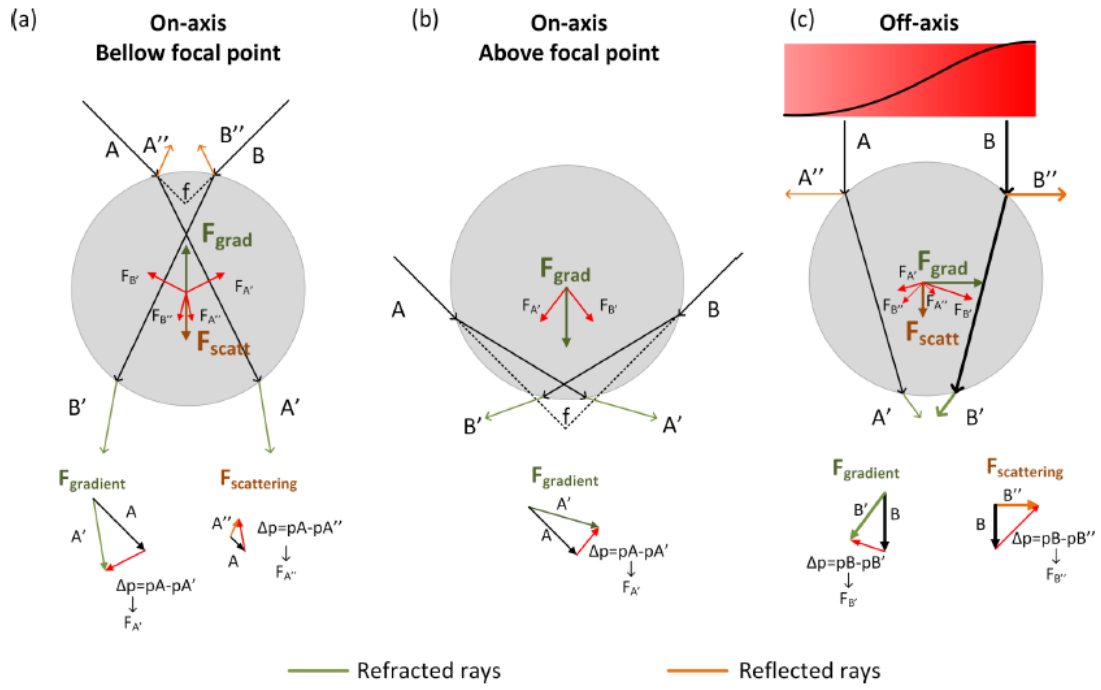


FIGURE 1.1: Geometrical representation of optical trapping forces obtained from reference [15]. Forces acting on a particle located (a) bellow the focal point, (b) above the focal point, and (c) laterally deslocated relative to the focal point.

this case, ray optics no longer suffices, and the particle is treated as a point dipole and both force components can be mathematically defined. The scattering force results from the absorption and redirection of light by the dipole. Given by

$$F_{scatt} = \frac{I_0 \sigma n_m}{c}, \tag{1.1}$$

it is proportional to the radiation intensity (I_0) and it depends on the medium's refractive index (n_m) and the scattering cross-section of the particle

$$\sigma = \frac{128\pi^5 a^6}{3\lambda^4}\left(\frac{m^2-1}{m^2+2}\right)^2, \tag{1.2}$$

where m is the ratio between the refractive indexes of the particle and the medium ($\frac{n_p}{n_m}$).

As for the gradient component of the force, it rises from the interaction between the dipole and the inhomogeneous field and can be written as

$$F_{grad} = \frac{2\pi\alpha}{cn_m^2}\nabla I_0, \tag{1.3}$$

where α is the polarizability of the particle

$$\alpha = n_m^2 a^3 \left(\frac{m^2 - 1}{m^2 + 2} \right). \tag{1.4}$$

1.1.1 Force calibration - stiffness determination

The best way to characterize a certain optical trapping configuration, whether it is a bulk setup or optical fibre-based one, is through force calculation. Determining the order of the forces acting on the particle is essential to understand the power of the tool at our disposal. Let us consider a commonly used tweezer setup commercialized by Thorlabs, where a laser beam is focused to a diffraction-limited spot using a high numerical aperture objective lens - see figure 1.2.

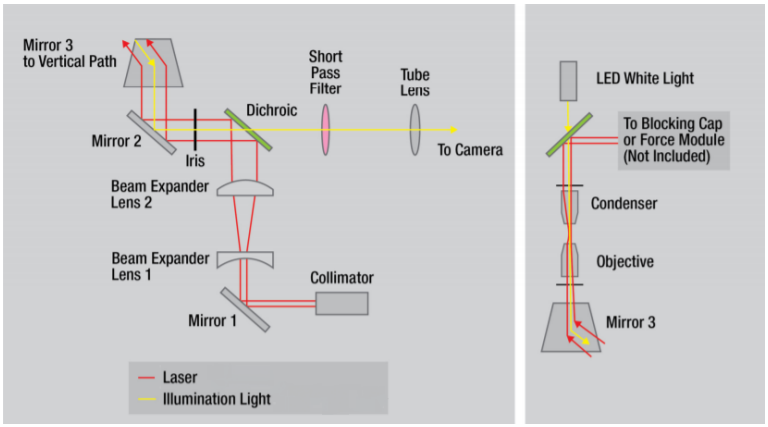


FIGURE 1.2: Schematics of a bulk optical tweezers setup, commercialized by Thorlabs [16].

In these setups, forces are usually not measured directly but determined through the stiffness of the trap. Stiffness calibration methods may be categorized in 3 different types, active, passive and direct [17].

In active methods, the trap stiffness is determined through calibration of the optical force exerted by the laser during a movement initiated by an external force. An example of such a method is the drag force, where the displacement of a trapped particle from its equilibrium position due to an applied force is measured [18]. When taking this approach, the inertial contribution of the force is considered negligible, and only the drag force is considered.

Determination of stiffness through passive methods is based on the study of the thermal fluctuations of the trapped particle. In the case of the power spectrum method, stiffness for a particle of known radius in a trap is determined by fitting its power spectrum to a Lorentzian curve [19].

As for the direct stiffness calibration methods, they rely on the measurement of the changes in momentum of the scattered trapping light. This is not frequently used, as it usually requires a dual-beam trap and the collection of the totality of the scattered light.

For now we have only briefly mentioned the set of available stiffness determination methods, and latter on the ones used in the context of this thesis will be discussed in detail.

1.2 Optical forces at a nanoscale

So far a general view of optical trapping has been given, so the reader could understand the different regimes in which it may occur. For the purposes of this section, however, I would like to focus the attention on the dipole forces - Rayleigh regime. Following Maxwell's stress-tensor formalism, presented in chapter 14 of reference [20], the conservation law of linear momentum in an optical field is used to derive an expression for the optical force acting on a particle.

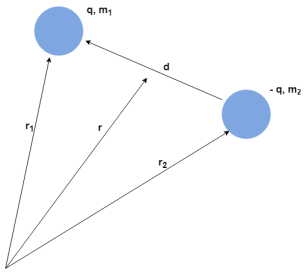


FIGURE 1.3: Scheme of the dipole by which the particle is approximated.

In the Rayleigh regime, a particle can be described by a dipole, like the one in figure 1.3, formed by two opposite charged particles, (q, -q), separated by a distance d. Considering a dipole illuminated by an arbitrary electromagnetic field, the motion equations that describe each of the particles can be written as:

$$m_i \ddot{r}_i = q\Big[E(r_i,t) + \dot{r}_i \times B(r_i,t)\Big] - \nabla U(r_i,t) \qquad i = 1,2 \qquad (1.5)$$

where U represents the binding energy between both particles.

By defining a center of mass coordinate, $r = \frac{m_1}{m_1+m_2} r_1 + \frac{m_2}{m_1+m_2} r_2$, the electric field at each particle's position can be described by a Taylor expansion:

$$E(r_i) = \sum_{n=0}^{\infty} \frac{1}{n!}\Big[(r_1 - r)\cdot\nabla\Big]^n E(r) = E(r) + \Big[(r_1 - r)\cdot\nabla\Big]E(r) + ... \qquad i = 1,2 \qquad (1.6)$$

that can be truncated after the second term when the distance d is much smaller than the wavelength of the incident radiation. This is called the dipole approximation.

Thus being, considering the definition of dipole moment, $p = qd$, the total force acting on the system, $F = (m_1 + m_2)\ddot{r}$, is given by:

$$F = (p \cdot \nabla)E + \dot{p} \times B + \dot{r} \times (p \cdot \nabla)B \tag{1.7}$$

where the first term on the right side originates from the inhomogeneous electric field, the second one from the Lorentz force and the last one from the movement in the inhomogeneous magnetic field. This last term can be ignored, as we are not working at relativistic speeds.

Considering the case of an electrostatic problem and a monochromatic field irradiating the particle, we arrive at the expression:

$$\langle F \rangle = \frac{1}{2} Re\Big\{ (p^* \cdot \nabla)E - i\omega(p^* \times B) \Big\} \tag{1.8}$$

that yields the same result as the one shown in chapter 3 - equation 3.3. By defining the induced dipolar moment by $p = \alpha(\omega)E(r_0)$, where $\alpha = \alpha^{'} + i\alpha^{''}$ is the particle's polarizability, expression 1.8 can be rewritten in the form:

$$\langle F \rangle = \frac{\alpha^{'}}{2} \sum_i Re\Big\{ E_i^* \nabla E_i \Big\} + \frac{\alpha^{''}}{2} \sum_i Im\Big\{ E_i^* \nabla E_i \Big\} \tag{1.9}$$

where the first term represents the gradient force $F_{grad} = \frac{\alpha^{'}}{4} \nabla (E^* \cdot E)$ and the second represents the scattering force, proportional to the dissipative part of the complex polarizability. If we represent the electric field in terms of real amplitude, E_0, and phase, ϕ, we reach the form of the expressions 1.1 and 1.3.

These results do not consider the case where the external electric field is affected by the presence of the particle, which may, in fact, happen when the particle is near a cavity or a material boundary. This phenomena, named self-induced back-action (SIBA), can be accounted by introducing a perturbation correction in the electric field expression - see reference [20] for more details.

1.3 Nano optical trapping

From theory to experiment, nano-optical trapping has become a reality that finds applications in the most variate fields. Beginning in physics and material science, nano trapping techniques have been applied in the trapping and manipulation of a very diverse range of objects, such as metallic [21, 22] and plasmonic [23, 24] nanoparticles, quantum dots [25] and even carbon nanotubes [26]. Nonetheless, one of the main areas of application of optical manipulation is the biomedical field. Using nano trapping methods allows the manipulation of single structures, but most importantly, it provides a way to study dynamic processes in a simpler way. Proteins have been trapped and measured [27, 28] and their interaction with DNA [29] and with other proteins [30] was studied.

Many techniques exist that make nano-optical trapping possible [31]. Throughout this section an overview of such techniques will be presented, the main focus laying on plasmonic nanohole techniques.

1.3.1 The first echos

In order to get dipolar forces strong enough to trap a nanoparticle, a strongly enhanced field is of the essence. Such a field is usually obtained near material edges, corners, apertures and metallic tips as Kawata and Sugiura showed in their pioneering work [32]. There they use evanescent fields produced in the near field of a surface of a sapphire prism to trap microparticles (sizes ranged from 1 to 27μm), it was the beginning of near field trapping (NFT).

The first works regarding the trapping of particles with nanometer dimensions began to appear by the end of the 1990's decade. Mainly they were theoretical and based on computer simulations, but they showed that it was indeed possible to trap such small specimens and proposed methods to do so. In a paper from 1997, Novotny *et al.* proposed a trapping scheme based on a metallic tapared shape tip that was externally illuminated, in order to produce a strong field enhancement [33]. Through their simulations, they demonstrated that the field near these metallic tips is composed of evanescent waves, that decay exponentially with the distance from the tip, which in practice results in a large field gradient, that increases the trapping force. They also verified the existence of a strong dependence of field distribution on the polarization of the incident light. For light polarized along the tip's axial direction, the enhancement was much larger.

Two years later, Okamoto and Kawata conducted a study of the optical forces exerted on a particle near a nano-aperture [34]. By simulating a glass substrate coated with a metallic thin-film layer ($\lambda/5$) where a subwavelength aperture ($\lambda/4$) was made, they also observed the existence of a polarization-dependent light field distribution - see figure 1.4 (A). They took yet one step forward and studied the force distribution outside such aperture, for a particle with a diameter of $\lambda/2$. These results are presented here in figure 1.4 (B) and as a consequence of the light distribution, the force distribution will also present dependence on the polarization. Regardless of that dependence, their results clearly showed that this type of configuration is able to produce strong enough forces to trap a nanoparticle.

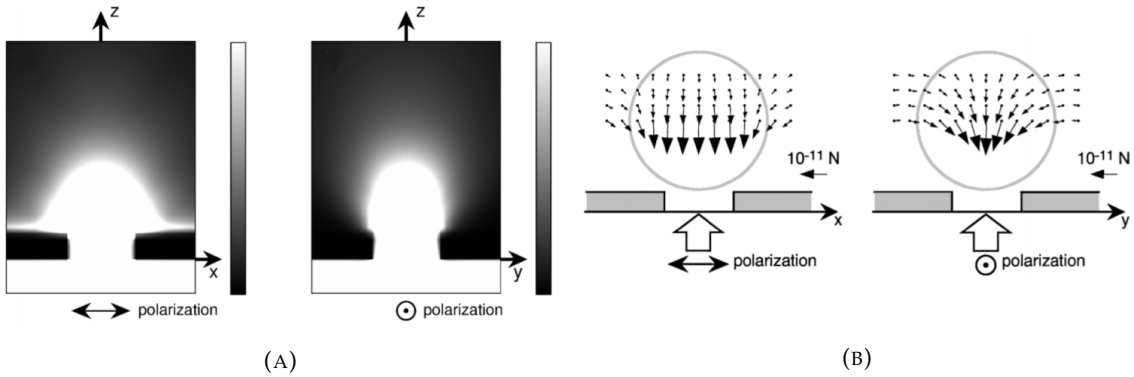


FIGURE 1.4: (A) Spatial distribution of light intensity near an aperture with a diameter of a quarter of the wavelength, for different observation planes relative to te light polarization. (B) Spatial distribution of the force exerted on a particle (represented by the grey circle) near the aperture. Figures adapted from reference [34].

1.3.2 Plasmonic nano optical tweezers

Good alternatives to conventional tweezers are those based on plasmonic techniques. By nanostructuring a given substrate it is possible to confine the incident laser beam beyond the diffraction limit and significantly enhance the local field thanks to the existence of a surface plasmon resonance (SPR).

As we have seen previously, in the 1990s some groups suggested that it was possible to take advantage of this resonance to perform nano trapping. In the years that follow, this was experimentally demonstrated. At the beginning of the 2000s, a work by Volpe *et al.* demonstrated that a surface plasmon polariton (SPP) at a glass/Au/water interface produced a 40 times increase in the optical forces exerted on a dielectric microparticle

[35]. However, given that it was a flat film interface, the generated potential was homogeneous, not allowing trapping to occur but guiding the particle along the surface instead. As Quidant *et al.* show in their work [36], trapping a particle at an interface requires additional confinement of the field in that region. To obtain such potential, Quidant and his team used gold nanostructures assembled in a glass prism. The prism was then illuminated under total internal reflection with a p-polarized plane wave which leads to the formation of a periodic optical potential pattern for Rayleigh dielectric particles. In figure 1.5 a reproduction of the results they found for the force distribution is presented. Potential wells, to where the particles will be attracted to, can be observed between the gold structures.

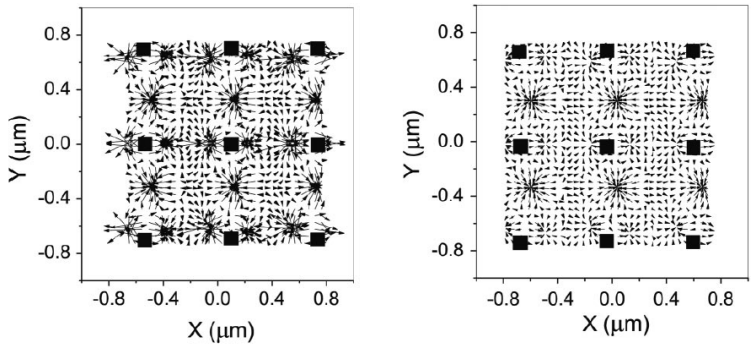


FIGURE 1.5: Force distribution for a 50 nm dielectric particle calculated at a distance z=100 nm of the surface. Image adapted from reference [36].

From here on, a large number of groups reported the fabrication of nanostructures in glass substrates to obtain the necessary potential wells for trapping [37–41].

A very common configuration relies on the use of nanorings. Such nanostructures can either be fabricated by electron-beam lithography [37], or by focused ion beam (FIB) milling [40], as can be seen in figures 1.7 (A) and (B), respectively. In both cases, when illuminated with p-polarized light these structures will work as a nano lens, concentrating light beyond the diffraction limit in the space between the rings [42]. This is most frequently done through the Kretschmann configuration, where light is incident in a prism under the total internal reflection condition so that the evanescent fields generated can penetrate the surrounding medium. To ensure index matching between prism and glass substrate an index matching liquid is used, as shown in figure 1.6 (A). This way, when a solution of nanoparticles, such as polystyrene beads [37], is placed on top of the nanostructures and the laser beam is incident at an angle close to the critical one the beads are

trapped by the arrays. It is worth noticing that the use of such configurations does not require the development of new trapping setups, but can indeed be incorporated in already existing commercial trapping arrangements as was done in reference [40].

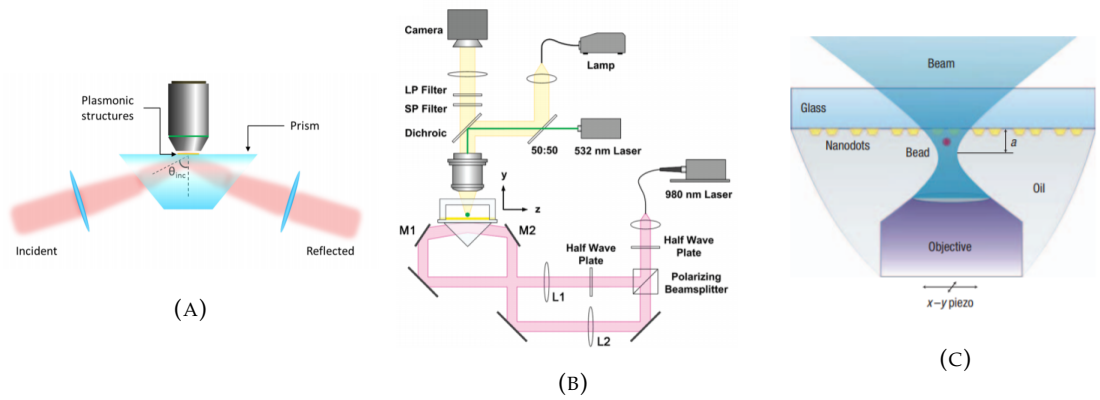
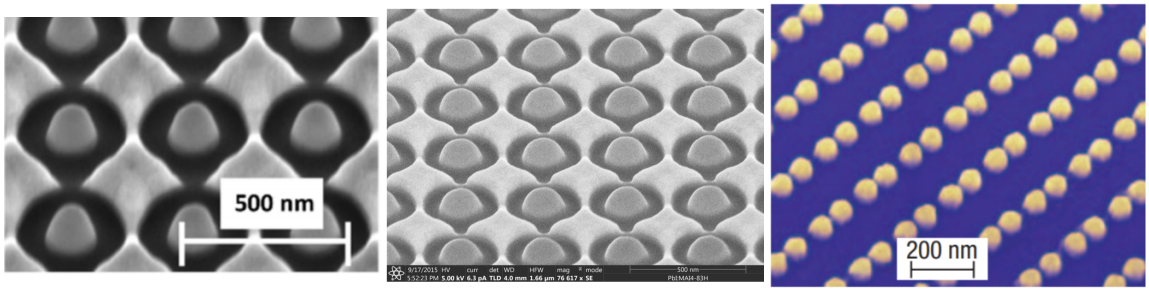


FIGURE 1.6: (A) Kretschmann configuration scheme used in reference [37]. (B) Bulk setup configuration used to excite counterpropagating SPPs through Kretschmann configuration in reference [41]. (C) Schematics of the nano tweezers used in reference [39].

Other illumination configurations and different nanostructures may also be considered. Wang *et al.* have used a gold stripe fabricated through e-beam lithography on a glass substrate to excite evanescent waves capable of trapping nanoparticles [41]. By reducing the amount of metal in use they aimed to reduce the heat effects. Although they also use the Kretschmann configuration to illuminate the substrate, the idea is a bit different. They wanted to use counterpropagating surface plasmon polaritons (SPP) on the gold stripe, so two beams with the same polarization are simultaneously incident at the prism - see figure 1.6 (B). A particle would then be trapped at the equilibrium position, which could be adjusted by changing the power of the incident beams to introduce a displacement.

In 2008, Grigorenko *et al.* reported for the first time trapping results with 3D nanometric optical tweezers based on plasmonics [39]. Also using high-resolution electron beam lithography, they fabricated coupled pairs of gold nanodots on a glass substrate that worked as a nanoantenna - see figure 1.7 (B). These types of structures will support localized surface plasmons (LSP) when illuminated with linearly polarized light along the vector that connects the nanodots. In the case of this particular work, the laser beam was focused by an objective and an immersion oil of refractive index of 1.5 was used between the lens and the substrate to ensure index matching - see figure 1.6 (C). Through this technique, they were able to trap polystyrene beads with dimensions varying from $6\mu m$ to $200nm$ and verified that when the incident beam spot was dislocated along the lattice the

trapping position also varied periodically. This work laid the foundation for all those that followed based on nano trapping with optical antennas [43, 44].



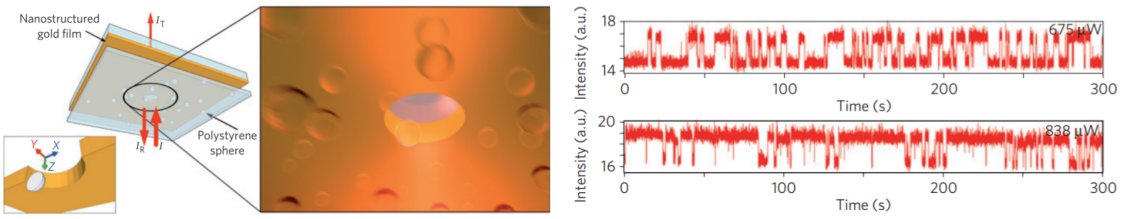
(A) (B) (C)

FIGURE 1.7: (A) Nanostructured substrate with arrays of nanorings fabricated by e-beam lithography, used in reference [37]. (B) Nanostructured substrate with arrays of nanorings fabricated by focused ion-beam milling, used in reference [40]. (C) Nanostructured substrate with pairs of gold nanodots fabricated by e-beam lithography, used in reference [39].

1.3.2.1 The self-induced back-action mechanism

By the end of the 2000s, the possibility to explore the interaction between the particle to trap and the trap itself, to obtain stable trapping, was discovered. The use of a dynamic approach, where the particle has a strong influence on the local electric field, makes it possible to overcome the scaling of optical forces and the increase of Brownian motion, enabling the reduction of the local intensity in the trap.

The concept of self-induced back-action (SIBA), summarily described in the last paragraph, was coined by Juan *et al.* in their 2009 work [45]. Using a 310nm diameter aperture, fabricated with FIB milling in a 100nm gold film on a glass substrate, they were able to trap polystyrene particles with diameters of 50nm and 100nm - see figure 1.8 (A). The sample was mounted upside-down, so gravity would not interfere with the trapping results, and illuminated by a 1064 nm Nd:YAG laser polarized along the x-direction. This choice of aperture dimensions and wavelength in use was not arbitrary, as this relation plays an important role in the SIBA mechanism. The aperture will have a transmission resonance wavelength that will depend on its dimensions, that is, for a given illumination wavelength the aperture's transmission will be maximum. Above that wavelength, the optical transmission of the aperture becomes especially sensitive to changes in the refractive index of the surrounding medium, which will be altered by the presence of a particle. Hence, given that the resonance wavelength for a 310nm aperture was 990nm, they used a laser of 1064nm.



(A) (B)

FIGURE 1.8: (A) Schematics of the aperture experimental configuration and (B) evolution of transmitted intensity through the same aperture for two different laser powers. Images reproduced from reference [45].

Since the particle has a larger refractive index than that of water, its presence will increase the aperture's transmission, functioning as a detection mechanism. Besides, this also allows the existence of a feedback mechanism that, in addition to the gradient force, helps to sustain the trap. When the particle moves away from the aperture, wether by Brownian motion or mechanical drag, the transmission will drop as a result of refractive index variation. This will cause a decrease in the rate of photon momentum that crosses the aperture, which by Newton's 3rd law will give rise to a force acting on the particle in the opposite direction. The same reasoning is valid for the opposing situation where the particle approaches the aperture. In this case transmission increases and the resulting force pushes the particle out. This balancing force will then be responsible for keeping the particle in its stable trapping position.

The trapping was studied by measuring the intensity transmitted by the aperture during a certain amount of time - the results they obtained can be seen in figure 1.8 (B). The higher intensity level corresponds to moments when there is a particle trapped at the aperture and the lower indicates that no particle is present. With higher laser powers a longer trapping time was verified. One of the main advantages of this SIBA mechanism is that it allows optical trapping to occur at very low laser powers, under $1\mu W$, which in practice can reduce the risks of damaging the particle.

1.3.2.2 Optical trapping with nanoholes

From all the types of nanostructures seen so far, nanoholes can perhaps be the most simple and interesting ones [46]. Besides being able to implement the SIBA mechanism, allowing for a better trapping stiffness and performance, different types of apertures can be manufactured allowing for their combination with antenna's properties - bowtie and double nanohole apertures [27, 44, 47, 48]. For now, only planar configurations will be

considered and the work involving optical fibres are left for discussion at the end of the chapter.

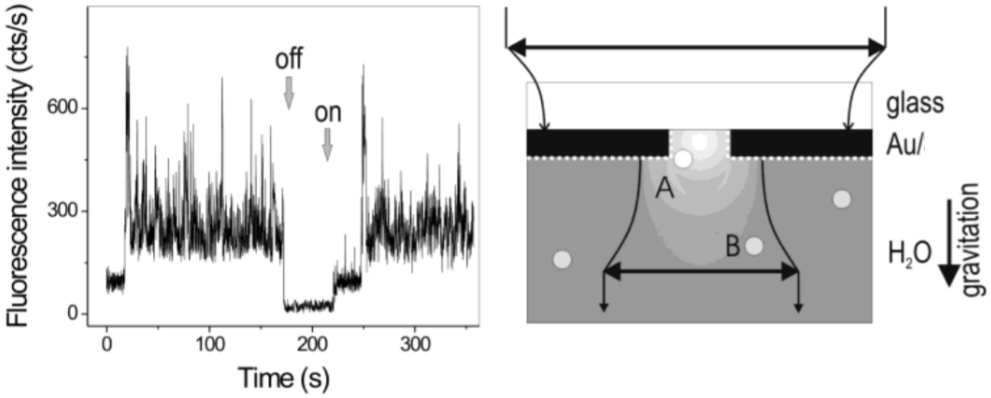


FIGURE 1.9: Fluorescence emission from one single nano aperture of 500 nm diameter (left) and schematical representation of the fluidic chamber (right). Image is from reference [49].

By depositing a gold layer in a glass substrate through either e-beam or thermal evaporation and then using FIB milling to open an aperture in that layer, a configuration such as the one presented in figure 1.8 (A) can be achieved. Even before SIBA was discovered, this was already a common procedure. Lets consider what Kwak *et al.* did to trap 200 nm latex beads in an aqueous solution [49]. As a proof-of-principle experiment, they used fluorescent beads to facilitate the detection, instead of measuring the transmitted signal. An array of nanoholes was fabricated into the gold film with enough separation between each hole so that no electromagnetic coupling would occur. The sample was then placed on an inverted microscope with a fluidic chamber mounted in it, much like that of the right side of figure 1.9, and the detection of the fluorescent signal for each nanohole was measured through an avalanche photodiode. The collected signal for one single nano aperture can be seen in the left side of figure 1.9, where an increase in the fluorescence intensity is verified after the laser is on for a while, indicating the presence and trapping of a latex bead.

Once this proof-of-principle was achieved the following step was to try to record the transmission signal through the aperture instead of using fluorescent particles, much like Juan *et al.* did when demonstrating SIBA. Nonetheless, that was not the only innovation that came along, groups began to try different aperture shapes.

Pang and Gordon performed two works in the years of 2011 and 2012 with double nanohole apertures. In the first one, they trap 12 nm dielectric spheres [50] and in the

later a single protein is the trapped specimen [27]. For both cases the aperture fabrication process was in everything similar to what was previously described, differing only on the type of shape designed by FIB milling. The result can be seen in figure 1.10, the two holes have a diameter of 110 nm and are connected by a channel with 30 nm width. To proceed with optical trapping tests the sample was sealed with a PDMS layer, as to create a microfluidic chamber containing the solution of particles to trap. Such chamber can be seen in the schematics of figure 1.11 (B), where it is also worth noticing that the solution stays below the aperture as to prevent gravity forces from having any influence on the experiment. The sample was then mounted between two objectives - an immersion one having a large numerical aperture, from where the linearly polarized radiation, along the channel direction, will be incident and a condenser one that will collect the radiation and direct it towards the avalanche photodiode detector - see figure 1.11 (A). This is basically an adaptation from the Thorlabs setup presented in figure 1.2.

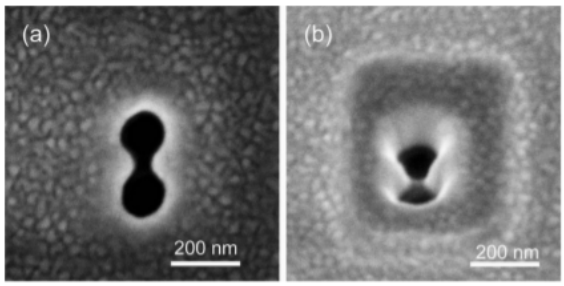
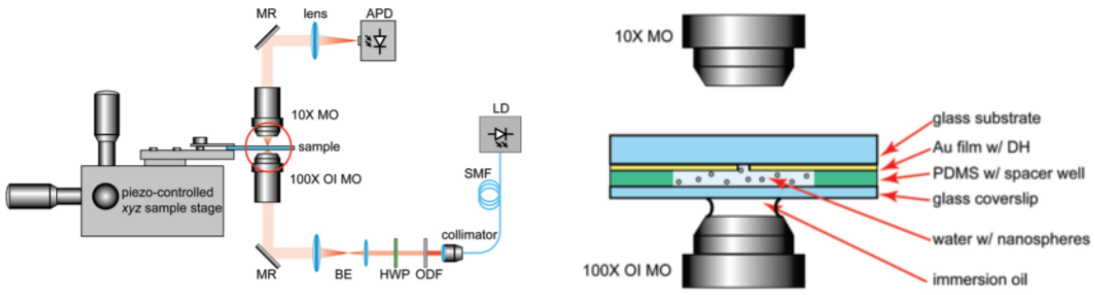


FIGURE 1.10: SEM images of the double-nanohole studied in reference [50]: (a) top view and (b) 45° inclination.



(A) (B)

FIGURE 1.11: (A) Optical trapping setup and (B) fluidic chamber assembled to test trapping. Images are both from reference [50].

They did not limit themselves to the test of the double nanohole, but instead did a comparison study between it and a single circular hole. Bearing in mind that the double nanohole trap has the same working principles described by SIBA, they found rather

interesting results. Looking at figure 1.12 we can see that both types of apertures were successful in trapping 100 nm polystyrene particles, although with some stability differences, with the circular aperture presenting a longer trapping time. As for the 20 nm particles, the results are very different. The circular one is not able to trap such a small particle, while the double nanohole presents very stable trapping. They had just demonstrated that double nanoholes are better at trapping very small particles than relatively bigger ones.

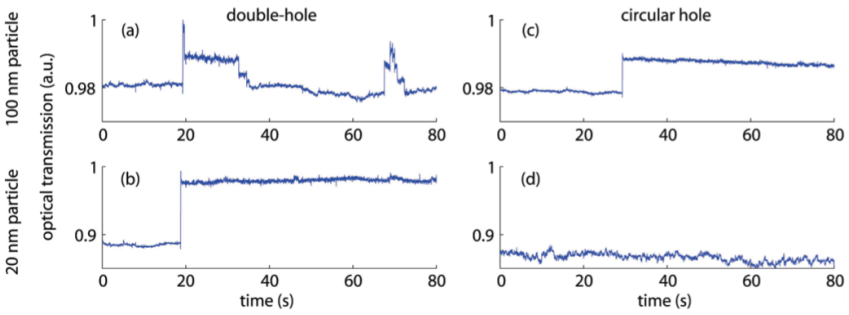


FIGURE 1.12: Optical transmission measurements through a double nanohole (a, b) and a single circular hole (c, d) during the trapping of 100 nm (a, c) and 20 nm (b, d) polystyrene particles. These results are from reference [50].

This difference in performance for the two types of apertures happens because the optical transmission in the small area between the two circles is extremely sensitive to changes in the refractive index. Since only particles with smaller diameters than the channel separation can fit in it, only those will be able to induce a strong trapping force due to transmission changes - SIBA mechanism. The larger particles will be kept out, inducing a much weaker force, hence the unstable trapping for 100 nm particles with the double nanohole. As for the circular aperture, being isotropic, the local field enhancement is not so strong and only relatively large particles will be able to induce a change in the transmitted radiation, inducing the trapping force.

It has become clear that each type of aperture presents advantages for different types of particles, depending on what we wish to trap. Double nanoholes have already proven very effective, showing good trapping stiffness, that increases with laser power [47]. It has been used in the trapping of single proteins [27] with a hydrodynamic radius of 3.4 nm, having allowed for the identification of the unfolded state of the protein - see figure 1.13. More so, analysis of egg protein composition has been successfully conducted [51], proving to be a very effective technique in the analysis of proteins in heterogeneous solutions without the need of denaturation, labelling or tethering.

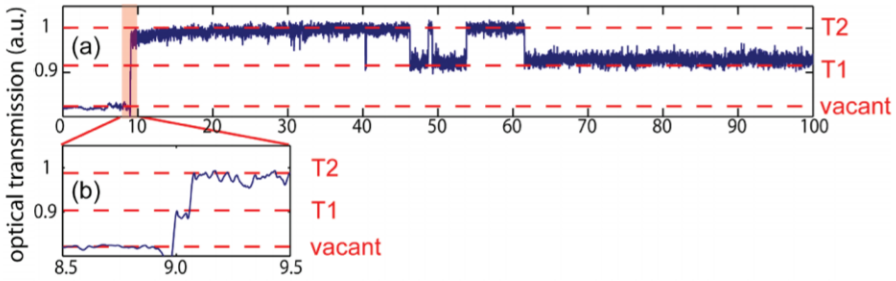


FIGURE 1.13: Optical power transmitted through a double nanoaperture during the trapping of a single protein. Three different states were identified: a vacant one, a second one corresponding to the trapping of the protein (T1) and a third one that indicated that the protein unfolded (T2). These results are from reference [27] and were acquired using a laser power of 13.4 mW.

1.3.2.3 Thermal considerations

Whenever dealing with plasmonic structures one must face the problem of heating due to Ohmic loss. Besides imposing a limit to the optical power in use, as too much power causes more heat that may damage the particle, it also leads to the occurrence of thermophoresis [52]. Thermophoresis is a phenomenon of nanoparticle drifting, in addition to the Brownian motion, in the presence of a thermal gradient. Depending on the particle's properties they can either present positive thermophoresis, moving from hot to cold regions, or negative thermophoresis, moving in the opposite direction. Whichever is the case, one thing is for sure, if the phenomenon occurs during an optical trapping experiment it will affect the results.

The net force acting on a particle present in a temperature gradient can be described by [53]:

$$f = -\frac{S_T}{\beta}\nabla T \tag{1.10}$$

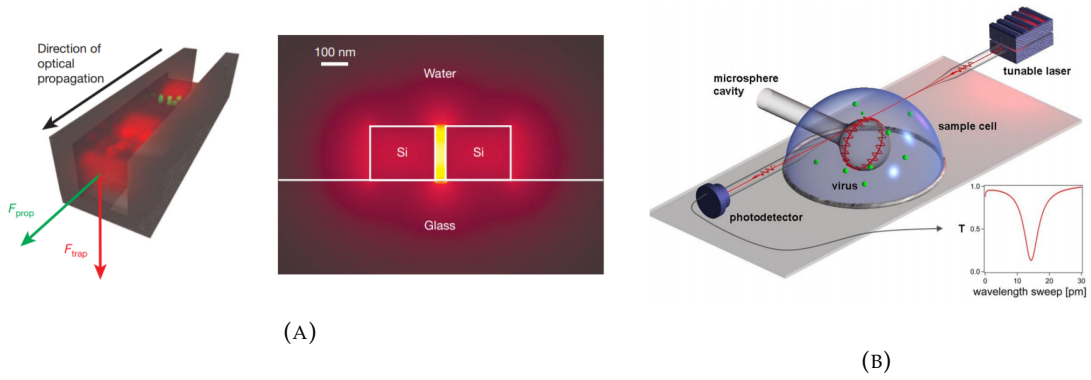
where $S_T = \frac{D_T}{D}$ is the Soret coefficient, with D_T being the thermodiffusion coefficient and D the diffusion coefficient, and $\beta = \frac{1}{k_B T}$. To fully grasp the extents of the problem lets consider that the plasmon resonance induces a temperature increase of 3K. It does not seem much. However, we must be aware that this increase happens in lengths lower than $1\mu m$, so in fact, there will be a large temperature gradient present that will affect the particle's motion.

When confronted by these issues some groups developed solutions that allow the minimization of the problem. The most known approach is the implementation of a heat sink

within the trapping structure. By introducing materials with a higher thermal conductivity than water and glass ($\kappa_{glass} = 1W/Km$) bellow the plasmonic metal, the heat generated during excitation will be conducted in their direction, instead of dissipating into water. Wang *et al.* [54] constructed a gold nanopillar on top of a copper film deposited on a silicon substrate, since both have very large thermal conductivities ($\kappa_{Cu} = 401W/Km$ and $\kappa_{Si} = 148W/Km$), they were able to reduce the thermal problem.

1.3.3 Other techniques

Other techniques exist that allow the trapping of nanoparticles, and although they will not be under the spotlight throughout this work I believe they are worth mentioning, for the more curious reader, at least.



(A) (B)

FIGURE 1.14: (A) Slot waveguides [55] and (B) microsphere used to excite a whispering-gallery mode [56] used to trap nanoparticles.

Not all nano trapping techniques involve a plasmonic excitation, there are other ways to harvest the near-field forces fundamental to the process, like slot waveguides [55] and whispering-gallery modes [56–58]. Slot waveguides are waveguides with sub-wavelength cores that guide strongly confined light. By making use of the near field forces it is capable of confining the particle in the core and thanks to the scattering force the particle can be transferred along the longitudinal direction of the core - figure 1.14 (A). As for whispering-gallery modes, as the name indicates they are optical modes created inside a resonator, usually spherical. The modes of the resonator give rise to a scattering force that will push the particles around. By balancing different and counterpropagating modes the particle can be lead to a stable trapping position.

Every technique presents its advantages and disadvantages depending on the specific application we wish to use it for, but most generally, the best way to evaluate a given

Structure	Method	Stiffness ($fN\ nm^{-1}\ mW^{-1}$)
nanopillar [39]	exp	0.013
slot waveguide [55]	sim	0.2
double nanohole [47]	exp	0.1
circular aperture [45]	sim	6.6

TABLE 1.1: Trap stiffness values for different optical trapps scaled for a 10 nm dielectric sphere [47].

configuration is by its trapping stiffness. In table 1.1 a set of stiffness values found for different techniques, either through experiments or simulations, is presented.

1.3.4 Optical fibre nanotweezers

All the techniques we have seen so far, being based on a planar configuration, restrict the trapping position to a fixed point, which imposes limitations on the manipulation of the trapped specimen. Being a very desirable feature, groups searched for a way to ensure more freedom of movement to manipulate samples and ended up applying some of the latter presented techniques on the top of optical fibres.

The idea of using a scannable tip, much like a scanning near field optical microscopy (SNOM) one, was not new [33], the novelty was in the application of optical fibres for such purpose. In a computational study from 2000 [59], a trapping configuration relying on a tapered optical fibre was first proposed. Having a tip diameter smaller than the wavelength, the 3D optical field formed at the near field of the tip would enable the trapping of a particle. Although this first proposal did not mention the use of a metallic coating on top of the fibre, it will later become a common configuration - a tapered, metal-coated fibre with an aperture at its apex.

Depending on the taper's shape, the guiding properties of the probe will be different, which will influence the transmission properties, and consequently the trapping itself. The properties of light propagation in circular dielectric waveguides with finite metal claddings were studied by Novotny *et al.* in [60], and the mode structure of such waveguides was calculated. From those results, it was understood, that the gradual decrease of the core diameter across the taper length results in the reduction of the number of propagating modes. One mode after the other runs into cutoff - the wave vector becomes imaginary and the field decays exponentially - until only the fundamental cylindrical mode, the HE_{11}, still propagates. Below a given diameter, that will depend on the wavelength

in use, not even the HE_{11} can propagate, and we are left only with evanescent fields. As a consequence, the actual power that reaches the aperture will depend on the distance between the z coordinate where the cutoff diameter for HE_{11} happens and the z coordinate where the aperture is located, both marked in figure 1.15.

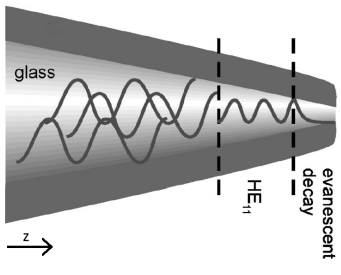
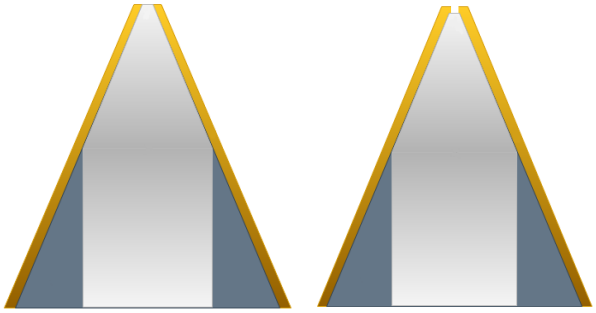


FIGURE 1.15: Mode propagation in a tapered metal-coated optical fiber for an arbitrary wavelength. The outer darker layer represents the metal coat and the dashed lines mark the places of cutoff. Image adapted from [61].

This way, in what regards the influence the shape of the taper has on the transmitted power, Novotny showed that large taper angles, between 30º to 50º, provide the best conditions for light transmission [62]. In [61], a simulation work was performed to evaluate the transmission coefficient variation with the taper angle for an aperture of 100 nm. The results showed that for an angle of about 30º we can expect a transmission between 10^{-6} and 10^{-5}, but for around 42º, it can reach values around 10^{-3}.

Regarding the aperture dimensions, according to the Bethe/Bouwkamp model [63], the transmission of a subwavelength aperture is expected to scale with $(k_0 a)^4$, where a denotes the aperture diameter and k_0 is the vacuum wave vector. A large decrease in the aperture dimensions will thus imply an even larger decrease in the transmitted signal, making it impossible to work with apertures smaller than 50 nm.

Following the theoretical considerations, the experimental approaches came along [64–67]. Tinguely *et al.* [64] presented, in 2014, a very interesting work where they try to use the fibre-based SNOM configuration to trap nanoparticles, for the first time. Even though they did not achieve trapping, they perform a very interesting comparison between two different tip geometries. They distinguished between a conventional SNOM probe, where the aperture is made by slicing the tip in a direction normal to its optical axis, and what they called a SIBA probe, where the aperture is milled using a FIB at the top of the aperture's apex - see figure 1.16.



(A) (B)

FIGURE 1.16: Schematics of the (A) SNOM and (B) SIBA probes, as described in reference [64].

Besides demonstrating the SIBA concept in a non-planar configuration they wished to make use of the extraordinary optical transmission properties (EOT) this configuration was reported to have [68–70]. The computational comparison between the forces and transmission of the two demonstrated that the SIBA probes provide indeed better transmission and better trapping performance. Also, they demonstrate that adjusting the aperture dimension in these probes so that they resemble the particle's dimensions will improve the trapping stiffness.

All the conclusions drawn from that work were latter experimentally confirmed by Berthelot *et al.* [65]. Using an aluminium coated tapered optical fibre with a bowtie nanoaperture milled at the apex, they performed the first 3D optical manipulation of 50 nm dielectric spheres with near-field fibre optic nanotweezers. Two different trapping tests were conducted, one with external illumination linearly polarized along the optical axis, and a second one where the trapping laser (1064 nm) is guided by the fibre itself. In both cases, the transmitted or reflected radiation was collected by the fibre. Also, the fluorescence of the beads was also excited using a 532 nm laser, thus guaranteeing the monitoring of the process by two independent photodetectors. Trapping confirmation was obtained, as in previous works, by signal variations.

More recently, a new trend has come, based on the use of "aperture mould" that can be re-used. The great majority of the techniques presented so far, if not all of them, rely on the use a FIB machine, which is not only a piece of very expensive equipment, it is also not available at every laboratory. Thus being, its use on every single probe may trouble the path to the final goal. But what if we only had to use a FIB machine once to get something like 50 probes?

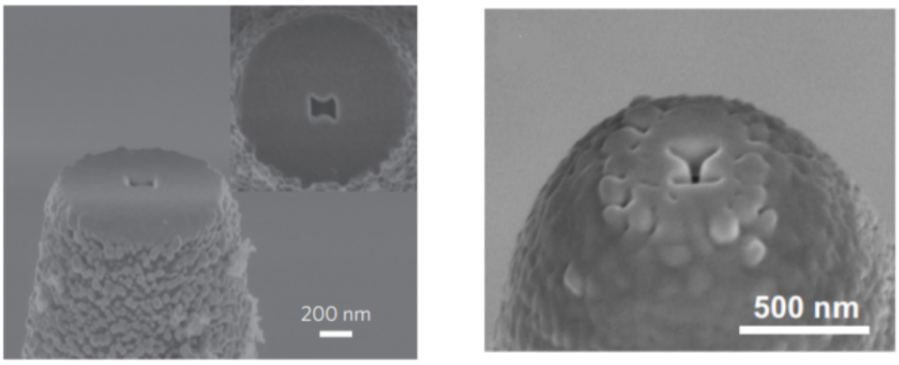


FIGURE 1.17: Bowtie nano apertures fabricated at the top of a (A) tapared optical fiber coated with aluminum and (B) a polymer tip coated with aluminum grown at the top of a cleaved optical fiber. Images adapted from references [65] and [66], respectively.

In 2018, Jamal Ehtaiba and Reuven Gordon published a paper based on this idea [71]. Using a FIB machine, they fabricated a series of rings, on a 100 nm thick gold substrate, with a diameter of 125 μm and a nanoaperture inside. The goal was for each of these rings to be transferred to an individual cleaved optical fibre by a stripping process, resulting in a fibre optical tweezer.

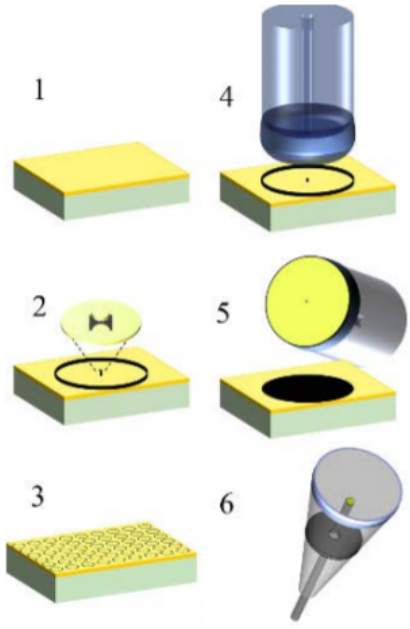


FIGURE 1.18: Schematics of the stripping process described above. Figure adapted from reference [71].

Even though this helps to reduce the need for a FIB machine, it introduces an additional step to the process, lithography. Once the fibre is perpendicular to the gold film, it is dipped in a UV curable epoxy. Then the alignment process needs to make sure that the

cleaved fibre is perfectly aligned with one of the rings in the film. Once this is guaranteed the fibre is brought into contact with it and a UV light, guided through the fibre, is turned on, exposing the epoxy for about 5 minutes. In the end, the fibre is retracted having the gold film attached to it. This entire process is schematized in figure 1.18. The trapping results presented with this configuration are in every way similar to all the ones presented so far.

1.4 Outline of this work

The reader has now been presented with the basic principles of optical trapping and the main challenges regarding the trapping of smaller specimens. A state of the art review was presented to provide a clarification of what has been done so far in the field and how we can use it to find a solution for our particular challenge.

This thesis is organized in five main chapters, the first one being already of your acquaintance. In the following chapter, the experimental methods used for the fabrication of our optical tweezers will be presented and the two that follow will focus on our results, simulation and experimental ones. In the third chapter a comprehensive study of the tweezer's geometries is presented, which allowed us to guide our probe fabrication. The trapping and light scattering results can be seen in chapter 4 and this thesis closes with a fifth chapter containing the main conclusions and our future work prospects.

Chapter 2

Experimental methods and tools

The fabrication of tapered optical fiber tweezers requires the use of some specific micro/nanofabrication techniques. As was mentioned in the previous chapter, these tweezers are based on the probes utilized in SNOM. As such, a taper has to be fabricated, coated with a metal layer and a nanometric aperture must be formed at its apex. In the context of this work the tapers were fabricated through chemical etching with HF, a gold layer was deposited through e-beam evaporation and the aperture was formed by focused ion beam milling. These tapers were latter on tested and used to optically trapp polystyrene beads of micrometre and sub-micrometre dimensions.

This chapter will thus focus on the description of the fabrication techniques, explaining their principles and showing the methodology used for each case. Furthermore we explain also how the trapping forces were experimentally measured. Here we focus only on the experimental techniques used. The simulation work developed to study and characterize the tips is presented in chapter 3.

2.1 Chemical etching with HF acid

In 1984 Turner proposed a method for the fabrication of optical fiber tapers using a chemical etching process [72]. The method is based on the utilization of an aqueous solution of hydrofluoric acid, covered with an organic solvent in which an optical fiber is dipped into to form a taper.

The process that occurs between HF and silica can be described by two reactions [73]:

$$SiO_2(s) + 6HF(l) \longrightarrow 2H_2O(l) + H_2SiF_6(aq) \tag{2.1}$$

$$SiO_2(s) + 4HF(l) \longrightarrow 2H_2O(l) + SiF_4(aq), \tag{2.2}$$

both reactions take place under the same temperature and pressure conditions. It has been demonstrated that etching is not a diffusion controlled process, and the reaction rate at which it occurs is not directly dependent on HF concentration, but on the fluoride-containing ion concentration [74]:

$$SiF_4 + 2F^- \longrightarrow SiF_6^{2-} \tag{2.3}$$

$$SiF_4 + HF_2^- \longrightarrow HSiF_6^- \tag{2.4}$$

As a consequence, the etching rate may be considered constant throughout the process [75].

In figure 2.1 we present a scheme that describes the process of taper formation through chemical etching. As can be seen, the fiber is placed vertically through the interface between the HF acid and an organic solvent, forming a meniscus onto the fiber surface. The height of the meniscus will depend on the interfacial tension and the difference in densities between the liquids, but most of all, on the fiber's diameter. As the diameter decreases so does the meniscus height [76], and the conical shape is reached through the successive decreases in fiber diameter and meniscus height [77]. Since the fiber is isotropically etched, the cylindrical shape of the fiber is conserved until the part of the fiber dipped in the acid has been completely dissolved, and the taper is formed. Once the taper is formed it will be protected by the solvent layer, that is also responsible for preventing HF toxic vapors from spreading around the environment.

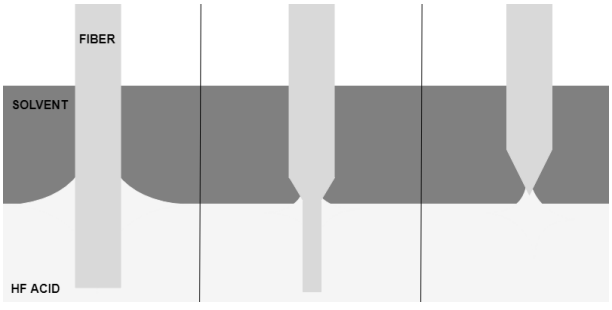


FIGURE 2.1: Scheme of optical fiber taper evolution during the etching process.

Other factors also influence the resulting geometry, namely the concentration of the HF solution used and the time the fiber stays in contact with the acid. In reference [77], Sayah *et al.* conducted a study to see how the acid concentration influenced the cone angle of the taper and its overall dimension. Their results are presented in figure 2.2, and are important to consider when determining the final parameters under which the tapers will be fabricated. As for time, what happens is that some HF vapors will diffuse into the solvent, where they will keep etching the taper's surface. This results in rough surfaces, which may be a problem when additional metal coatings are required. As a result, it is important to remove the fiber right after the taper is completely formed, to prevent unnecessary damage to the surface.

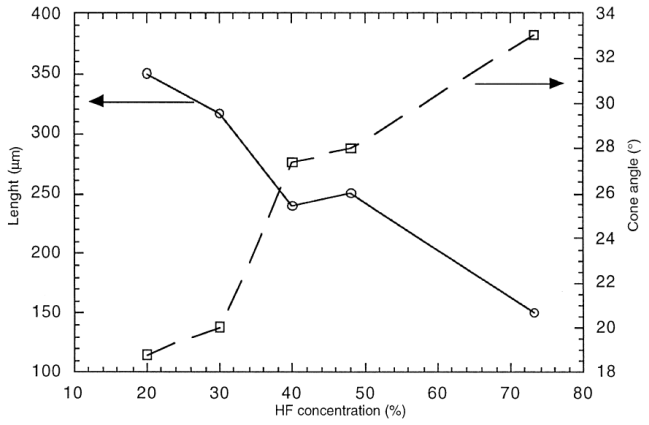


FIGURE 2.2: Cone angle and cone length as a function of HF concentration, for etching at room temperature using isooctane as a solvent. Figure adapted from reference [77]

2.1.1 Sample preparation and experimental configuration

Based on the information presented so far, a simple experimental configuration was assembled to allow the fabrication of a few tapers at a time. As HF acid etches through silica, glass containers could not be in direct contact with it. We opted for the use of rectangular plastic cuvettes placed in a glass container in a way they could not move, to prevent accidents. The configuration is depicted in figure 2.3. Previously cleaved fibers were duck-tapped to a metallic holder on top of the container, in a way that each fiber enters an individual cuvette. Each cuvette is filled with $2.5mL$ of HF acid and the solvent amount was varied from $0.3mL$ to $1mL$. The acid concentration and the solvent used were varied until we found a combination that would allow us to produce the desired taper geometry. All the details and results of this fabrication are presented in chapter 4.

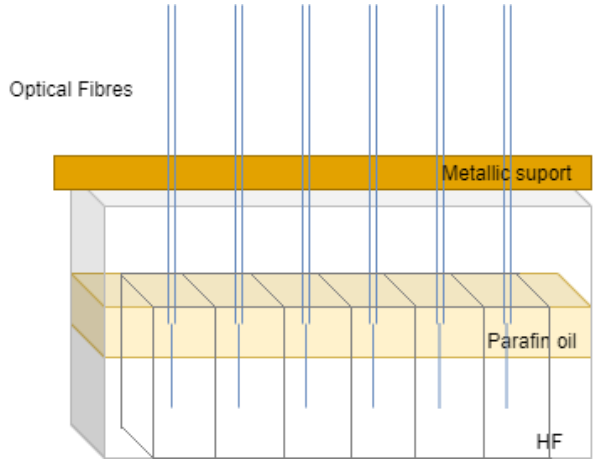


FIGURE 2.3: Experimental configuration used for etching.

2.2 E-beam evaporation

Electron beam evaporation is a physical vapor deposition technique that uses electron beams to heat up a target material, vaporizing it, so that a thin-film can be deposited onto a substrate material - see figure 2.4.

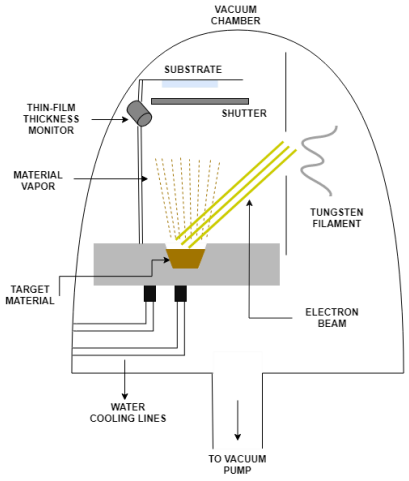


FIGURE 2.4: Schematic representation of an e-beam vacuum evaporation chamber.

To produce the beam, a current passes through a tungsten filament heating it up, which leads to a release of electrons. These electrons will be accelerated from the source (cathode) to the target material (anode), bombarding the target with high kinetic energy electrons [78]. This will heat up the material, the highest temperature being reached at the area of contact between the beam focus and the target. For this reason, it is important to water-cool the crucible that holds the material to vaporize, as it is the only way to avoid contamination [79].

For this entire process to take place, however, there needs to be vacuum in the chamber. Pressure needs to be at least $7.5 \times 10^{-}5$ Torr or lower, to allow the passage of the electrons. Consequently, an e-beam evaporation system always has to have vacuum pumps connected to it. A first one to guarantee an initial evacuation, usually a rotary vacuum pump, that will reduce the number of particles in the air to allow the safe functioning of a diffusion vacuum pump, so high vacuum can be achieved in a second step.

2.2.1 Sample preparation and assembling

The Edwards Auto 306 electron beam evaporation system available at CEMUP's clean room was used to coat the tips - see figure 2.6. For the porpuses of this work, we needed to deposit thin-films of chromium and gold in an optical taper. Being a cylindrical structure, the assembly of the samples onto the chamber is a bit more complex than simply laying a plane substrate at the top. Fortunately, the system possesses an additional rotatory structure, that can be attached at the top, where the optical fibers can be placed - see figure 2.5. The rotation guarantees a uniform deposition of the metal through the fiber's surface.

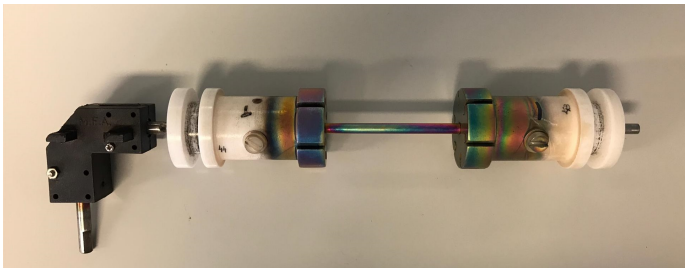


FIGURE 2.5: Rotatory sample holder.

Once the samples were mounted and ready to be placed inside the chamber, we proceeded according to the operation instructions given in the manual [80].

After the chamber is brought to atmosphere pressure, it can be open and the materials to deposit can be placed inside the crucibles. This particular system has a rotating crucible line, that allows for the deposition of more than one layer of material without the need to open the chamber more than one time. Materials must be placed in clockwise order so that when one deposition is finished, a simple turn on an external knob allows for the new material to be set in place. Afterwards, the sample holder is placed on the support at the top and the chamber can be closed, so the pump down process may begin.

The pressure must reach a value of 10^{-6} Torr before we begin to vaporize the material. After selecting the right settings for the material to deposit - see table 2.1 - and pressing the high voltage button, we can slowly start to increase the current value and elevating the crucible platform, until the metal inside starts to glow. The thin-film monitor thickness is inside the chamber so one can monitor the deposition rate at which we are working. When such rate is reached, the shutter is opened and deposition may begin.

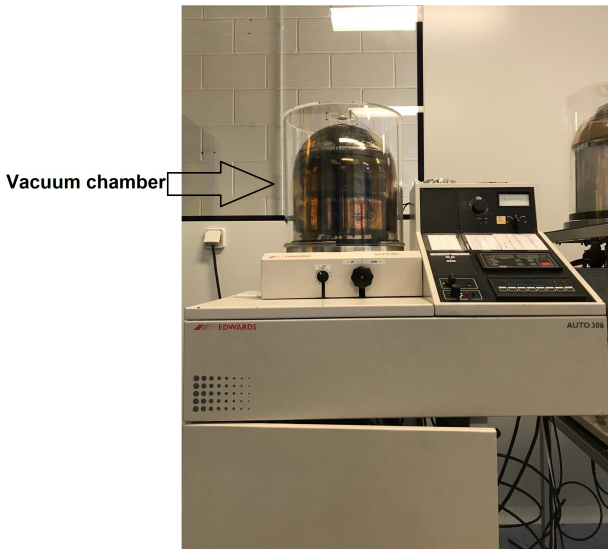


FIGURE 2.6: Edwards Auto 306 electron beam evaporation system.

Some variations of deposition rate may be verified throughout deposition time. That happens due to the evaporation of the material inside the crucible. As it evaporates, its volume decreases and the beam focus may no longer hit the material's surface. As a consequence, the deposition rate decreases. To correct this situation a balance must be found between the height of the platform and the current in use.

Material	Density (g/cm^3)	Accustic Impedance ($\times 105 g.cm^2/s$)
Chromium	7.2	28.9
Gold	19.3	23.2

TABLE 2.1: Material properties.

The shutter will close automatically once the pre-defined thickness is reached.

2.3 Focused ion-beam milling and scanning electron microscope system

The final step to achieve optical fiber nanotweezers involves a micromachining process right at the taper's apex. To do so, a dual-beam high-resolution FIB/SEM system, like the one presented in figure 2.7 was used. This Helios NanoLab 450S DualBeam system [81] belongs to the Iberian Nanotechnology Laboratory (INL), where the micromachining work was performed.

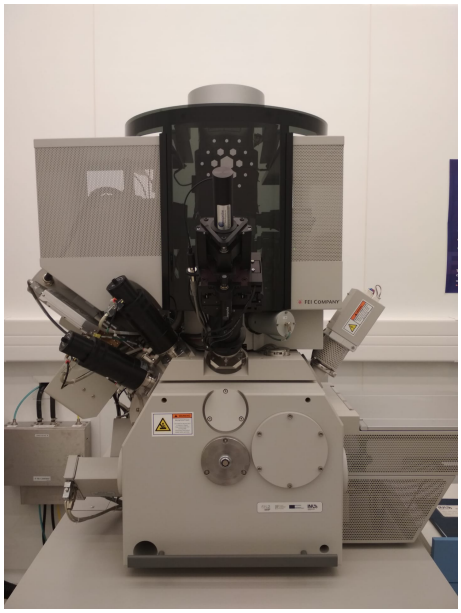


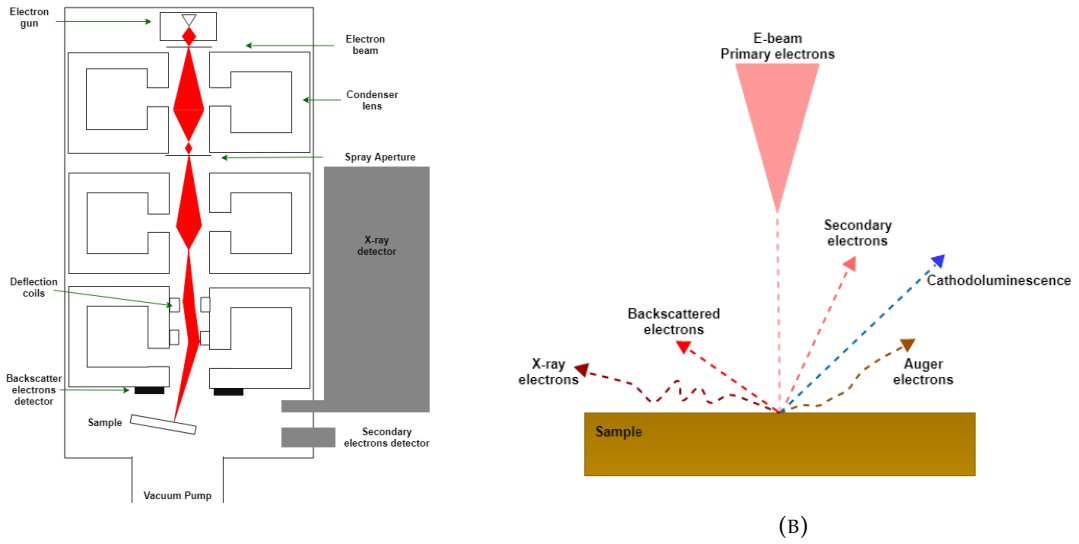
FIGURE 2.7: FIB machine Helios NanoLab 450S DualBeam, from FEI company.

Being a dual-beam system this FIB machine combines in it not only the ion beam but also an electron beam. They are inserted at a 52º angle at a coincident point in the sample surface, which allows for the collection of high-resolution SEM images of the FIB-milled surface. This way, when a sample is mounted in a planar stage with 3D translation, rotation and tilt freedom, it will have an eucentric point at the point where the two beams meet. Moving the region of interest of the sample to this point and then tilting it to obtain the desired angle of incidence leaves the sample ready for milling.

2.3.1 Scanning electron microscope

Scanning electron microscopy (SEM), as the name indicates, is a type of microscopy that makes use of an electron beam to image a sample. Unlike what happens in an optical microscope, here electrons are used. These electrons are produced at the top of a column,

in an electron gun, they are accelerated in a voltage difference, passing through a combination of lenses and apertures meant to focus it on the surface of the sample to analyse - see figure 2.8 (A). Both this column and the chamber where the sample is placed must be in a vacuum.



(A) (B)

FIGURE 2.8: (A) Scheme of a SEM column. (B) Illustrating scheme of the interaction between primary electrons and the sample.

The primary electrons, that are incident at the sample's surface, interact with it in a non-destructive way and generate other types of electrons. In the context of image formation, the mode used in this work, the secondary electrons are the most important. They are generated by inelastic collisions and are very easily collected using a positively biased collector [82]. There are, however, other electrons generated during this process, such as the x-ray electrons, the backscattered electrons, the Auger electrons and even electrons generated by cathodoluminescence (emission of ultraviolet, visible or infrared light stimulated by electron bombardment) - see figure 2.8 (B). These electrons can be used to acquire additional information that the secondary ones do not provide. In this work, we will take advantage of the x-ray electrons to perform element analysis in our samples, to confirm what materials are really present at the surface.

2.3.2 Focused ion-beam milling

A focused ion beam is very similar to a SEM, however, instead of electrons, it uses an ion beam to scan the sample. The most common FIB columns are composed by a pair of lenses - to define and focus the beam, apertures - to select beam diameter and current,

deflection plates - that allow the scanning of the beam over the sample, and a high speed beam blanker, that quickly deflects the beam off the sample once the process is finished. The column contains also the liquid metal ion source (LMIS), a Ga-based needle source. During operation, Ga flows from a reservoir to the needle tip originating a cone (Taylor cone), from where the Ga ions will be extracted and directed towards the sample.

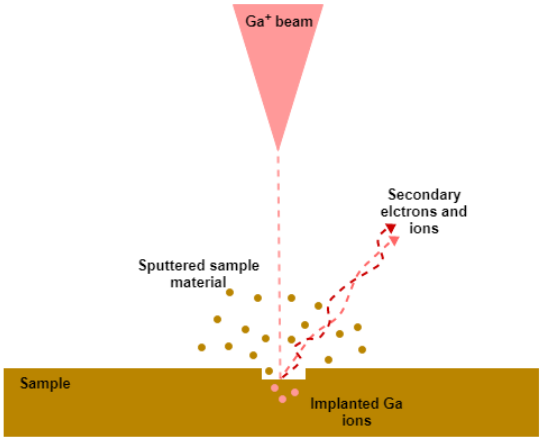


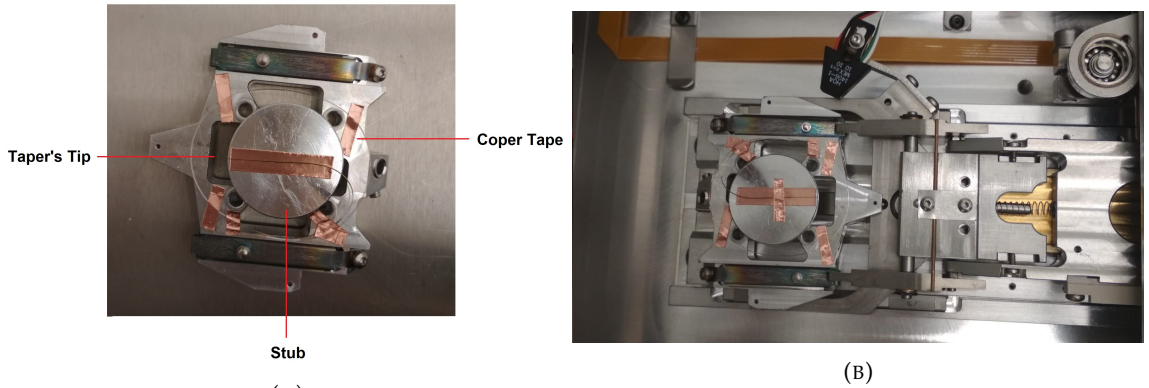
FIGURE 2.9: Scheme of the interactions that occur between the Ga ions and the sample in which thay are incident. The secondary electrons generated may also be used for imaging, much like in a SEM.

When an ion interacts with the atoms of the sample, it loses kinetic energy to a point where it comes to rest in the solid. As consequence, there is one additional process occurring at the same time as the second electron and ion emission and atomic sputtering - the Ga ions are being implanted in the sample, leading to contamination - see figure 2.9.

There is one major drawback to ion beam imaging and machining, the damage the ion beam may do to the sample. If the current used during the raster scanning of a sample is too high it can result in surface amorphization, point defect creations, or grain modifications.

2.3.3 Sample preparation and assembling

The preparation of the sample for micromachining and its safe placement inside the chamber is a crucial step of the tweezers fabrication. Once the fiber is stripped of its protective jacket it becomes very fragile and easy to break if not carefully handled. Once the fibers get to this step they have already been etched and coated in gold, so it is of the essence that the tip of the fiber remains untouched.



(A) (B)

FIGURE 2.10: (A) Tapered optical fiber coated with a layer of 100 nm of gold placed in a planar stub held by coper tape. (B) Placement of the stub inside the FIB chamber.

They were carried in glass slides inside of a protective box to INL, where they were mounted in a circular planar stub, as can be seen in figure 2.10 (A). Copper tape was used to fix the fiber to the stub and also to avoid charge effects. Typically carbon tape would be used to perform such a task, however, it has a very strong adhesion that could not allow us to recover the fiber afterwards. As such, a less sticky material had to be used to secure the safe removal of the taper. The fiber was placed on top of a piece of copper tape, with the taper's tip aligned with the exterior triangular shape of the lower support, and gently pressed against the tape with a metallic tweezer, to ensure complete adhesion. The rest of the fiber was then rolled around the stub, also held by copper tape.

Once the sample preparation was finalized, the FIB chamber was opened and the stub was placed inside it, as seen in figure 2.10 (B). The chamber was then closed and the sample brought to a position where it was ready for manipulation.

2.4 Measurement of optical trapping forces - the drag force method

The mathmatical model used in this thesis to calculate the optical forces acting on the trapped particle is based on the revised Stoke's equation, known as Faxen's law [15, 83]. According to it, the total optical force results from two different contribution: the inertial force and the drag force:

$$F_{opt} = F_{inert} + F_{drag} = m\frac{\delta^2 s}{\delta t^2} + \beta\frac{\delta s}{\delta t} \tag{2.5}$$

where m is the mass of the particle, $s(t)$ the trajectory it describes and β is the viscous drag coefficient given by:

$$\beta = 6\pi\xi\eta r. \tag{2.6}$$

This drag coefficient, besides depending on the particle's radius (r) and the medium viscosity (η), which for water has a value of 8.90×10^{-4}, also includes a correction factor, due to the proximity to the trapping chamber's surface (h):

$$\xi = \frac{1}{1 - \frac{9}{16}\left(\frac{r}{h}\right) + \frac{1}{8}\left(\frac{r}{h}\right)^3 - \frac{45}{256}\left(\frac{r}{h}\right)^4 - \frac{1}{16}\left(\frac{r}{h}\right)^5}. \tag{2.7}$$

This correction is included because the model considers the particle to be close to a boundary of the trapping chamber. In the present case there will be no trapping chamber, *per se*. There is a drop of solution placed in a glass slide, so we will consider such glass slide to be the limit of our "chamber".

Now, if we take a look at the inertial component, we can see that it is negletible when compared to the drag one. Let's consider the Reynolds number (Re) for this case. The Reynolds number is a constact factor given by:

$$Re = \frac{2rv\rho}{\eta}, \tag{2.8}$$

that represents the ratio between inertial forces and viscous forces. Looking at the typical velocity values found in this thesis $\approx 1 - 2\mu m/s$ and the particle's radius $r \approx 0.5 - 1\mu m$ we found a value of $Re \approx 10^{-6}$.

As a consequence we can consider the optical force acting on the particle to be given by:

$$F_{opt} = F_{drag} = 6\pi\xi\eta rv. \tag{2.9}$$

2.4.1 Data acquisition and processing

To determine the value of the force acting on the particle we then need to record the displacement of an isolated particle under the actiong of the laser. For that effect we have the CMOS camera recording. Initially the laser is off and no action is observed, then we turn it on and the particle moves towards the tweezer. That process is repeated around 7 times.

Once we have the videos of the particle's trajectories, we then need to process the information they contain. Using the ImageJ software MosaicSuite for particle tracking

in the video file, the trajectories of the particles are retrieved and are written in terms of coordinates [84]. These sets of data can then be fitted to a Langevin equation from where the particle's velocity can be determined. Once we acquired the velocity, the force calculation is straightforward from equation 2.9.

Chapter 3

A simulation-based study of the trapping forces at a nanoscale

Before blindly diving into experimental work, some computational simulations to study the force fields acting on the particles were performed. The goal was to better understand the phenomena of optical trapping at the nanoscale and in doing so, design a path that would allow the optimization of the experimental resources.

The majority of the simulations presented here are an attempt of emulation of the experimental reality. Probe geometrical parameters were varied throughout the study to understand how it would affect the trapping results.

This chapter is organized into three main parts. In the first one, the configuration of COMSOL Multiphysics utilized to calculate the electric field distribution is presented, followed by the mathematical method used to determine the forces acting on the particle and the python scripts built to perform the calculations. The second part is dedicated to presenting, discussing and comparing all the simulations results obtained. The main conclusions are presented at the end.

3.1 COMSOL Multiphysics

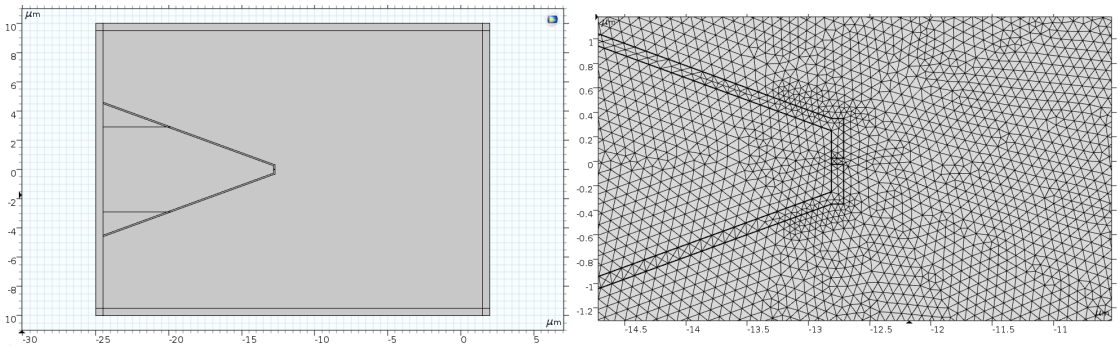
The calculation of the electric field distribution over the areas surrounding the test particle was performed using COMSOL Multiphysics software. COMSOL Multiphysics is a comprehensive simulation software environment for a very large amount of applications. One of its main advantages lays on a very intuitive and user-friendly interface and the capability of simulating multiple scientific models.

For the purposes of this work, the *Wave Optics* interface was used, from which the *Electromagnetic Waves, Frequency Domain (ewfd)* option was selected, to perform a frequency domain study. To run such study some parameters, such as wavelength and refractive index needed to be defined (see table 3.1) and a geometry had to be built.

λ	980 nm
n_{core}	1.45660 @ $\lambda = 980$ nm
$n_{cladding}$	1.45081 @ $\lambda = 980$ nm
ε_0	8.85419×10^{-12} F/m
n_{gold}	$0.27047 + 6.03950i$ @ $\lambda = 980$ nm
$n_{polystyrene}$	1.58 @ $\lambda = 980$ nm

TABLE 3.1: Wavelength and refractive indexes used in the COMSOL simulations.

During the process of defining the problem geometry, experimental issues had to be considered. As the goal was to work with metal-coated optical fibre tapers with nanometer apertures, these had to be included in the simulation. Since the tapers were fabricated by chemical etching, the assumption was made that the core was not affected by the HF for diameters above 5.8μm - the core diameter of the fibre (Thorlabs SM 980-5.8-125). Below that value, the core diameter starts to decay until it reaches its minimum value at the taper's tip. This way, we made a clear distinction between the core's and the cladding's refractive indexes.



(A) (B)

FIGURE 3.1: (A) Exemple of a COMSOL geometry used in the simulations. (B) Closer look at a triangular mesh built aroud a 50 nm aperture.

In figure 3.1 (A) a geometry example is presented. We can still see the part where the core remains unchanged and a little of the cladding that surrounds it. Afterwards, the core begins to decrease until it reaches a diameter of 500 nm. A layer of 100 nm of gold was also included, with a 50 nm aperture at the tip's apex. The polystyrene particle is not represented in this particular image, but it will always be placed to the right of the taper.

To prevent the solution from diverging a *perfectly matched layer* was created around the simulation environment [85], represented by the external layer of the rectangle in figure 3.1.

The next step was to assign a material to each domain of the geometry. To do so, one can either select a material from an already existing library or define a blank material from its physical properties. In these simulations, water was chosen from the existing library as the surrounding material, and both the fibre materials and the gold were defined by their refractive index, as given in table 3.1. A triangular mesh was chosen for this problem with an element size ranging from 0.12 nm to 98 nm, with a maximum element growth rate of 1.3. The mesh was created automatically and as it can be seen in figure 3.1 (B), it becomes denser in the regions where more fine details exist, namely near the aperture and near the gold edges, at the taper's apex.

The three-component vector of the electric field resulting from the excitation of a Gaussian beam in the paraxial approximation was then calculated using the frequency domain study. The results were exported as text files containing the electric field norm for each point of a grid of 1000×400 elements.

3.2 Force calculation method

The main purpose of this chapter is to understand how the forces acting on a given test particle look like for different experimental configurations. To do so we need to know how to calculate the resulting optical force.

To compute the force resulting from the action of an electromagnetic wave on a particle, a microscopic approach based on the Lorentz force was used, as presented in references [15, 86, 87]. The Lorentz force acts on each microscopic dipole that constitutes the particle [88], and its density per unit volume is given by

$$f^d = (\overrightarrow{P}.\nabla)\overrightarrow{E} + \frac{\delta}{\delta t}(\overrightarrow{P} \times \overrightarrow{B}) \tag{3.1}$$

where $\overrightarrow{P}$, $\overrightarrow{E}$ and $\overrightarrow{B}$ are the polarization, the electric field and the magnetic field, respectively. When combined with Maxwell's microscopic equations, equation 3.1 yields the expression

$$f_i^d = P_j \nabla_i E_j + \frac{\delta}{\delta t}(\overrightarrow{P} \times \overrightarrow{B})_i \tag{3.2}$$

where the indexes i and j denote spatial components.

Defining the polarization as $\overrightarrow{P} = \epsilon_0(\epsilon - 1)\overrightarrow{E}$, and taking into consideration that we are dealing with an electrostatic problem, the temporal dependence will vanish and equation 3.2 can be rewritten as

$$\overrightarrow{f}_i^d = \frac{1}{2}\epsilon_0(\epsilon - 1)\nabla \overrightarrow{E}^2. \tag{3.3}$$

The last step comes from the fact that we are using monochromatic radiation. For such case, the electric field can be given as the real part of a complex macroscopic field, and so we arrive at the final expression

$$f_i^d = \frac{1}{4}\epsilon_0(\epsilon - 1)\nabla_i |E|^2 \tag{3.4}$$

used to calculate the force acting on each one of the dipoles.

It is important to mention that these calculations were performed for forces acting on a medium described by a dielectric constant ϵ. In the particular context of this work, we wish to analyse the electromagnetic forces acting on a particle of dielectric constant ϵ_p that lays in a medium with a constant ϵ_m, and so the final expression yields:

$$f_i^d = \frac{1}{4}\epsilon_0(\epsilon_p - \epsilon_m)\nabla_i |E|^2. \tag{3.5}$$

3.2.1 Python scripts

From the COMSOL Multiphysics layout described above, we were able to determine the matrix of values of the electric field. Such matrix was exported in a 1000×400 format, meaning that the simulation box was divided into 1000 points in the x axis and in 400 in the y axis, and for each point, a value of the electric field norm was assigned.

To arrive at the completed force maps presented in the next sections, a COMSOL study was run for each position of the particle. As we were dealing with a very large amount of data, a python script was developed to handle it. The script determined the value of the resulting force acting on the particle at a given position, and in the end, a plot is returned, presenting an arrow at each analysed position. Such arrows represent the direction and the relative magnitude of the force (arrows were normalized to fit the plot).

3.3 A 3D view of the problem

Even though our idea was always to study a two-dimensional (2D) simulation of the problem and then extrapolate to the three dimensional (3D) case, we had to first look at the general picture and analyse the field behaviour in a 3D model, to understand how the light would propagate to the outside. As such, small 3D simulations were run, to evaluate the situation. Given the memory limitations of our computers, we had to reduce our geometry to the essential - the final part of the taper, leading to its apex - just enough to represent the problem and allowing us to have a very fine mesh, necessary for the solution to converge.

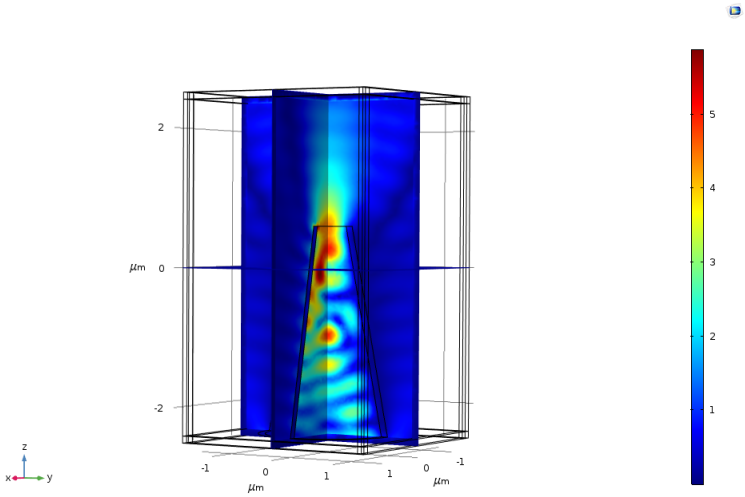
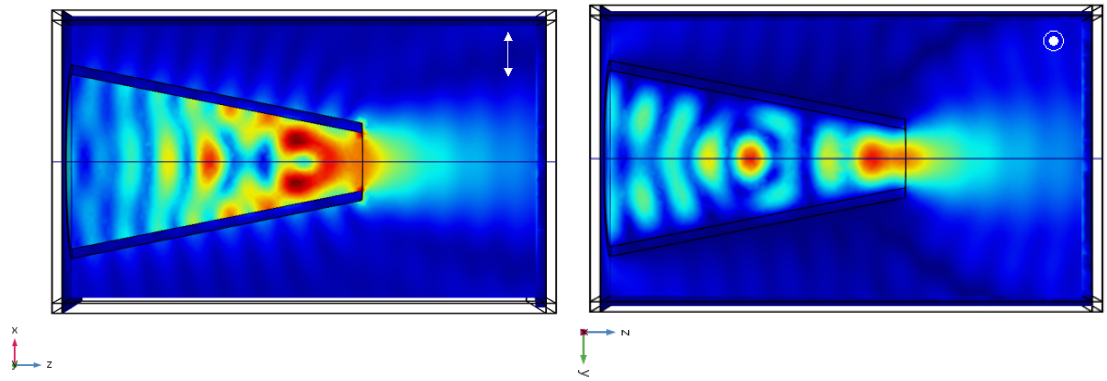


FIGURE 3.2: Electric field norm calculated for a 3D geometry of a taper with apex and aperture diameters of 600 nm.

The result of such simulation can be viewed in figure 3.2, where 3 planes of the solution are plotted, namely planes $x = 0$, $y = 0$ and $z = 0$. It is clear that the field presents a different intensity profile for planes xz and xy - see figure 3.3 for more detail. This asymmetry in light distribution is related to the polarization of the light and was also observed, for example, in references [34, 49, 89].

In figure 3.4, the polarization vector was plotted at the taper's entrance. As can be seen, the polarization at the taper's entrance is along the x-axis, meaning that it is always parallel to the surface defined by the interface between the silica and the water. It will, however, be either parallel or perpendicular to the interface between silica and gold, depending on the observation plane.

For the case of the yz-plane, we have the electric field parallel to the dielectric-metallic interface. Given that the tangential component of the electric field must be continuous



(A) (B)

FIGURE 3.3: Electric field norm for planes (A) xz and (B) yz. The color legend and grid dimensions are the same ones presented in figure 3.2.

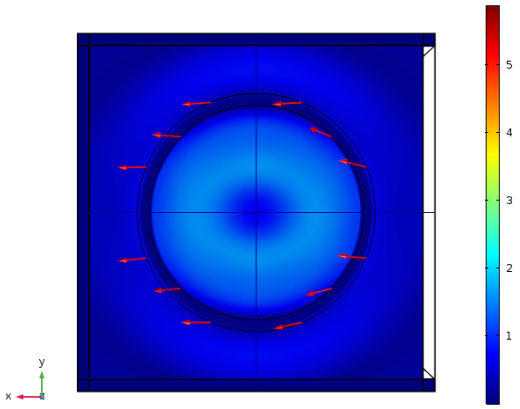


FIGURE 3.4: Representation of the polarization vectors at the entrance of the taper.

through an interface, as given by the relation [90]:

$$n \times (E_2 - E_1) = 0 \tag{3.6}$$

where mediums 1 and 2 are the silica and gold, respectively, there will be no charge build-up at the interface - figure 3.2 (B). As for the xz-plane, we have larger field components perpendicular to the silica-gold interface. Since the incident light drives free electrons in metal along the direction of polarization, there will be a charge accumulation on the surface of the metal, as given by [90]:

$$(E_2 - E_1) \cdot n = \frac{\sigma}{\epsilon_0} \tag{3.7}$$

leading to the excitation of a localized surface plasmon.

3.4 A 2D evaluation of the problem

Our 3D simulations lead us to the conclusion that the optical output field is not centre-symmetric. It is, in fact, polarization-dependent. As such, it will have a different distribution depending on the observation plane. The aim of the study presented from here on now is to determine how this polarization will affect the optical force spatial distribution and to understand what is the best geometrical configuration for our goals. However, given the computational time of a single 3D simulation, we wished to work with a 2D model. Since the scope of this work does not involve the development of exact computational models and in this chapter we are only aiming for a qualitative analysis of the output field of the tweezers, a 2D simulation should suffice. Therefore, the model presented in this section restricts the complexity of the problem to two dimensions and although electromagnetic field propagation differs from 2D to 3D, similarities exist that approximate to experimental reality. In reference [89] a correspondence between field distributions of a circular aperture and a slit aperture across the two principle polarization directions (s and p) was found. As such, it is safe to assume that the output field patterns from the circular aperture (3D) and the slit model (2D) will have a certain degree of similarity that satisfies our needs to perform a qualitative study of properties such as relative gradient and intensity variations and the form of the force maps.

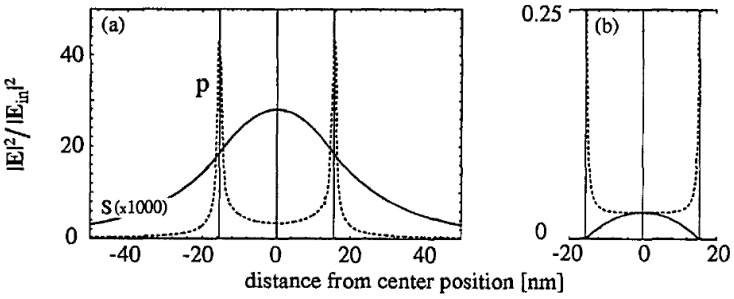


FIGURE 3.5: $|E|^2$ in the aperture exist plane: (left) two-dimensional-model SNOM and (right) ideal circular aperture [89].

As a consequence of the influence of polarization, in order to work with 2D simulations, one must evaluate the problem from the two observation planes correspondent to the principle polarizations. It is thus crucial to clarify the terms that will be used throughout the remains of this chapter to identify them. The observation plane perpendicular to the polarization is the s-polarization plane, and the observation plane parallel to the

polarization is the p-polarization plane - consider figure 3.5. In reality, both polarizations will be present at the output of the taper, as a combination.

3.4.1 The influence of the taper angle on the transmitted field

As the first step of this study, the focus was set on the taper's shape, namely on its angle. We wanted to observe how the taper's shape influenced the output beam. Besides the angle, two other properties were varied throughout the study: the diameter of the taper's apex (d), and the aperture in the gold coating layer (a), as can be seen in figure 3.6. Therefore, for a fixed angle, different apex diameters were simulated, and for each such apex diameter, different aperture diameters were considered.

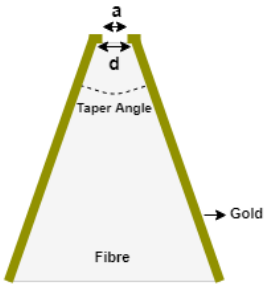


FIGURE 3.6: Scheme of the taper's geometry.

In performing this study, two physical quantities were considered. The first one was the maximum value of the squared norm of the electric field outside the aperture, which, being proportional to the intensity, is an indicative of the taper transmission. The second, and most significant one, is the maximum gradient value of the squared norm of the electric field found outside the aperture. As the resulting force acting on the particle is proportional to this quantity, it will be an indicator of how strong the forces will be for each configuration. These points will always be in close proximitty to the taper's aperture. Both values were acquired from the matrix of values extracted from the COMSOL simulations.

The results obtained for the taper with a cone angle of 20^o are presented in figure 3.7. Looking at plots (A) and (B), that present the values found for the s-plane, both data seem to agree that the best aperture values for all apex diameters are somewhere around 300 nm. However, for larger apertures, the results diverge. While the intensity plots ($I \propto |E|^2$) decay by only a small amount, relative to its maximum value, the gradient shows a slightly larger decay. In practice, it means that in spite larger apertures being able to transmit a bigger amount of light, as can be seen in the bigger spot in figure 3.8 (B), the beam intensity will not decay as fast along the propagation direction. This is a consequence of diffraction - the more the field is laterally confined, the faster it will diverge [20]. As such, because the spectrum of a strongly confined field mainly contains evanescent components that exponentially decay along the propagation axis, the field from the source will decay and diverge very rapidly along the optical axis - figure 3.8 (A).

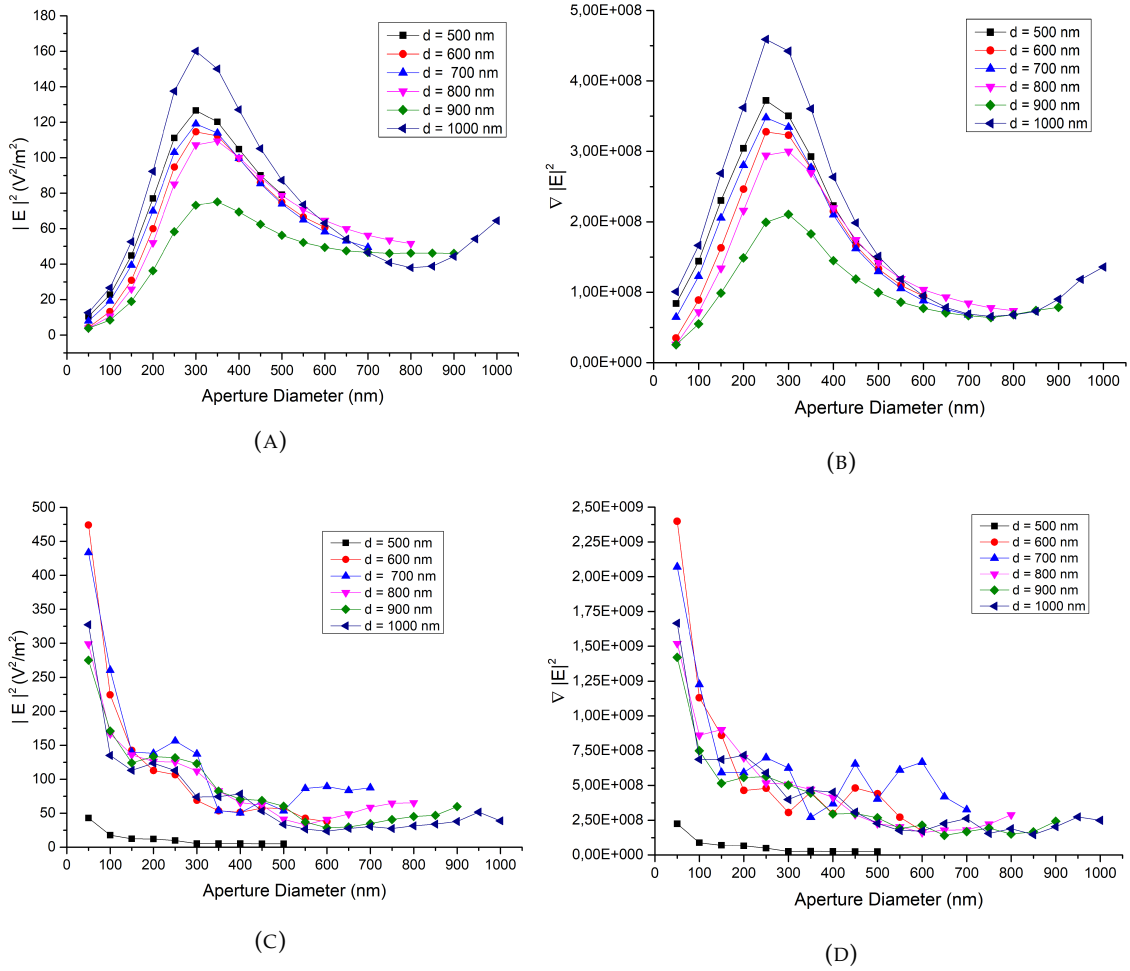


FIGURE 3.7: Intensity (A), (C) and intensity gradient (B), (D) maximum values registered for tapers with 20º cone angles. Plots (A) and (B) are relative to the s-polarization plane, and plots (C) and (D) to the p-polarization plane.

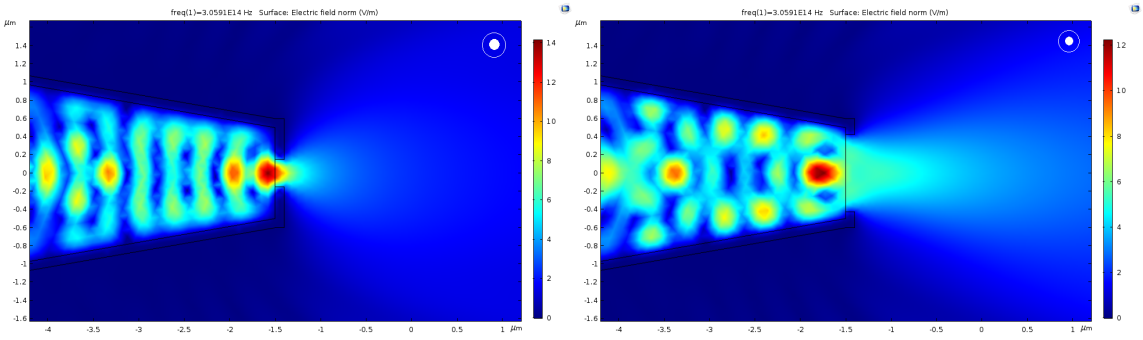
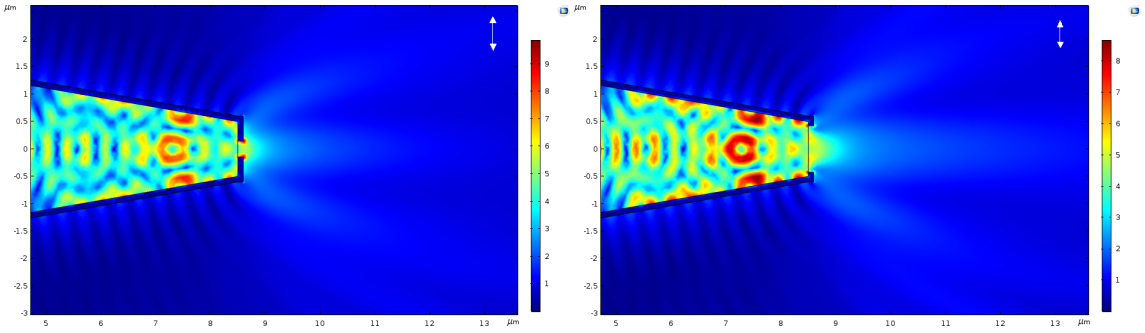


FIGURE 3.8: Electric field norm for a 20º taper with an apex diameter of $d = 1\mu m$ and (A) $a = 300nm$; (B) $a = 850nm$ in the s-polarization plane.

As for plots (C) and (D), relative to the p-plane, the behaviour is much different from that seen in the ones for the s-plane. Even though we also observe a decaying for larger apertures, due to the diffraction effects, there are some other questions to be considered here. When compared to the s-polarization plane, the registered values of intensity and intensity gradient for very small apertures are very high in this plane. That is a direct consequence of the charge build-up effect near the edges of the aperture, as can be seen in figure 3.9.



(A) (B)

FIGURE 3.9: Electric field norm for a 20º taper with an apex diameter of $d = 1\mu m$ and (A) $a = 300nm$; (B) $a = 850nm$ in the p-polarization plane.

This is a very strong indication that if we ever wish to trap particles below 50 nm these will most likely be the ideal apertures to use. Given the presence of strong localized surface plasmons at the aperture's edges, there will exist a very localized and rapidly decaying field in that region, resulting in large gradient values. However, given our interest in trapping particles around a few hundred nanometers, and considering also our initial experimental limitations, we focused our attention in the region of the plots where a is larger than 500 nm. This way, the aperture can be slightly larger than the particle to trap, allowing the particle to fit in - as discussed in chapter 1.

Figures 3.10 and 3.11 show the results found for tapers with 30º and 40º cone angles, respectively. They present similar behaviour to the one found for the 20º taper, showing, however, lower values.

3.4.2 Results for 20º angled tapers

From the plots of figures 3.7, 3.10 and 3.11, one may immediately infer that the best angle to work with is the 20º. As it presents the higher values of the electric field gradient

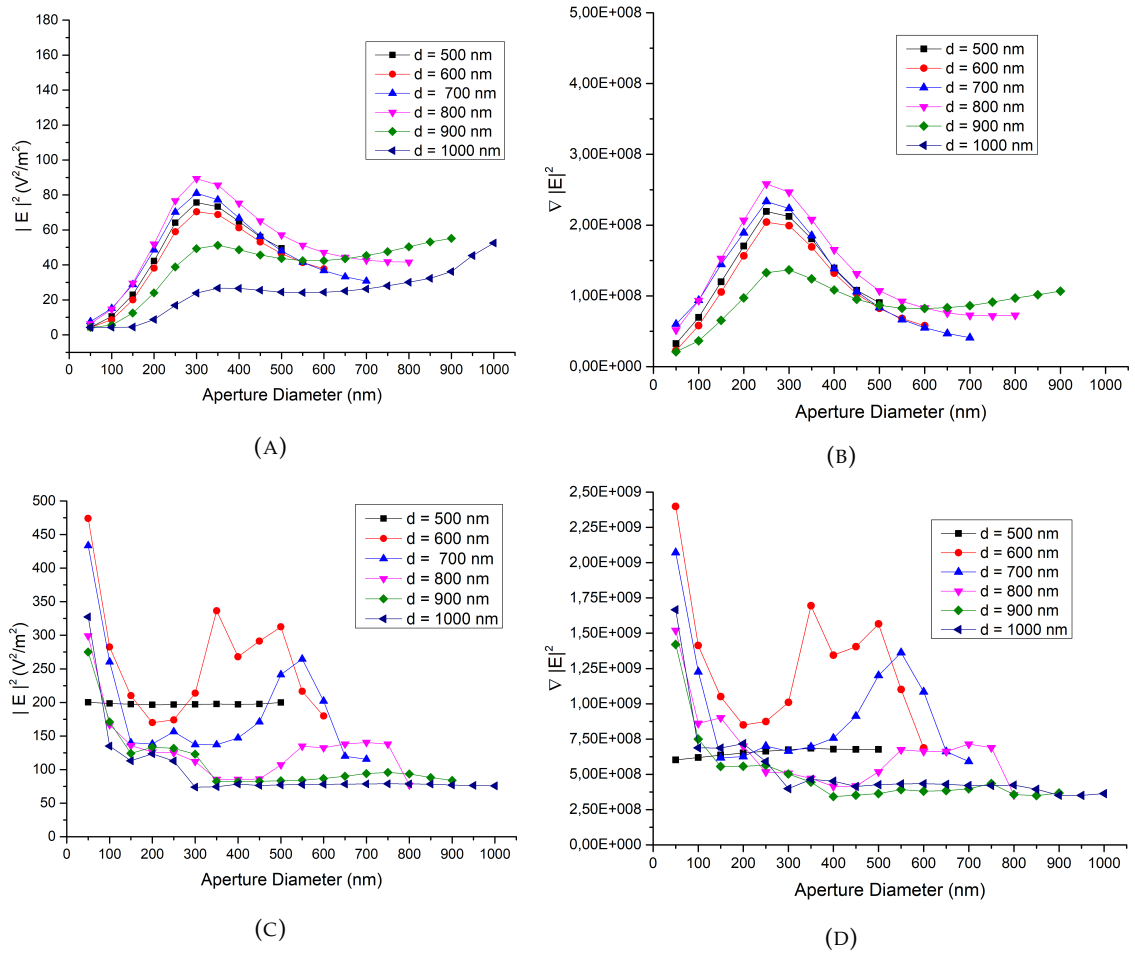


FIGURE 3.10: Intensity (A), (C) and intensity gradient (B), (D) maximum values registered for tapers with 30º cone angles. Plots (A) and (B) are relative to the s-polarization plane, and plots (C) and (D) to the p-polarization plane.

when compared to the others, it will produce stronger forces. But everything in the literature seems to affirm that larger angles will allow for better transmission and henceforth bigger intensity values for larger angles. So what is happening in this particular case?

According to Hetch *et al.*, in reference [61], the power that is delivered to the aperture will depend on the distance between the HE_{11} cutoff diameter and the aperture plane. Such distance is determined by the cone angle of the taper, and so, larger cone angles provide better transmission. The question here is what is the diameter for which the HE_{11} mode enters cutoff. All the results presented in the previous section are for diameters above 500 nm, for which the mode has not entered cutoff yet. Consequently, we can not talk of a distance between the cutoff and the aperture plane, and the cone angle will have a different influence on the problem.

To justify such arguments, a small set of simulations was performed for a taper with an

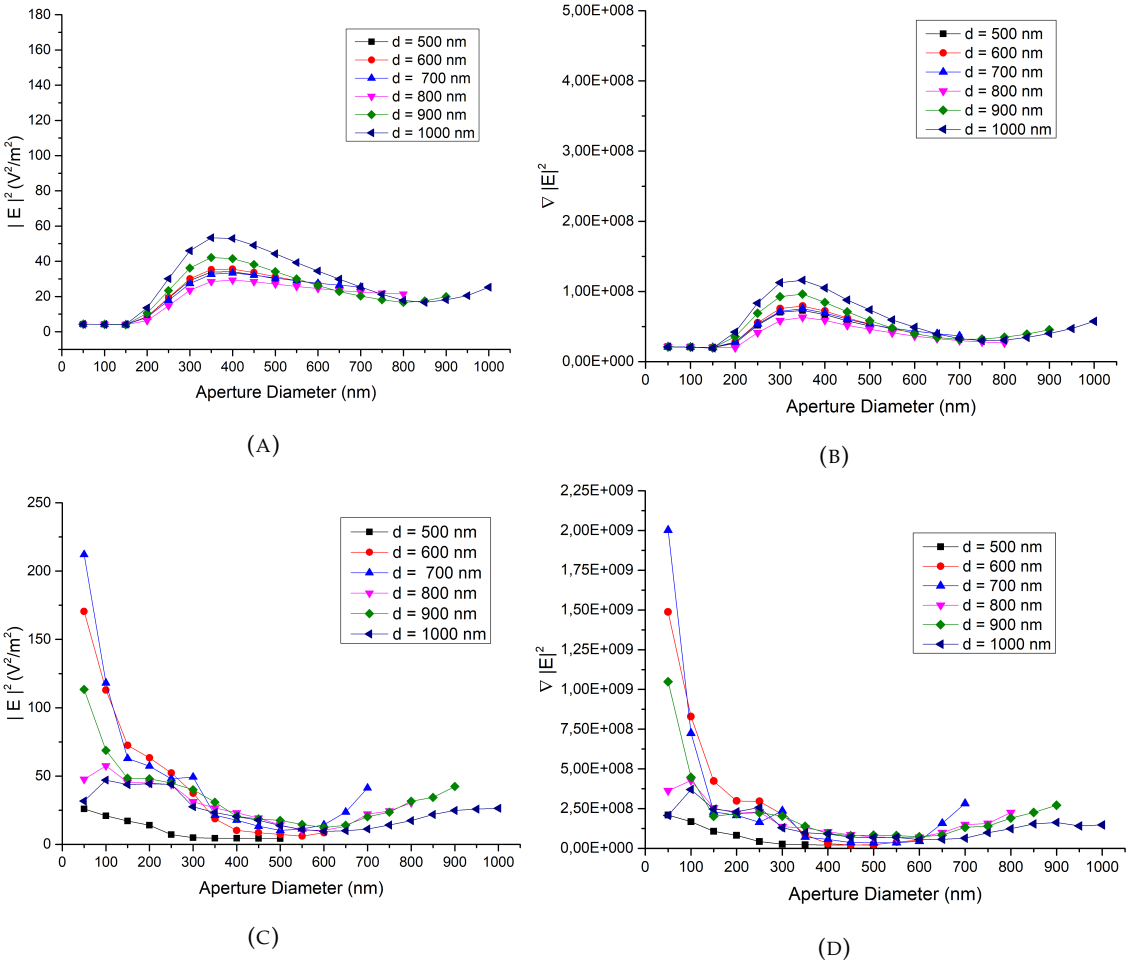


FIGURE 3.11: Intensity (A), (C) and intensity gradient (B), (D) maximum values registered for tapers with 40º cone angles. Plots (A) and (B) are relative to the s-polarization plane, and plots (C) and (D) to the p-polarization plane.

apex diameter of 200 nm, where the HE_{11} mode has already entered cutoff. The field was calculated for the 3 different angles in study, and for each case, the maximum intensity outside the aperture was determined. As can be seen in figure 3.12 the maximum values registered outside the aperture grow with the taper's cone angle, as is expected in the literature. Also, if we take a closer look at the images of figure 3.13 we can see that the distance between the last propagating mode (the spot of maximum intensity inside the taper) and the aperture decreases with increasing angle - under 300 nm for the 40º case and almost 400 nm for the 30º taper.

As we will not be dealing with such small apertures, this effect will not be verified in our tweezers.

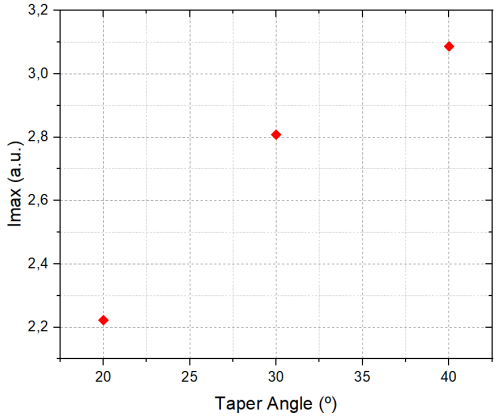
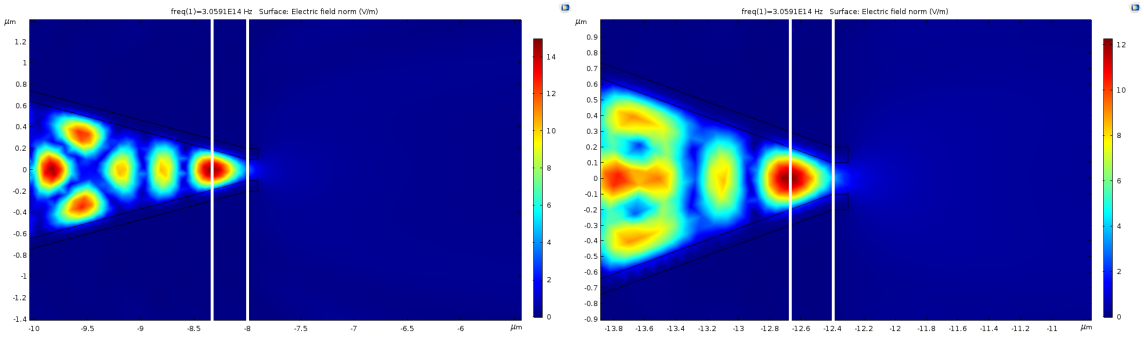


FIGURE 3.12: Variation of the intensity values outside the aperture for a taper with an apex diameter of 200 nm as a function of taper cone angle.



(A) (B)

FIGURE 3.13: Electric field norm simulations for a taper with an apex diameter of 200 nm and a cone angle of (A) 30° and (B) 40°.

3.4.2.1 A comparison with polymeric tips

We wanted to understand how the intensity and gradient values found for this tapered tips compare to the ones obtained with the polymeric tips used in previous works, to trap larger particles ($> 1\mu m$). To do so, a simple simulation of a standard polymeric tip was performed under the same conditions as the ones used for the taper. The tip has a radius of $2.9\mu m$ and a refractive index of 1.52 - figure 3.14.

The maximum values registered for this case were $|E|^2_{max} = 15.210027$ and $\nabla|E|^2_{max} = 3.03E+7$. Comparing these values with the 20° taper, we see that the tapered tips provide intensity and gradient values up to 10 and 15 times larger than the ones found in polymeric tips, considering only the s-polarized plane. This ratio values can vary depending on the aperture diameter of the tweezer, as was shown in figure 3.7, here we used the highest value to determine the highest possible ration. As for the p-polarized, the field

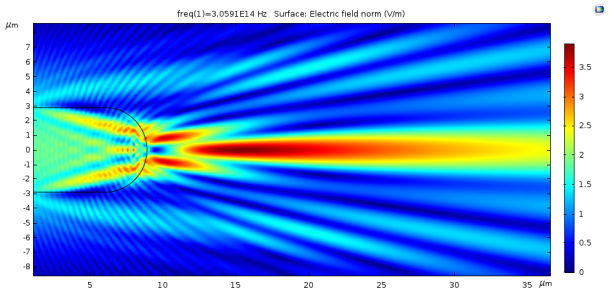


FIGURE 3.14: Electric field norm simulations for a polymeric tip with 2.9μm radius. Polarization is not an issue here, since the field is center-symmetric and there are no plasmonic effects.

enhancement is even greater, as is the gradient, due to the existence of localized surface plasmons. This results are summarized in table 3.2.

This field enhancement so near the aperture and the fast decay that follows guarantees intensity gradient values necessary to trap nanometer particles, as is demonstrated in the next section.

	$\frac{\lvert E\rvert^2_{Taper}}{\lvert E\rvert^2_{Polymeric}}$	$\frac{\nabla\lvert E\rvert^2_{Taper}}{\nabla\lvert E\rvert^2_{Polymeric}}$
$p-pol$	≈ 31	≈ 78
$s-pol$	≈ 10	≈ 15

TABLE 3.2: Squared norm of the electric field and its gradient ratios showing the field enhancements obtained with SNOM like tweezers of 20º cone angle, relative to polymeric ones.

3.4.3 A detailed study of a 20º taper configuration

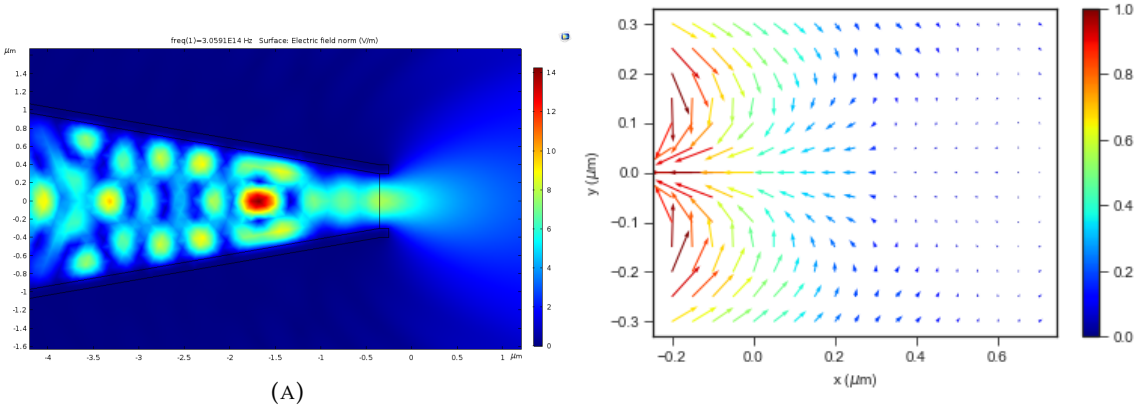
Upon concluding that the cone angle of $\approx 20^o$ would be the best configuration to optimize the trapping forces, a detailed study of optical force fields was conducted. Although we are only treating simulations here, we thought it was important to consider our experimental limitations from the beginning. Thus being, the main focus of this study is on configurations where the aperture diameter matches the apex diameter. Since initially we didn't have a FIB at our disposal, we wanted to be sure that the limiting cases would work.

The force was calculated for two different sizes of polystyrene particles, one with 100 nm in diameter, and another with 500 nm. All the force fields for the limit cases are presented in this section. The main goal was to understand if there was a limiting configuration, for which trapping would no longer occur.

3.4.3.1 P-polarization vs. s-polarization

However, as we saw in previous sections the electric field has a different distribution depending on the plane we are looking at, so we need first to understand how the force maps will differ from each other in each plane.

First, let us consider the case presented in the 3D simulation, a taper with an apex diameter of 600 nm and an equal aperture. Electric field simulations of both planes were performed and the respective force maps were calculated for a particle of polystyrene with 100 nm diameter. The results are presented in figures 3.15 and 3.16. It is important to stress out that the coordinates of the maps correspond to the coordinates of the electric field simulation, so the reader may have a full understanding of the resulting force acting on the particle at each position.

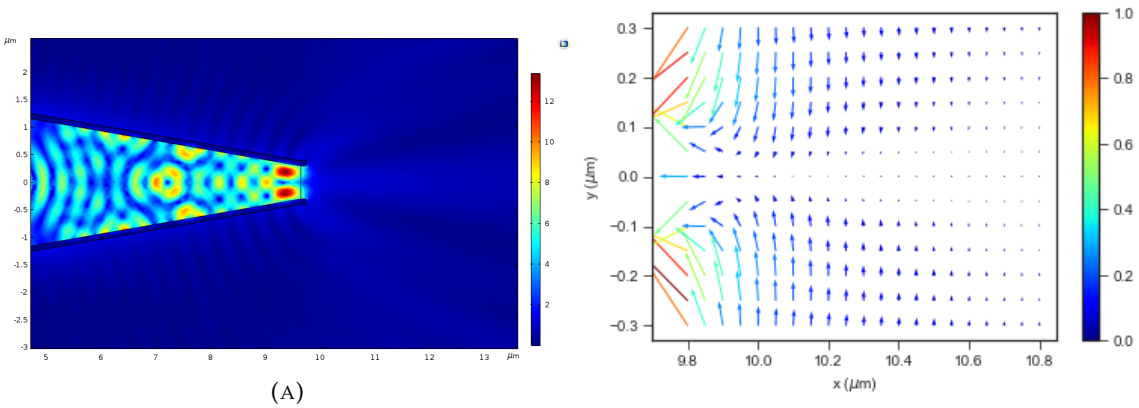


(A) (B)

FIGURE 3.15: (A) Electric field norm in the s-polarized plane for a 20° angled taper with apex and aperture diameters of 600 nm. (B) Force field map for a polystyrene particle with 100 nm in diameter in the electric field of plot (A).

In both cases, we can see the arrows pointing towards the aperture position, indicating the existance of an optical force atracting them towards it. The field pattern is, however, different in each plane, as was expected. While in the s-polarized plane we see the forces pushing the particle towards the centre of the aperture, in the p-plane we can see 3 different spots to where the particle is attracted to, which are stronger but at a much shorter range than in the s-polarization. Once again that is happening because of the charge build-up near the edges, that create the two strong gradients.

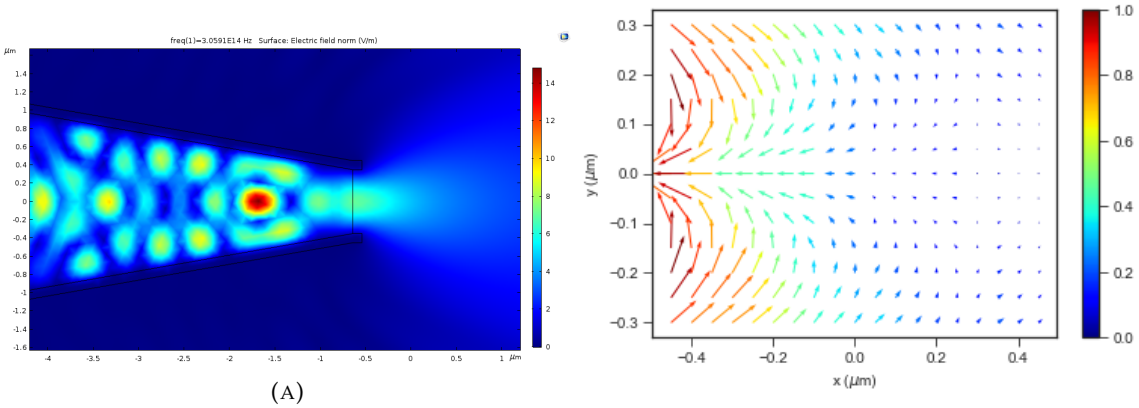
The same type of behaviour was also observed for an aperture of 700 nm - see figures 3.17 and 3.18. Note that in this particular case there is a larger zone, near the aperture,



(A) (B)

FIGURE 3.16: (A) Electric field norm in the p-polarized plane for a 20° angled taper with apex and aperture diameters of 600 nm. (B) Force field map for a polystyrene particle with 100 nm in diameter in the electric field of plot (A).

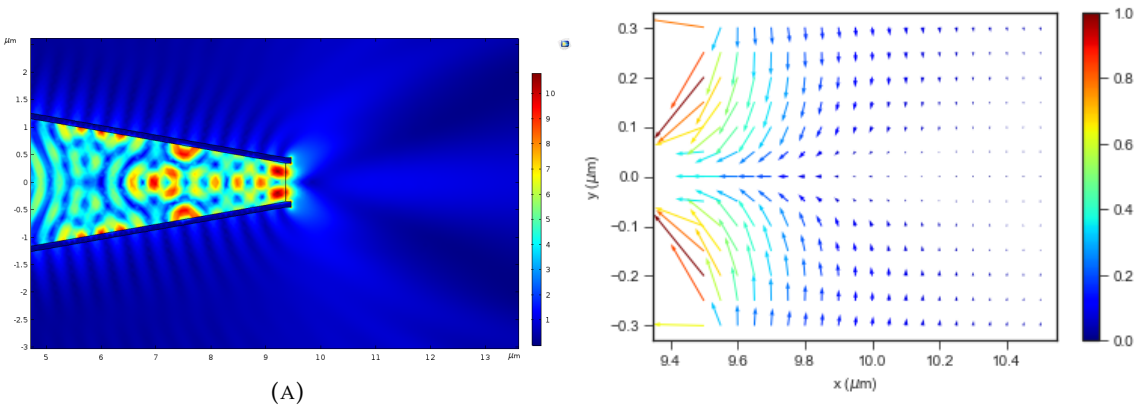
where the force in the p-plane is perpendicular to the plane of the aperture and not pointing to the centre. The same effect was also verified for the 600 nm aperture, but with less significance when compared to the force directed towards the edges. Okomoto *et al.* also observed this type of behaviour [34].



(A) (B)

FIGURE 3.17: (A) Electric field norm in the s-polarized plane for a 20° angled taper with apex and aperture diameters of 700 nm. (B) Force field map for a polystyrene particle with 100 nm in diameter in the electric field of plot (A).

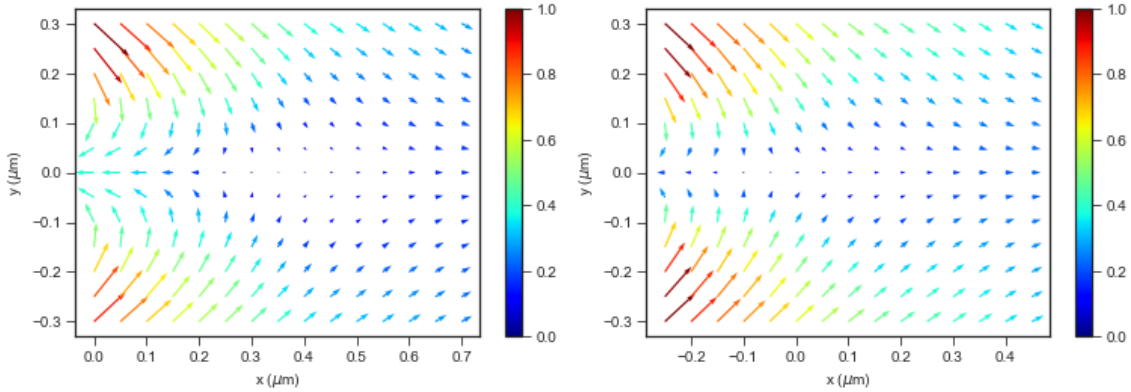
From the results, both planes seem to give enough information to understand if a given geometry will enable trapping or not, and we know that reality will be a combination of both. Since we wanted to find a limiting configuration where trapping is no longer possible, if such configuration exists, we decided to focus our attention on the s-plane, for it is the plane with lower gradient values of the two. As such, the analysis in the next section is focused on this plane, for which that force maps for 500 nm polystyrene particles



(A) (B)

FIGURE 3.18: (A) Electric field norm in the p-polarized plane for a 20° angled taper with apex and aperture diameters of 700 nm. (B) Force field map for a polystyrene particle with 100 nm in diameter in the electric field of plot (A).

were also calculated - figure 3.19.



(A) (B)

FIGURE 3.19: Force field maps for polystyrene particles with diameters of 500nm positioned in front of a taper with apex and aperture diameters of (A) 600 nm and (B) 700 nm.

3.4.3.2 Comparing the force maps for different geometries

For trapping to occur we need to have a balance between the gradient and the scattering forces, that is, either a spot where the resulting force in null or a complete dominance of the gradient component. However, by looking at the maps in figure 3.21 we observe a different behaviour. For both cases, we see a region, near the aperture, where the forces are mainly attractive, in the direction of the aperture itself. In fact, what we are observing is a dominance of the gradient contribution over the scattering one, and so, as the gradient force is directed towards the aperture, so will the total force. This can be viewed

as an axial confinement close to the aperture, which will most likely allow for 3D optical trapping.

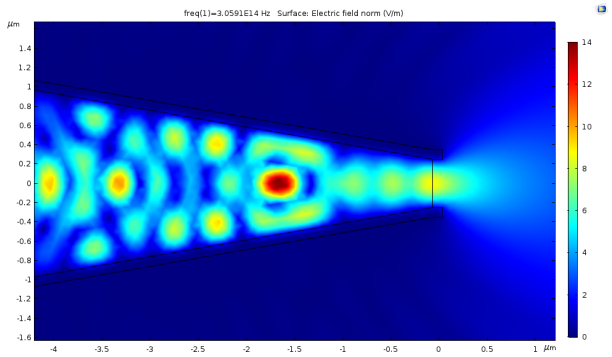
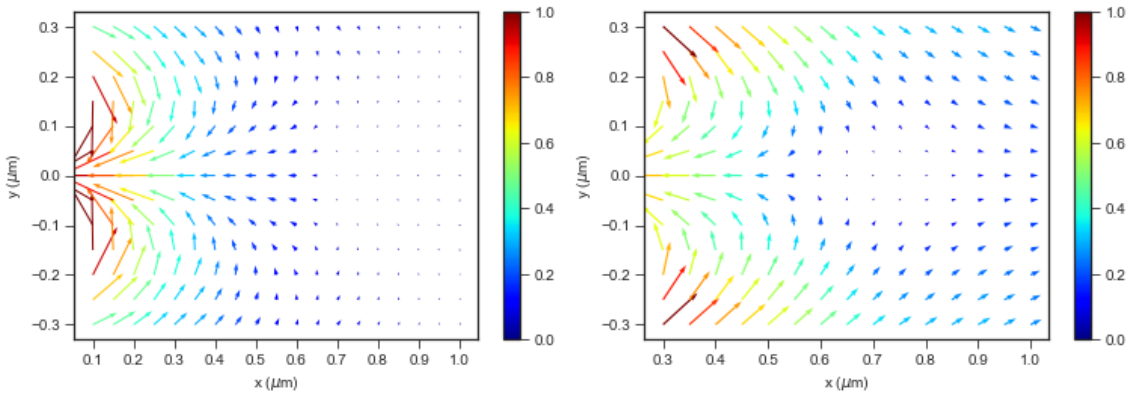


FIGURE 3.20: Electric field norm, in the s-polarized plane, for a 20° angled taper with apex and aperture diameters of 500 nm.



(A) (B)

FIGURE 3.21: Force field maps for polystyrene particles with diameters of (A) 100 nm and (B) 500nm positioned in front of a taper with apex and aperture diameters of 500 nm.

Another visible feature is the existence of a spot with null resulting force, in plot (B). This can easily be explained by the dependence that both gradient and scattering forces present on the particle's radius. While the first one scales with the third power of the radius, the second scales with the sixth power of the radius, and so the scattering force will be less significant for very small particles. Simultaneously, the intensity gradient will be much larger near the aperture and so, the gradient force will overcome the scattering force in that region. As the gradient becomes less significant with growing distance from the aperture, the scattering force gains ground, and so, we may observe a region of null forces. With the increasing distance we observe a region in plot (B) where the scattering force becomes dominant, and the resulting force is repulsive.

The same generalized behaviour was observed for the tapers with apex and aperture diameters of 600 nm, 700 nm and 800 nm, as can be seen in figures from the previous section (figures 3.15, 3.17, 3.19) and figure 3.23. It is, however worth notice that the distance between the aperture and the point of null forces decreases with increasing apertures, which has to do with the field distribution outside the aperture. Again, the simulated electric fields are presented in figures 3.15, 3.17 and 3.22, to give the reader a geometrical reference of the particle's center position relative to the taper.

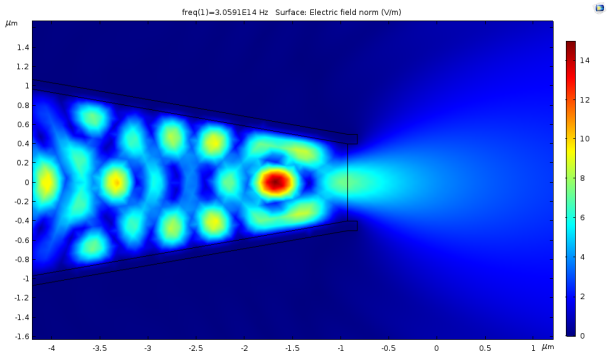
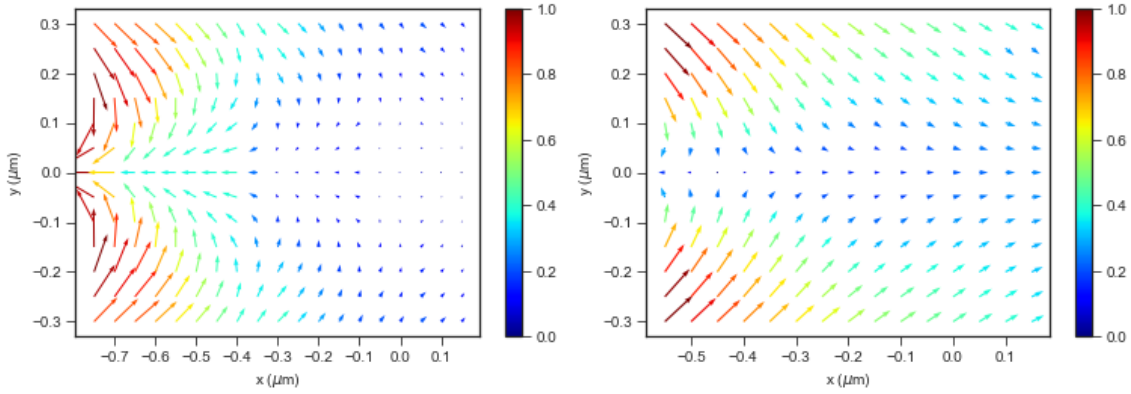


FIGURE 3.22: Electric field norm, in the s-polarized plane, for a 20º angled taper with apex and aperture diameters of 800 nm.



(A) (B)

FIGURE 3.23: Force field maps for polystyrene particles with diameters of (A) 100 nm and (B) 500nm positioned in front of a taper with apex and aperture diameters of 800 nm.

An interesting case is found for a taper with apex and aperture diameters of 900 nm, specifically for the case of the 100 nm polystyrene particle. Focusing our attention in figure 3.25 (A), we observe a behaviour not seen in any of the other plots. We still observe the same transversal confinement, as in the other cases, but now, the axial confinement looks different, and we can identify a specific trapping point along the optical axis, for $x = -0.9\mu m$. This can be understood by looking at figure 3.24, more specifically at the

field pattern outside the aperture, and compare it with the ones presented so far. To design a taper with larger apex diameter, its length will have to be reduced, and so, the optical modes that reach the aperture can vary. In all the other ones there is a field maximum right at the interface fibre-water, but for this particular case, such maximum is located a few hundreds of nanometers away from the aperture. As a consequence there will be an inversion of the gradient sign along the optical axis, resulting in the kind of axial confinement observed in plot (A) of figure 3.25.

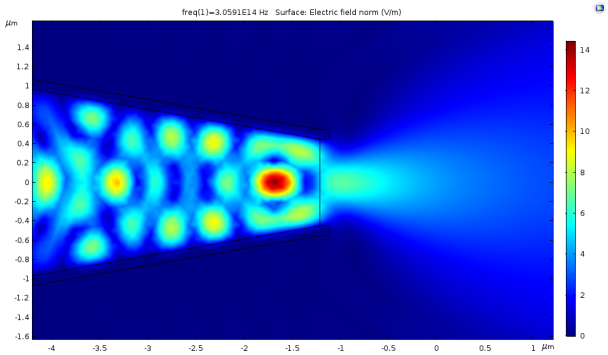
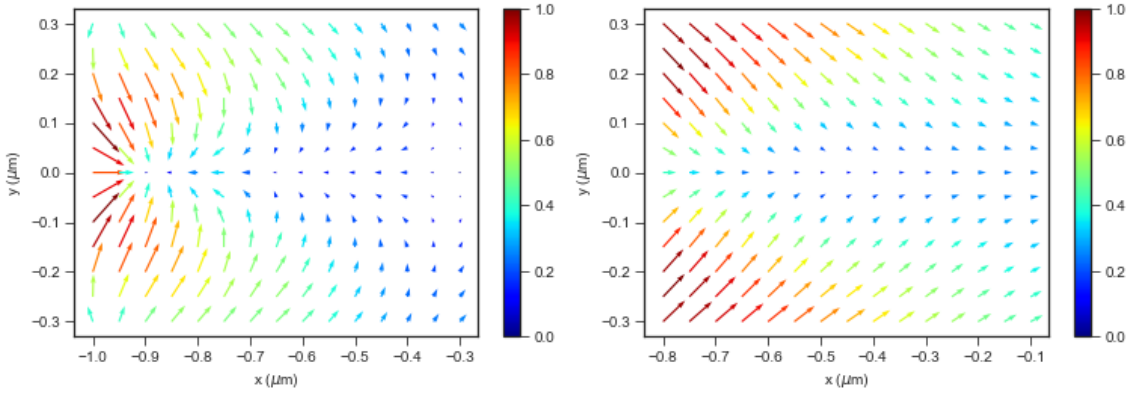


FIGURE 3.24: Electric field norm, in the s-polarized plane, for a 20º angled taper with apex and aperture diameters of 900 nm.



(A) (B)

FIGURE 3.25: Force field maps for polystyrene particles with diameters of (A) 100 nm and (B) 500nm positioned in front of a taper with apex and aperture diameters of 900 nm.

As for the case of the 500 nm particle, plot (B) - figure 3.25 - shows that there will be no optical trapping with such configuration. As previously mentioned, in the presence of a slightly bigger particle, the scattering forces become dominant and the particle will simply be pulled away by the field along the optical axis direction. We have thus found the limiting configuration that may be able to allow trapping of a 500 nm particle to be the one where the taper apex and aperture diameters are smaller than 800 nm. Even for the case of

a 800 nm aperture it is not safe to conclude that optical trapping will occur experimentally, as the magnitude of the forces near the aperture pushing the particle towards it are very small.

For the taper with apex dimensions of $1\mu m$ two different configurations were considered. In the first one, the aperture has the same dimensions as the apex, and we can observe in figure 3.26 that the field has a different shape from the ones seen so far, because of the optical mode reaching the aperture. As a consequence, the optical force maps have different patterns. It is clear from plot (B) of figure 3.27 that the scattering force has completely dominated over the gradient one, and as expected the particle will simply be pulled away from the taper. As for the 100 nm particle, whose force map is presented in plot (A), the data is slightly more difficult to interpret. Given the field pattern, it appears that there are two zones where the gradient dominates, near the two outer maxima. This may indicate that the particle will be trapped around the edges of the taper's aperture, but no further conclusions can be drawn without experimental confirmation.

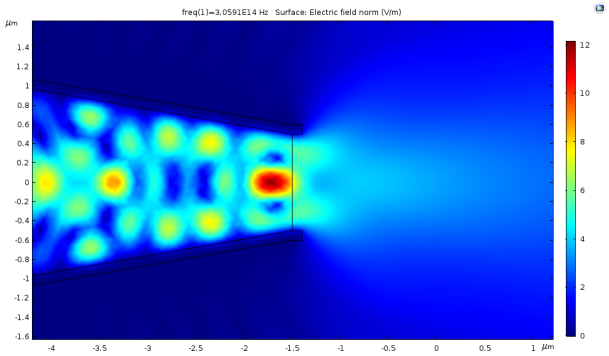
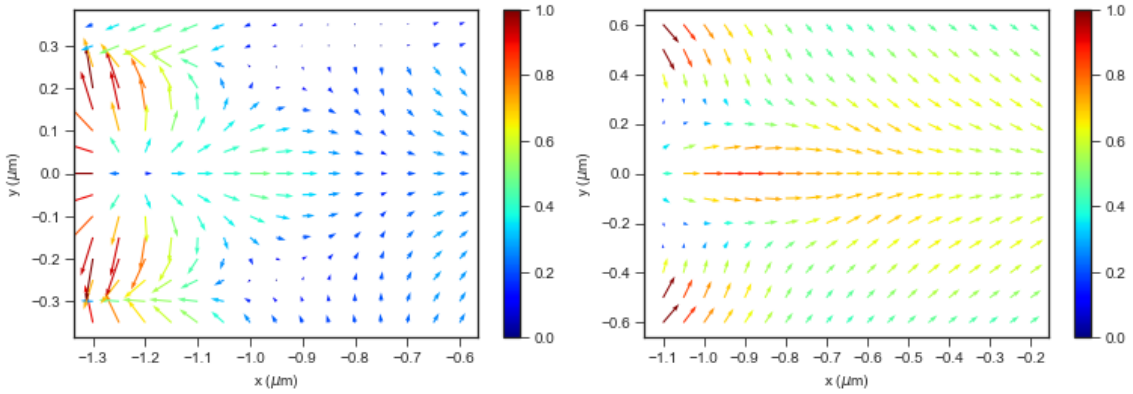


FIGURE 3.26: Electric field norm, in the s-polarized plane, for a 20º angled taper with apex and aperture diameters of 1000 nm.

As for the second configuration, the aperture has a diameter of 250 nm - figure 3.28. The field will be very confined in such a small aperture, resulting in a large gradient over a very small distance from the aperture. As a consequence of such gradient, the resulting forces will attract the particle towards the aperture. As can be seen in the plots of figure 3.29, both axial and transversal confinements are present and are very strong, for the two sizes of the simulated particles.

3.4.4 How will the Cr layer afect the results?

In reality, the gold layer is not directly applied to the taper's surface. Given its slight roughness, an extra layer of chromium (Cr) of about 2 nm is deposited prior to the gold



(A) (B)

FIGURE 3.27: Force field maps for polystyrene particles with diameters of (A) 100 nm and (B) 500nm positioned in front of a taper with apex and aperture diameter of 1000 nm.

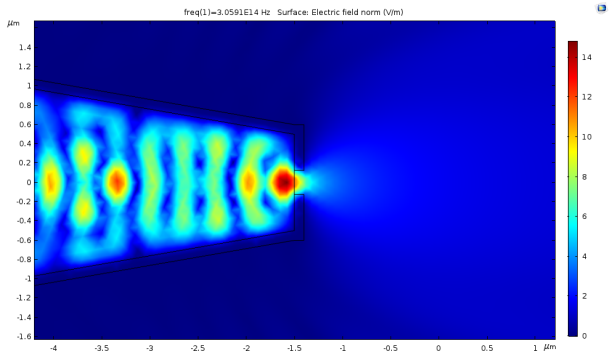
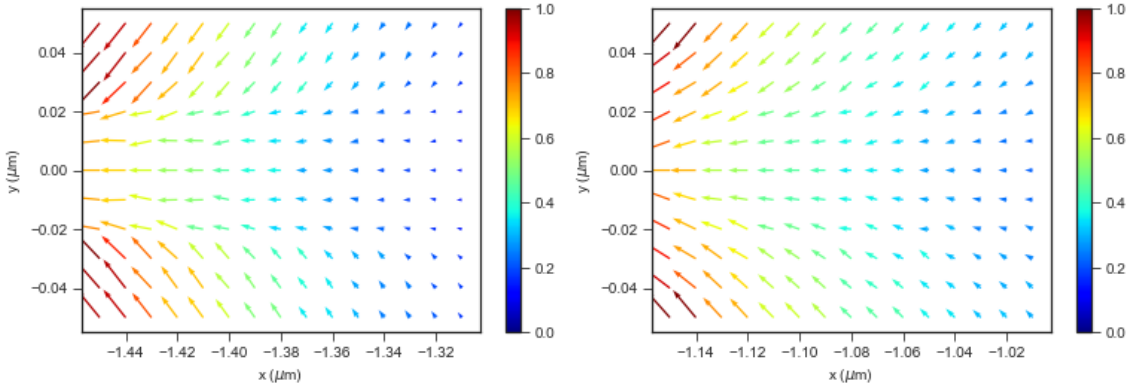


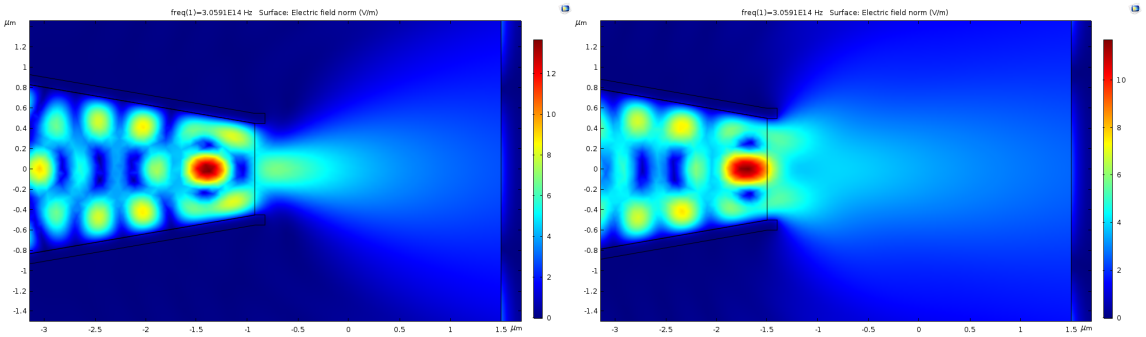
FIGURE 3.28: Electric field norm, in the s-polarized plane, for a 20º angled taper with apex and aperture diameters of 1000 nm and 250 nm, respectively.



(A) (B)

FIGURE 3.29: Force field maps for polystyrene particles with diameters of (A) 100 nm and (B) 500nm positioned in front of a taper with apex and aperture diameters of 1000 nm and 250 nm, respectively.

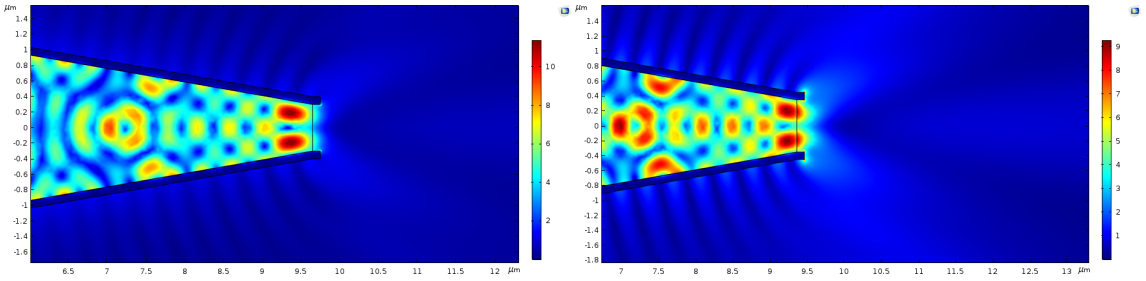
deposition. The evaporation of Cr nucleation centres onto the substrate before the Au deposition is important to inhibit the island growth, that would result in a very rough surface. Since Cr is an oxygen-active material, it will lead to very stable nucleation, resulting in a much smoother surface, and assuring a better gold adhesion [91].



(A) (B)

FIGURE 3.30: Electric field norm, in the s-polarized plane, for a 20º angled taper with apex and aperture diameters of (A) 900 nm and (B) 1000 nm, including a 2 nm chromium layer beneath the gold one.

However, all of the simulation results presented so far did not consider such a layer. Given the very small field penetration into the metallic layers, which can be seen in all the figures of the electric field simulations, it is very unlikely that such a small Cr layer would dramatically affect the results. Nonetheless, some complementary simulations were performed to allow a comparison between the two cases. The refractive index of chromium was considered to be $n_{Cr} = 3.4052 + 3.5678j$ at a wavelength of 980 nm. Here we present only a few of them, namely some of the cases already presented, so the reader can compare them as well.



(A) (B)

FIGURE 3.31: Electric field norm, in the p-polarized plane, for a 20º angled taper with apex and aperture diameters of (A) 600 nm and (B) 700 nm including a 2 nm chromium layer beneath the gold one. Results are very similar to the ones found in figures 3.16 and 3.18, respectively.

As expected there is no significant alteration between the simulations presented in figure 3.30 and the ones from figures 3.24 and 3.26, which leads us to conclude that the results presented are valid. No significant alteration was noticed in the p-polarized plane either, registering just a slight drop in intensity values - figure 3.31.

3.5 Discussion

Throughout this chapter one thing has been made clear, optical trapping of nanometer particles using optical fibre tapers is possible. By confining the optical field at the taper's apex coated with a gold film, intensity gradients can be achieved. Such gradients allow the trap of smaller particles, as was shown in the force field maps presented in this chapter.

Our attention was focus on the geometrical configuration of the taper with a cone angle of 20^{o}, as it was the one that presented the best results regarding the gradient and intensity values. However, this does not mean that other angles will make the trapping of nanoparticles an impossibility, as we shall see later on.

The results seem to indicate that smaller particles will be easier to trap. A quick look at the force maps shows us that the forces acting on the 100 nm particles strongly push the particle towards the aperture, while for the case of the 500 nm polystyrene forces seem to decay in intensity from the 500 nm aperture to the 1000 nm one. While in the beginning we observe the same strong attraction as the one found for smaller particles, as the aperture grows, the force maps change, as a result of the decaying values of intensity gradients created outside the aperture. We thus found a limiting configuration above which trapping of this particles will no longer occur - a taper with apex and aperture diameters of 800 nm. As for the 100 nm polystyrene particles, no configuration was found where trapping would not occur.

We must bear in mind that even though we found some configurations where trapping will not occur in the s-polarized plane, the particle may still be attracted to the edges of the aperture in the p-polarized plane, due to the observed phenomenon of charge build-up. Nonetheless, we have no particular interest in those cases, as one of the goals of this work is to allow the collection of a scattered signal, to differentiate the particle. If the particle is trapped in the edges, a shadow zone may be created, affecting the collected data.

With these guidelines, efforts to fabricate some of the devices simulated were pursued.

Chapter 4

Tapered optical fibre tweezers

Up to this point, the reader has already been presented with some of the experimental methods used in this work and a computational study of the optical tweezers we wished to fabricate. Now comes the time to present the experimental results obtained.

This chapter begins with fabrication considerations, from the selection of the fibre in use to the etching parameters. A detailed description of the process is given, as well as the reasons why other parameters and techniques were left aside. Characterization of the finalized tweezers will follow, giving us an idea of their scattering and transmission properties. The final main section of this chapter is focused on the results of the optical trapping tests.

4.1 Fabrication

4.1.1 The optimization of the etching process

In chapter 2 the proceedings used to perform the etching of the optical fibres have already been described, however, to achieve those parameters an optimization process had to be performed. Several previous tests were made in order to reach the final configuration. In this section we wish to debate those initial tests, comment on the results and show how the path towards the final tapered optical fibres was paved.

4.1.1.1 The tube etching method

The first etching experiments were conducted using a method known as ”tube etching”. In it, the fibre is dipped inside the acid without being stripped of its protective coating layer. The solvent layer on top of the acid also prevents the acid vapour from

spreading to the environment. As the acid begins to etch the fibre, a hollow cylinder is created by the protective coat that can withstand the HF [92]. The main goal of this particular method was to diminish the influence of external factors, such as vibration or temperature, on the resulting taper's shape and consequently obtain a taper with a smoother surface.

We began by performing some preliminary tests using $2.5mL$ of a 48% concentrated HF solution protected by $300\mu L$ of paraffin oil. Two uncleaved fibres were dipped in each cuvette, in a configuration otherwise similar to the one presented in chapter 2, for 90 minutes in an hotte controlled environment. The results obtained showed tapers with apex diameters much larger than those we wanted to obtain - see figure 4.1. We realized that a temporal study was necessary to understand how even slight time variations affected the final shape of the taper.

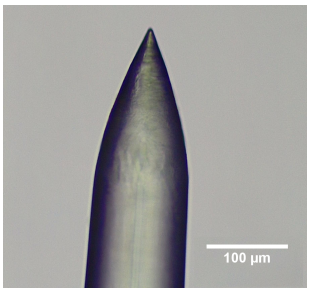


FIGURE 4.1: Optical fibre taper obtained from the first etching test. It has an angle of $\approx 42^{o}$.

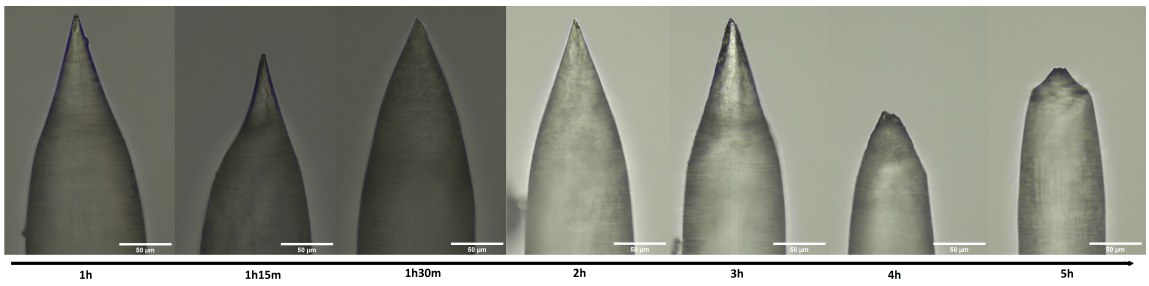


FIGURE 4.2: A study of the resulting shape of the taper for different etching times. HF concentration was 48% and the tube etching method was applied.

The time studies were performed under the already mentioned conditions. All fibres initiated the etching process at the same time but were removed one by one at each chosen interest time. The interest times were initially chosen to be close to the 90 minutes of the initial test and were later broadened to include larger times.

From the results of these studies, one thing was clear, for very large etching times (somewhere above 3h) the taper's integrity is compromised and the formerly formed

structure deteriorates. This is a possible indicator that the process is not self-terminating and it should have been our first clue. Besides that, we began to notice that independent of the etching time, the shape of the taper's apex was never the desired one. It was either too large, or it presented a defect similar to a small cavity - this can be readily observed in figure 4.2 for times 1h, 1h30min, 2h and 3h. Also, the overall taper angles obtained with these fabrication parameters were all above 35^{o}, when we had seen, through the simulation work, that smaller angles would provide better results. As none of the obtained tapers matched the shape requirements we had established we decided to try something different, and so, we lowered the HF concentration.

We diluted the 48% concentrated HF in water to obtain a 30% concentration and proceeded in the same way as before - still using the tube etching method, the pairs of fibres were dipped inside a cuvette containing $2.5mL$ of HF and $300\mu L$ of paraffin oil.

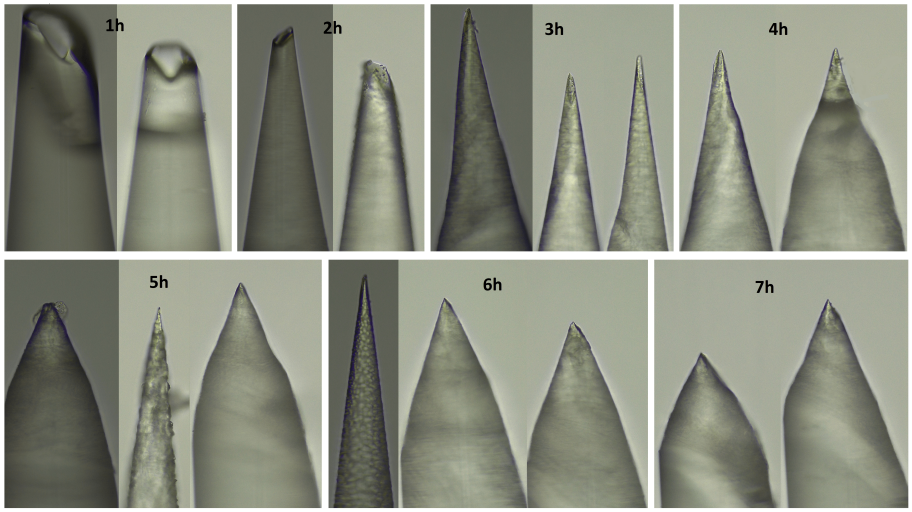


FIGURE 4.3: A study of the resulting shape of the taper for different etching times. HF concentration was 30% and the tube etching method was applied.

We again wanted to see how the taper shape evolved in time under fixed conditions. In figure 4.3 some of the obtained tapers are presented. The destruction of the tip for larger etching times is no longer observed, an indication that the process is happening at a slower rate, but we do see, however, a deterioration in the surface quality. When the fibre is exposed to the acid for longer periods, the surface roughness seems to increase to a point where it can easily be observed through an optical microscope. It is worth noticing that with this concentration a smaller tip apex dimension was achieved in some cases, as well as smaller taper cone angles. Nonetheless, we still observe tip defects in others. Even

though the tapers were fabricated under the same conditions the pairs and trios presented in figure 4.3 for the same etching time present significant differences between each other.

A process with such low reproducibility could delay the work by a significant amount of time. If we could not be sure of the shape of the taper we were fabricating we would just be entering a gambling process until we finally got what we wanted, which could never happen.

We began to wonder if the reproducibility problem had something to do with the tube etching method. So we performed a comparison study between the tube etch and Turner's method [72]. Still using a 30% HF concentration, two fibres were dipped in each cuvette, one was removed of its plastic coating and cleaved; the other was not.

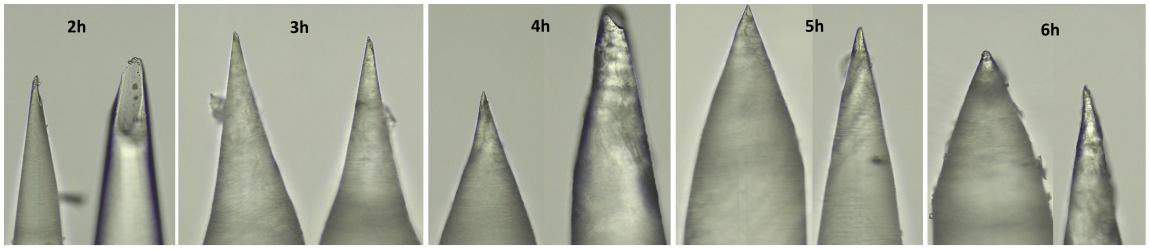


FIGURE 4.4: A study of the resulting shape of the taper for different etching times, for the tube etching method (right) and the Turner's method (left). HF concentration was 30%.

In figure 4.4 the tapers produced by Turner's method are on the left and the ones resulting from a tube etching process on the right. The one thing that intrigued us was the fact the Turner ones appear to present a slightly smoother surface than the others, even though the tube etch claimed to greatly improve the smoothness. After some consideration and some additional experiments and reading, we concluded that the type of fibre, especially the type of plastic coating, played a great role in the process presented in reference [92]. They were using fibres with different compositions than ours, hence the very different results.

Another thing that these first tests insinuated and that later on became apparent is that, as the fibre is cleaved before being dipped in acid the incidence of tip defects greatly decrease when compared with the other method. This probably happens due to the regularity of the bottom surface of a cleaved fibre, and the fact that Turner's method is a self-terminating process.

4.1.1.2 The Turner's method

A new series of etching experiments allowed us to determine the ecthing time as 2 hours for an HF concentration of 30%. Unlike before, we were able to reproduce the etching results for different experiments under the same experimental parameters. The tapers presented in figure 4.5 were fabricated in different days using the same amount of acid and paraffin oil, where they were dipped for 2 hours.

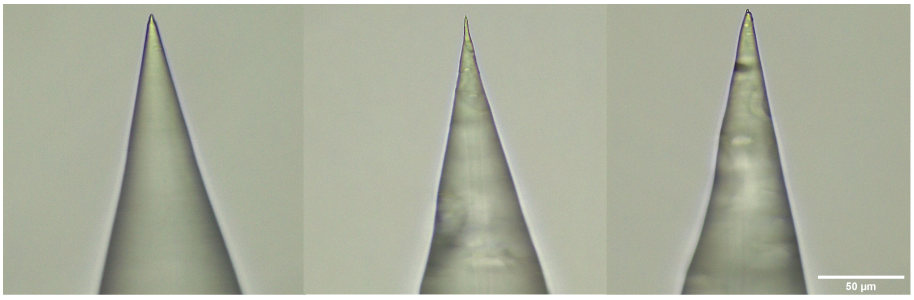


FIGURE 4.5: Tapers resulting from 2 hours long etching processes with HF 30%. They were all fabricated in different days.

Although they are not exact copies of each other, they present similarities in critical parameters, such as the taper cone angle, which in this case lays between 20º and 25º, and the dimension of the taper's apex, that was finally staying below $1\mu m$.

At this point, with a slight improvement achieved in reproducibility, we decided to try changing the oil used to cover the acid, to study how it affected the final angle of the taper. We wished to understand in what direction to go to bring the taper as close to the desired configuration as possible. The oils tested are presented in table 4.1. Up to this point, we had only use paraffin oil, for convenience, as it was available at large quantities in the lab.

Oil	**Density (g/cm^3)**
Paraffin oil	0.842
Olive oil	0.899
Sunflower oil	0.896
10W30 oil	0.846
Silicon oil	0.912

TABLE 4.1: Oils used in the experiment and respective densities. Note that all of them have densities below $1g/cm^3$ (water density), so they can stay above the acid solution.

The oils play an important role when working with Turner's method, as they influence the height of the meniscus that forms at the acid/oil interface. As we have discussed in

chapter 2 this meniscus directly affects the final taper shape, something that did not happen in the tube etching method, as the coating layer prevented the fibre from contacting with the oil.

For each of the oils being tested, 4 tapers were produced and its angles were measured. The medium values and maximum absolute deviations found are represented in figure 4.6 (A). Even though there are slight angular variations for the different oils, in all cases the mean values can be found between 21º and 27º, an interval of just 6º. This can be helpful if we ever wish to perform a fine-tuning of the taper's angle, especially for the cases of the paraffin, olive and sunflower oil, where the absolute deviation presents very small values, but for now, that is not the case. Except maybe for the 10W30, all the tested oils resulted in a taper angle close to the intended one. In terms, this confirms that the factor with the most impact on the value of the angle is the HF concentration, as presented in the graphic from figure 2.2.

We chose to continue using the paraffin oil, as it presented a 22º medium value and the smallest absolute deviation.

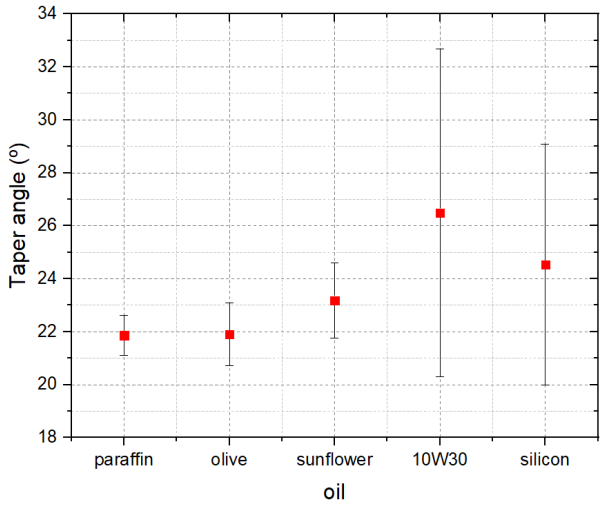


FIGURE 4.6: Taper angles as a function of the type of oil. In every case $300\mu L$ of oil were used.

As the work proceeded and more tapers were fabricated, oddly shaped ones continued to appear, some with no resemblance to a tapered shape whatsoever. Examples of such tapers are presented in figure 4.7. In the search for a solution to this problem, we started to question whether or not it had something to do with the fact that we were etching two fibres, at the same time, in the same confined cuvette volume. Could the two

processes be interfering with each other? Or maybe we needed some agitation in the solution to try to keep it as homogeneous as possible, as the process took place.

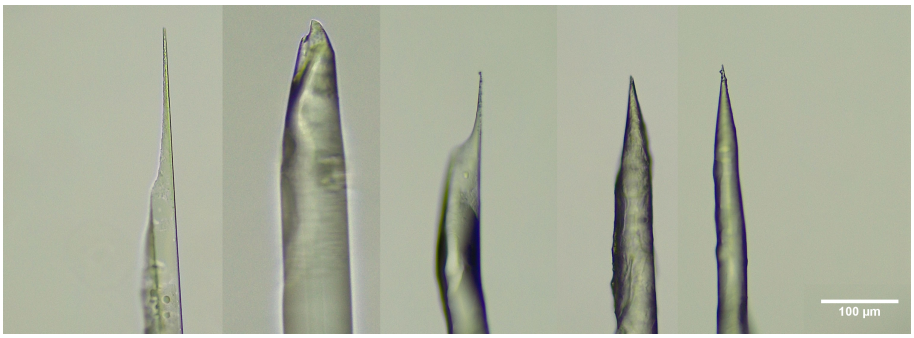


FIGURE 4.7: Oddly shaped optical fibres resulting from chemical etching.

We decided to make 4 alterations to the fabrication process. First, we moved it to a clean room controlled environment, still using an hotte, but inside a cleanroom. Second, the protective layer was increased to $500\mu L$ of paraffin oil. Third, we started placing only a single fibre inside each cuvette; and last, we decided to test the use of ultrasounds applied to the solution.

Although the ultrasounds seemed to accelerate the etching process (registered etching time was 1 hour and 45 minutes) and even contributed to smoother surfaces in the case of higher HF concentrations, in the majority of the situations the oil ended up mixing with the acid, originating a homogenously white opaque solution. In practice, this means that the oil layer, that is supposed to protect the taper once the process is finished, has been compromised to the point where it no longer exists and the etching process continues in areas where it should have stopped. For HF concentration of 30%, or lower, the etching times are too long and this mixture seriously deteriorates the taper's surface. However, some tests performed at 48% concentration showed that the 1 hour the etching process took was not enough for the two liquids to completely mix and the final surfaces presented a smoother surface. Notwithstanding this concentration results in larger taper angles, which we were not interested in, and so we abandoned the use of ultrasounds.

Having excluded the ultrasounds we kept on working with the other 3 alterations we had just made, inside a clean room, on isolated cuvettes and with a larger amount of oil. The process seemed to be 1 or 2 minutes slower than it was outside the cleanroom. When the tapers were removed at exactly 2 hours of etching they usually came with a very thin fibre tail at the tip - see figure 4.8 (first one on the left) - the extra minute or so was usually enough to guarantee this did not happen. However, we started to look

at it as a possibility to obtain an apex as small as desired and so some tailed tapers were intentionally produced. Comments on such tapers will be made in the next sections.

The fact is this seemed to have done the trick, we had finally found the parameters that guaranteed us the tapers we desired - 2.5 mL of HF 30% and 500 μL of paraffin oil in a cleanroom controlled environment with one fibre per cuvette. Of course, is not a perfect method, and some tapers still have significant defects, but the frequency with which this happens was reduced throughout the optimization process.

To close this section there is still one important thing to mention. The orientation in which the fibre is placed inside the cuvette is also a very important, and sometimes difficult to control, factor that influences the taper's shape. A closer look at the tapers of figure 4.8, shows that some of those tapers present a slight asymmetry, as if the etching process started at different fibre heights on each side. This can happen when the fibre is not placed at a perfect 90º angle with the acid surface, which is a frequent event. As the fibre is commercialized in rolls, when we cut a short piece to fabricate a tweezer that we can latter splice to our setup, it is already slightly curved. This gentle curvature is hard to correct and so the 90º are hard to attain. If the asymmetry of the taper is very significant we may have to discard it as an optical tweezer, as this means that the fibre's core is not at the tip, but displaced to one of the sides, affecting the light delivery to the exterior.

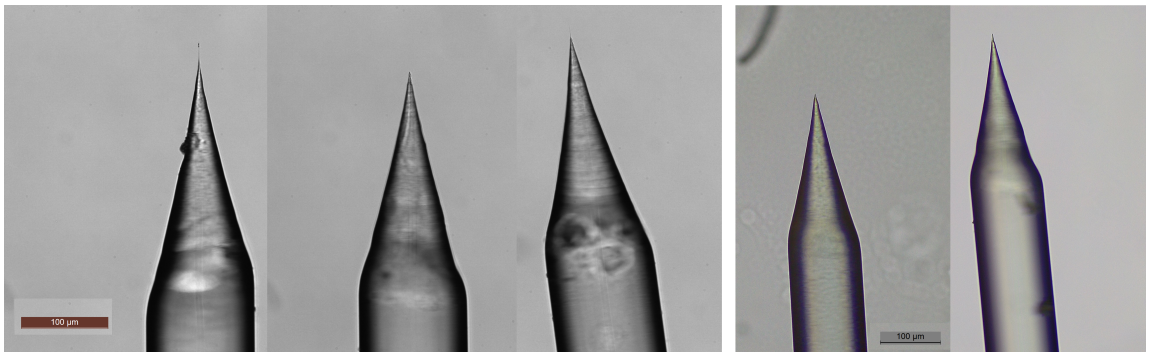
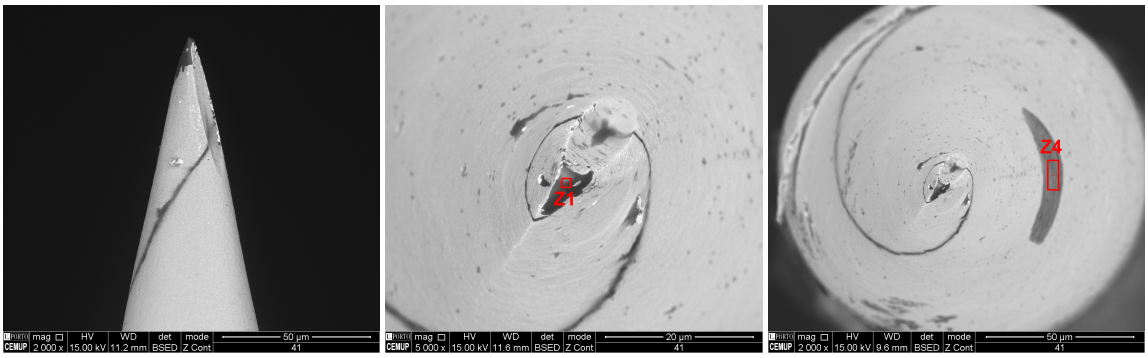


FIGURE 4.8: Tapers fabricated with the optimized etching process. The first one to the left presents a little fibre tail.

4.1.2 The gold coating

The overall description of the coating procedure has already been presented in chapter 2, here we mainly want to stress out some of the difficulties encountered during the process and the main results obtained.

Since we were depositing on a cylindrical surface and the film thickness monitor is calibrated for planar depositions, the thickness value the monitor shows us does not match what is deposited on the fibre's surface. Fortunately, there were registered values from previous works that showed that for every 225 nm deposited on a planar substrate, 100 nm were deposited on the fibre.

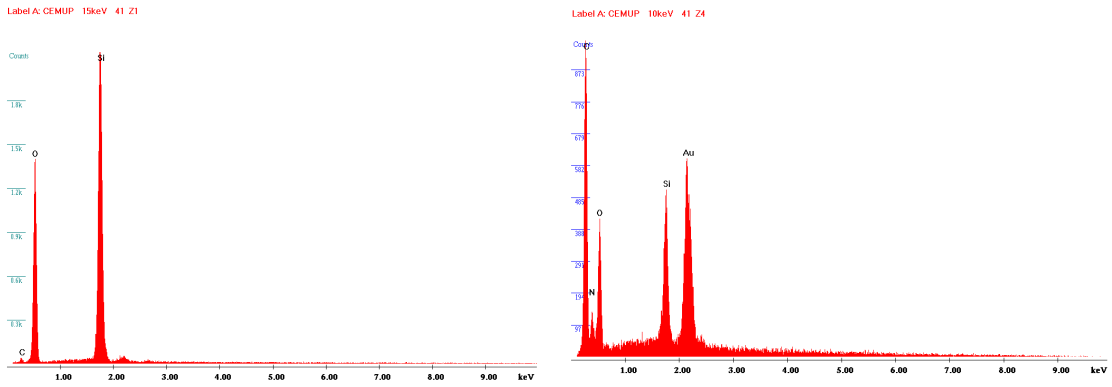


(A) (B) (C)

FIGURE 4.9: SEM images of gold coated taper labeled as number 41: lateral (A) and top (B) (C) views. Zones 1 (B) and 4 (C) are identified in red.

For the first depositions, we choose a few tapers with defects. We had no idea of how it was going to go and we did not want to compromise the good ones. Four tapers were assembled at the e-beam as previously described and the pressure value of $10^{-6} Torr$ was achieved without a problem. We deposited a 2 nm layer of Cr, followed by what was supposed to be a 100 nm deposition of Au. Due to an e-beam's source problem, the deposition stopped at 55.11 nm. Both depositions were performed at a rate of $0.1 nm/s$. Given that at the time we were not sure of what had caused the problem, we repeated the deposition test that same day, with a set of 4 other tapers. The 2 nm of Cr were deposited without any problem, but the Au deposition was again abruptly interrupted when it reached a thickness of around 52.66 nm.

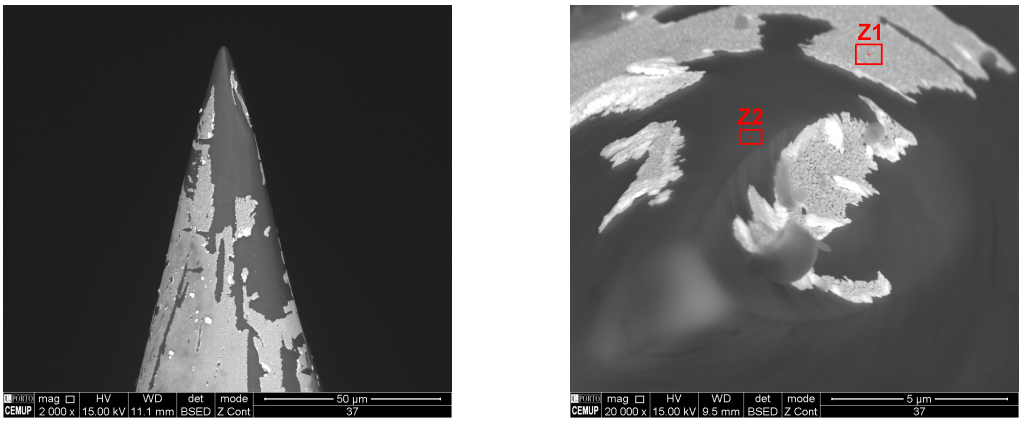
The SEM images collected at CEMUP and presented in figures 4.9 and 4.11 show two of the tapers resulting from the depositions described above. These were acquired a couple of weeks after the Au layer deposition, during which time they were dipped in water and solutions containing polystyrene particles of various sizes. The gold layer, seen in light grey in the figures, presents a smooth surface, a good indicator of deposition quality. However, there are some areas where the gold has either not been deposited or was somehow removed during the period in which they were being tested. Energy dispersive



(A) (B)

FIGURE 4.10: EDS results for zones 1 (A) and 4 (B) of taper 41.

spectroscopy (EDS) was used during the SEM session to study the darker areas and confirm that they are in fact Si, from the fibre's surface - figures 4.10 and 4.12. For the case of the darker zones - zone 1 in figure 4.9 (B) and zone 2 in figure 4.11 (B) - a large peak appears in the EDS spectrum around 1.8 keV, indicating the presence of Si and no Au. As for the light grey areas, although they still indicate the presence of Si, because the beam penetrates through the surface, there is clear evidence of the presence of gold (peak is just above 2 keV). The presence of other elements such as O and N indicate the contamination that probably happened during the time they were tested.

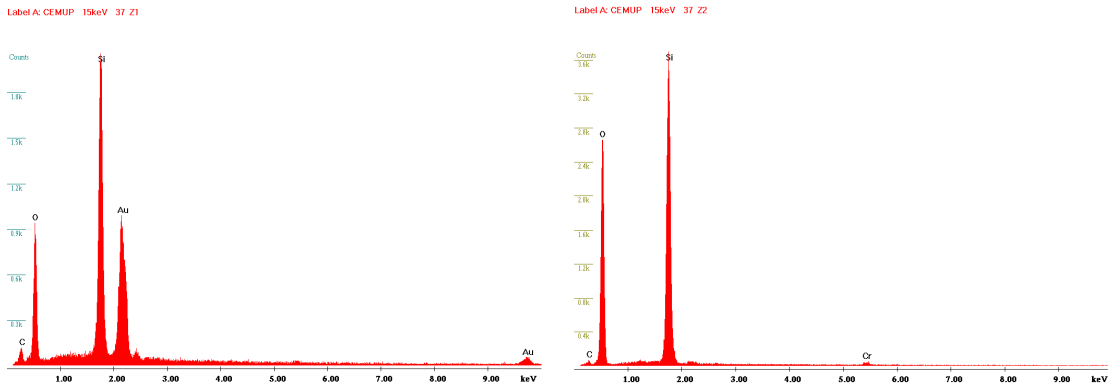


(A) (B)

FIGURE 4.11: SEM images of gold coated taper labeled as number 41: lateral (A) and top (B) views. Zones 1 and 2 are identified in red (B).

But why exactly has the gold been stripped of the surface of the fibre? Could it be that the deposition did not uniformly distribute the gold near the apex, or could it have been a consequence of their utilization during tests? The fact that the fibre was coupled to the setup and light had been guided through it all the way to the apex could affect the gold

layer if the power is too high. Either way, we were not going to be able to answer this question just by looking at these tapers, new ones were needed.



(A) (B)

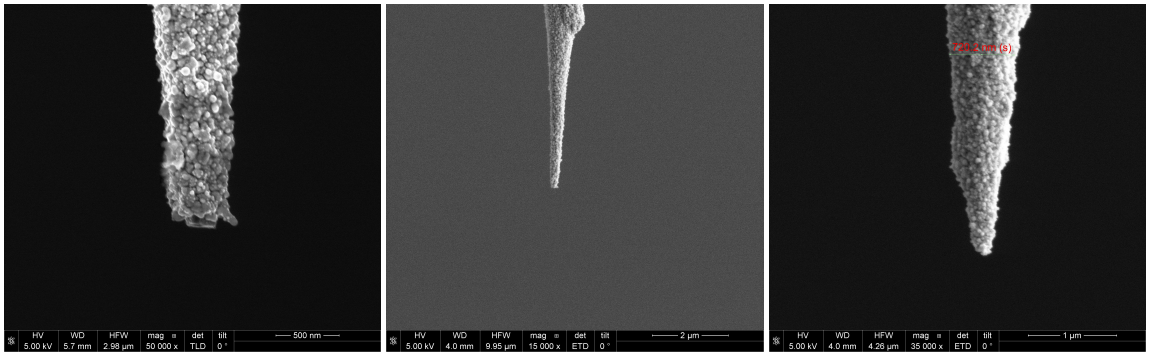
FIGURE 4.12: EDS results for zones 1 (A) and 2 (B) of taper 37.

Once the problem with the power source of the e-beam had been fixed we got back to the cleanroom to do some more depositions in a new set of tapers, 6 of them to be precise. Only this time the problem was not with the power source, but with the vacuum pump. Pressure levels would not go below 3.5×10^{-5} mbar, which is considered a high-pressure value for deposition. As we were not sure of if and when the problem would be fixed, we decided to go through with the deposition, even with that pressure. Once again we began by the layer of Cr, 3.18 nm were deposited with a pressure of 6×10^{-5} mbar inside the chamber. As for the layer of Au, the deposition was carried with a pressure value of 8×10^{-5} mbar inside the chamber and the layer reached a thickness of 100 nm. However, a problem with the equipment resulted in a very sudden and strong light and the thickness measured by the monitor rapidly rose from 218 nm to 231.9 nm, right before we turned it off.

Some of the results of this deposition can be seen in figure 4.13. These tapers were not tested before this images were acquired and the Au layer appears to have endured the time, meaning that the problem we had found before was not a deposition associated one. The stripping of the gold probably resulted from the performed tests and the small thickness of the layer.

This set of tapers presents, however, a very rough surface when compared to the others. Most likely the roughness is a consequence of a vacuum level at which the deposition was performed. As the number of particles present in the chamber was still above what was supposed to be, it may have interfered with the process. But also, that final event

described above that we could not understand, could have been an abrupt gold release directed at the fibres.



(A) (B) (C)

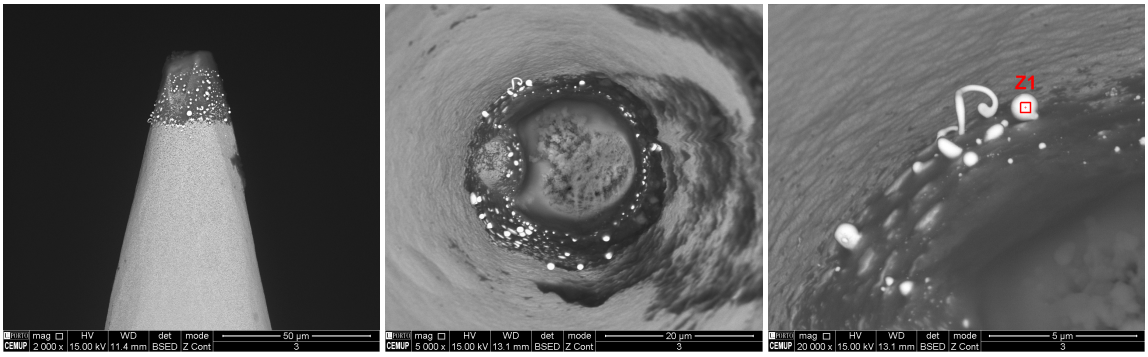
FIGURE 4.13: SEM images of gold coated taper labeled as number (A) 1, (B) 4 and (C) 5. Images acquired at the Iberian Nanotechnology Laboratory (INL), Braga.

After these tapers were coated, the e-beam evaporator was inoperational for a couple of months, preventing further depositions to occur within the time limits. As a consequence we had to work with the tapers we had, since the exterior surface roughness should have no impact on the tweezer performance.

4.1.3 Aperture milling

One thing that we concluded from the metal coating depositions was that they did not leave an aperture at the apex, there was no shadow area being created and as such we needed another technique to fabricate the aperture.

A femtosecond laser (SATSUMA HP^2) was our second attempt. We tried using it to perform a transversal cut on the taper's apex, in order to open an aperture much like the one represented in figure 1.16 (A). As it was just preliminary test and the image resolution of the femtosecond direct writing laser system was not adapted to the sub-micrometre dimensions of the tapers apex, the cuts were performed in a region of the taper where the diameter had already a few micrometres. The fibre was then placed in a glass slide with the tapered part just a few millimetres outside it, so the beam would not affect the slide. The sample was then mounted onto the femtosecond system setup and the beam was swept across a range of a few micrometres so that one of the pulses would hit the tip. However, sometimes a single pulse was not enough to cut through the entire thickness of the structure and the process had to be repeated. The results can be observed in figure 4.14.



(A) (B) (C)

FIGURE 4.14: SEM images of a femtosecond laser beam cut to a taper: (A) lateral view (B) top view (C) zoom in top view with EDS tested zone identified.

The femtosecond laser was, in fact, successful in cutting off the apex of the taper, however, it was also responsible for a peel-off of the gold layer that previously coated the entire taper. Without it, light is no longer confined to the interior of the core and no field enhancement effect can happen. This was probably originated by a thermal effect, as the gold appears to have coalesced into tiny spheres - white spheres in figures 4.14 (B) and (C). Initially, we were not sure if those were gold or polystyrene particles, but after an EDS analysis their composition was confirmed by the Au peak in figure 4.15 (A).

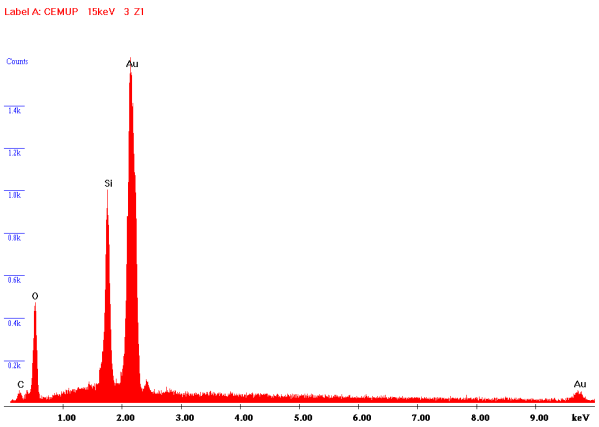
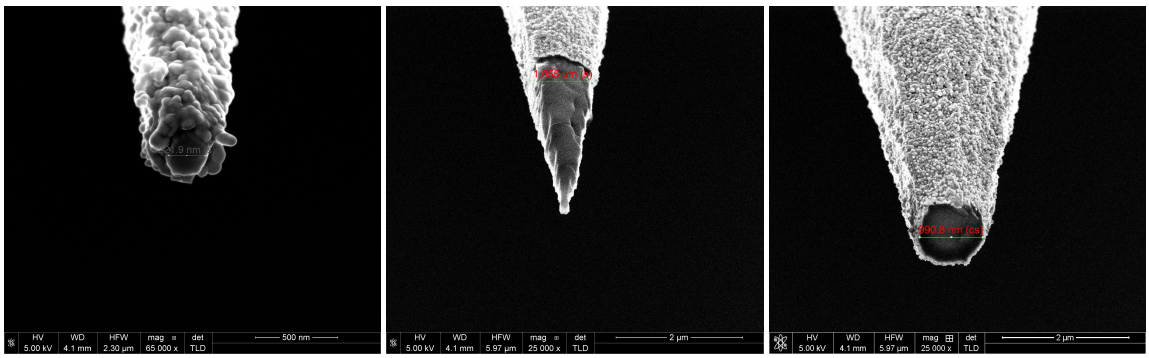


FIGURE 4.15: EDS spectrum of zone 1 identified in figure 4.14 (C).

Besides removing the gold layer close to the apex, this technique also results in a very rough apex surface, as can be observed in figure 4.15 (B). So even if the gold was still in the surrounding surface, the field output would also be affected by this roughness.

We came to the realization that the only technique that would guarantee the results we needed was the FIB milling. The sample preparation and assembly as already been described in chapter 2, now we will present and comment on the results.

We will focus the comments in the representative taper that can be seen in figure 4.16 in three different stages. When we first assembled the taper into the machine we examined it with the electron beam, to acquire an image without damaging the sample - in figure 4.16 (A), the taper as assembled, prior to any cut. The second step is to try to make the two beams coincide in a point so that we know exactly where we are milling. This, of course, requires the use of the ion beam. However, the ion beam damages the gold surface, so care must be taken when working with it. Initially, we were using a current of 7.7 pA in a continuous acquisition mode. To the reader, this may seem negligible, but it was enough to induce the damage seen in figure 4.16 (B). At first, we were not aware of what was happening, as we were trying to focus the image using ions, but then after careful analysis, we understood that the ion beam, even at such a low current had already done significant damage to the layer of gold. As decreasing the current would harden the task of focusing, we instead switched to snapshot acquisition. The current was still the same, but the beam was only hitting the sample a few times.



(A) (B) (C)

FIGURE 4.16: SEM images of FIB milling results: (A) taper as assembled to SEM-FIB machine, (B) damage induced to the gold layer by the ion beam, and (C) taper's aperture resulting from a FIB cut. These images all belong to the same taper.

Although the induced damage had already made us lose the narrower part of the taper, we decided to cut it either way and we still managed to get an aperture of 990.8 nm - figure 4.16 (C). The current used for this cut was 80 pA, although a smaller value like 24 pA would have been sufficient as we latter verified.

All of the milling was done transversally to the fibre's axis because of stub limitations. Given the existent angle between the ion and electron beams, in order to perform the milling exactly at the top of the axis, a specific inclined stub would have been necessary. Such stub was not available at INL at the time.

With this process we were able to produce 5 fully developed tweezers that will be presented and characterize during the next sections.

4.2 Tweezers characterization

The final tweezers with apertures ranging from 580 nm to 1700 nm are presented in figure 4.17 and table 4.2 presents their geometric features. In this section, some experimental and simulational results are presented and analysed to help better understand the transmission and collection properties of each taper. With these results in hand, the analysis of the trapping events will hopefully be facilitated.

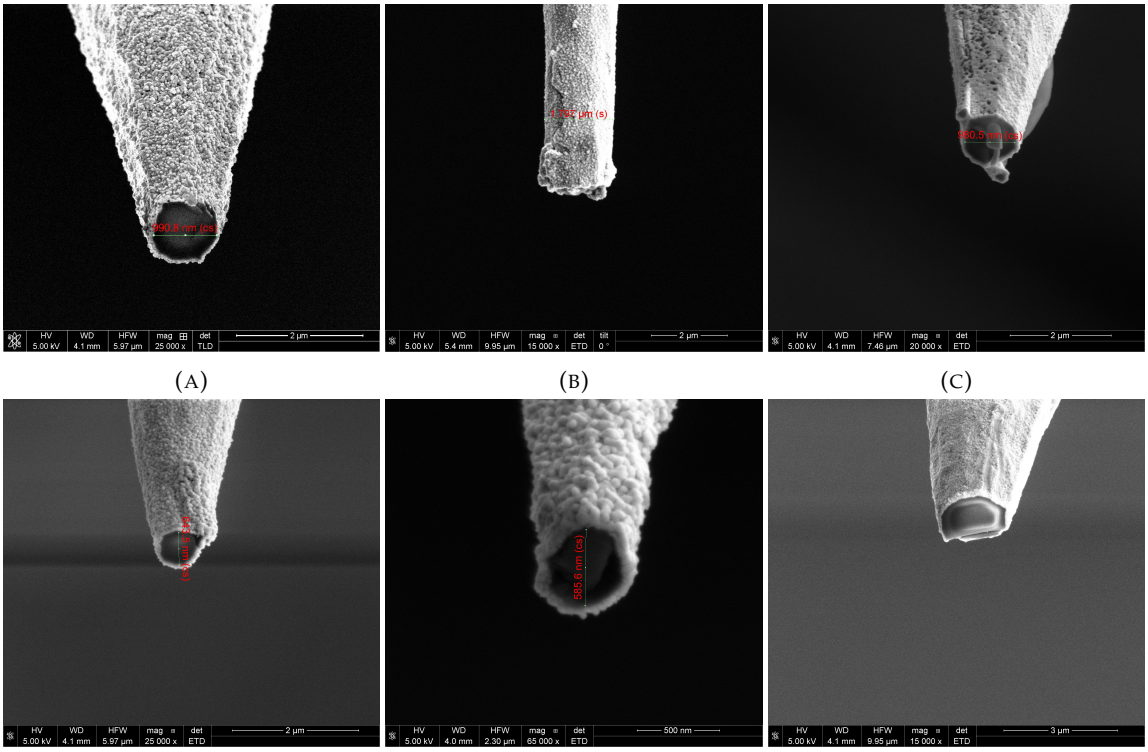


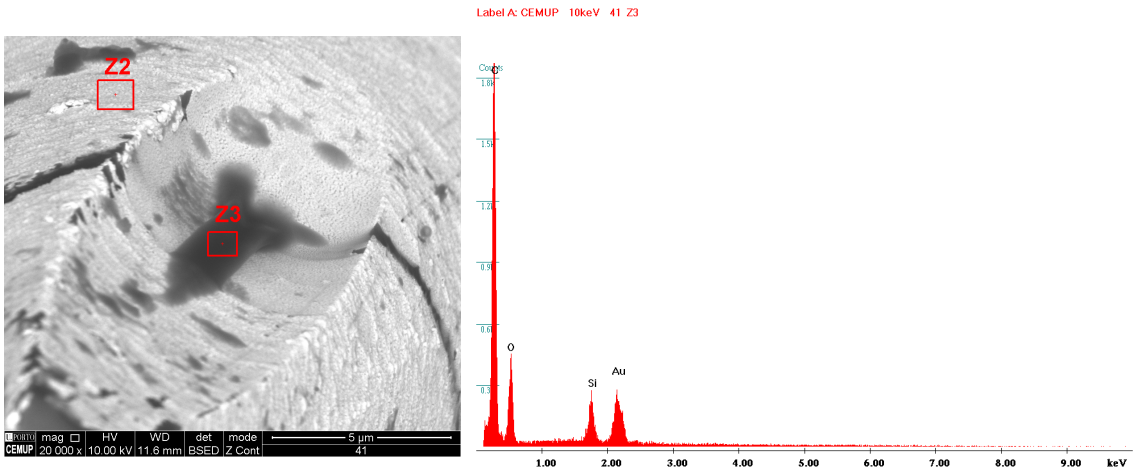
FIGURE 4.17: SEM images of the tweezers used in the optical trapping tests: (A) tweezer 1, (B) tweezer 2, (C) tweezer3, (D) tweezer 4, (E) tweezer 5 and (F) tweezer 6. The tweezer number 2 broke during the milling process and was not used for testing.

Initially we wished to evaluate the transmission properties of these tweezers, however, as we are dealing with optical near fields, it is difficult to evaluate them experimentally. Nonetheless, in a preliminary test with one of the first gold-coated tapers, we decided to experiment with a photopolymerization process to check whether or not an aperture had formed and if that was the case, what would the field look like. We have previously investigated the possibility to obtain an aperture in the gold coating, by playing with the

asymmetry of the coating process. We were hoping that in the right position, a part of the tip could be shadowed preventing deposition. In practice, this was not observed. However, in one of the tapers, the core and the apex were dislocated from each other, resulting in a hole near the apex - see figure 4.9. This surface accident ended up forming a shadowed area where no gold was deposited. This way, when the fibre was dipped in a liquid polymer and latter illuminated from within, the polymer exposed to the light solidified - figure 4.18 (A). This was an interesting result because, in these conditions, the polymer typically assumes the shape of the propagating mode at the output. Indeed, in this case the polymer presents a very similar shape to the expected field profile in the simulations. EDS was used to confirm that what we were seeing was, in fact, the polymer, and not other surface feature. The presence of the C peak confirmed that it was the polymer - figure 4.18 (A).

Tweezer	Cone angle (º)	Aperture Diametre
1	27.35	990.8 nm
3	25	980 nm
4	26	643 nm
5	15	585 nm
6	20	1700 nm

TABLE 4.2: Tweezer's geometric features.



(A) (B)

FIGURE 4.18: (A) SEM image of the field shape imprinted on the polymer. (B) EDS results of zone 3 identified in (A).

4.2.1 Some observations on transmission

As was pointed out in chapter 1, the presence of a particle near the aperture can be detected by small alterations in transmitted and reflected intensities. It has been reported that the tweezers become more sensitive to these variations when the wavelength of the radiation that crosses the aperture is above the resonance.

To investigate into the resonance of each aperture and understand if it will influence the sensitivity latter on, three of the six tweezers (1, 4 and 5), the more promising ones, were simulated in COMSOL Multiphysics and a study of electric field intensity as a function of wavelength was conducted. The results can be seen in 4.19. It is important to stress out that the tweezers not only differ from each other in aperture diameter, but also in the cone angle of the taper. These geometrical differences make it difficult to draw conclusions from the results because there are two geometrical parameters varying at the same time, there is no way to tell which parameter is responsible for a certain variation.

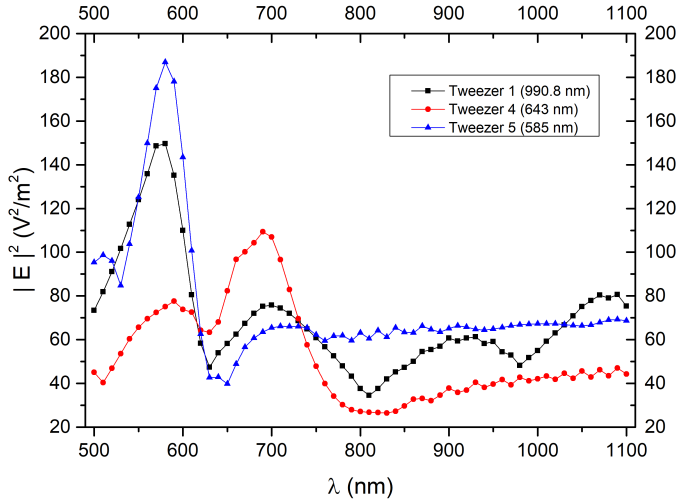


FIGURE 4.19: Tweezers maximum intensity outputs as a function of wavelength. Tweezer 1 has an aperture diameter of 990.8 nm and a cone angle of 27.35º. Tweezer 4 has an aperture diameter of 643 nm and a cone angle of 26º. Tweezer 5 has an aperture diameter of 585 nm and a cone angle of 15º.

Tweezers 1 and 5 present a pronounced peak for wavelengths in between 550 nm and 600 nm followed by a second peak around 700 nm. Afterwards, they seem to present regular intensity variations with wavelength that relates to the different combination of propagating modes that occur for each wavelength. Tweezer 4 presents a very similar behaviour, however, the second peak is the highest in this case. In order to draw some conclusions as to what factor is responsible for these variations other sets of tweezers had to be modulated where only one parameter is changed, be it the cone angle or the

aperture diameter of the taper. In the present case, we will only use these results to better understand the signals acquired during the trapping tests presented ahead.

Overall two thing can be concluded from this data. One, they all present a resonant behaviour for wavelengths bellow the value we will be using and two, for that wavelength, 980 nm, we expect tweezer number 5 to present better transmission, followed by tweezer 1 and tweezer 4.

4.2.2 Backscattering collection

One of the first experimental studies conducted relates to the collection of backscattered radiation. Since as a future project we wish to apply these tweezers to the identification of single cells through a backscatter analysis algorithm, we first needed to assure ourselves that that would be possible. It is important to stress out that all the results presented in this section were acquired without having a particle trapped in the optical potential.

Not only did we wanted to see if the collected energy was significant enough to allow a posterior analysis, we also wanted to verify if the angle at which the tweezer is incident on the solution, i.e. the angle the tweezer makes with the surface where the drop of solution lays, somehow affects the outcome of the experiment. We pose this question mainly because of the role this angle parameter has been shown to play in the optical trapping efficiency for polymeric tweezers. From previous works, we know that it is not possible to obtain stable trapping for an angle lower than 30º [15]. To find the answer to this question we conducted an experiment using a single tweezer with an aperture of $\approx 1.7\mu m$. The tweezer was dipped into two different environments, one contained only deionized water and a second one containing a deionized water solution of polystyrene particles of $1\mu m$ average diameter. For each environment, the tweezer's angle of incidence was varied from 35º to 60º and for each angle, a set of 7 backscattered signals of 60s were acquired. The results are depicted in the graphic from figure 4.20.

An overall look leads us to conclude that there is no significant changes in the average power values acquired with the angular change. All the values are in close proximity to the blue line that represents the medium energy value acquired, or at least their deviations are. Also, the separation between the values obtained for the DI water and the polystyrene solution is very small, even being coincident in some cases. This is easily explained by the

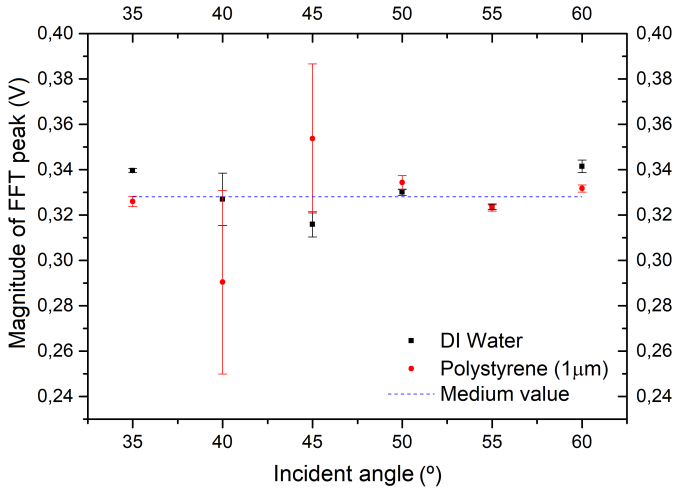


FIGURE 4.20: Peak value of the FFT of the collected backscatter signal as a function of tweezer's angle of incidence in the solution. The peak value is an indicator of the amount of energy collected at that frequency (1kHz).

equivalence in refractive indexes between the two media. As the polystyrene concentration present in the solution is so low, it is not enough to change the DI water's refractive index. In both environments, the measured refractive index was of 1.3324 ± 0.0001. The fact that the angle of incidence of the taper does not play a major roll here is due to the fact that even though the light that reaches the particle is being scattered in all directions, not all directions are receiving an equal amount of light. The most likely scenario is a direct incidence of photons in the particles that bounce straight back to the tweezer [93]. This way, considering the configuration used for backscatter collection, as much as we vary the angle in which the tweezer is incident on the solution, the angle between the incident and collected radiation is always the same - 180º.

To finalize, the larger deviation for the angles of 40º and 45º, that only appears for the case of the polystyrene solution, may suggest a larger sensitivity to environmental variations, such as the passage of a polystyrene particle near the tweezer. Either one of these angles seems to indicate good sensitivity for optical trapping tests, for experimental convenience we opted to start for the 45º. Choosing the ideal experimental conditions for this project is of the utmost importance, because given the tweezers fragility, they may suffer damages throughout the testing process.

4.3 Optical trapping

Throughout the remaining of this chapter, the optical trapping results will be presented. It begins with a description of the experimental setup used for the optical trapping tests and a brief description of the initial tests, trying to understand why those did not work. A presentation of the stable trapping results follows with the respective trapping forces analysis.

4.3.1 Optical trapping and signal acquisition setup

The experimental setup used to trap and manipulate the particles consists of an inverted homemade microscope with a 60x objective, where a CMOS camera is used to acquire images of the trapping - see figure 4.21. The fibre that contains the tapered tweezer is controlled using a motorized micro-manipulator capable of handling the optical fibre in the x, y and z-direction, and varying the inclination angle. Since the fibre is too fragile to be handled directly by the micro-manipulator, it was first inserted in a capillary, and only then placed on the controller.

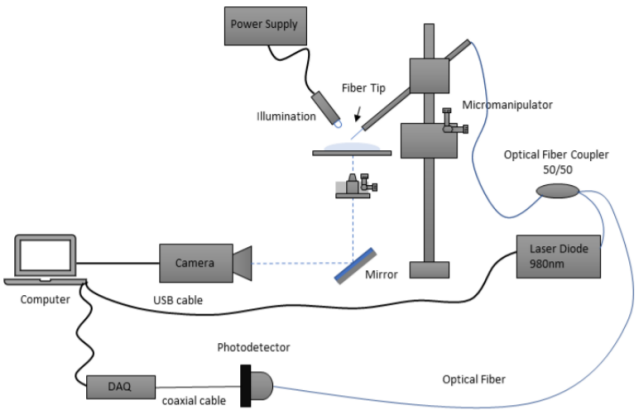


FIGURE 4.21: Experimental setup used in the optical trapping and back-scattering signal acquisition experiments.

The tapered fibre tweezer was connected through the exit port of a 1x2 (50:50) optical coupler to a pigtail 980 nm laser diode (cLDD MWTECH) and the signal acquisition module. The latter included a photodetector to collect the back-scattered signal and a data acquisition board (DAQ) from National Instruments for signal processing. A computer-controlled both the DAQ and the laser enabling control of its input and output parameters. This configuration allowed both laser light guidance through the optical fibre, and the acquisition of the back-scattered signal through the photodetector.

The laser diode 980 nm signal was modulated by a sinusoidal signal with a frequency of 1 kHz, to the noise from the power grid. This signal was injected in the laser module using the DAQ, and was acquired with a sampling rate of 100kHz.

4.3.2 Preliminary experiments

4.3.2.1 Checking for thermal effects

In a preliminary approach to all tests, we needed to be sure that the optical power used to trap the particles would not induce any thermal effects, or if it did, we wanted to be aware of it. As it was described in the introductory chapter of this thesis, thermal effects may, on their own, induce movement on the particle, affecting the effects of optical trapping forces. Furthermore, they could induce damage to the gold layer coating the tapered fibre, compromising future tests.

With this in mind, prior to the trapping experiments, the tweezers were tested for thermal effects. To do so, they were dipped inside a solution containing polystyrene particles with an average diameter of $1\mu m$ and the laser was turned one at its lower current value above threshold: 30 mA, which corresponds to a power of about 0.117 mW - see appendix A. The experiment was monitored through the CMOS camera, to evaluate whether or not it induced changes in the solution, i.e. particle's behaviour alterations, or in the tweezer itself.

Our main focus was to look for alterations in the particle's Brownian motion once the laser was turned on. Several videos were acquired, first with the laser off and then on, so a safe comparison could be performed. No increase in vibrations due to Brownian effects was noticed with the laser at 30 mA, so we increased the current to 40 mA. Again, no change was verified. When the current was once again increased to 50 mA and the tweezer was brought close enough to a particle, a trapping event was verified and still no changes in the Brownian motion of the solution were observed. We had thus achieved the minimum necessary power for trapping to occur - 50 mA corresponding to 1.327 mW - for which no thermal motion appeared to be induced.

We decided to further increase the laser current to 100 mA, which corresponds to $\approx$ 4.23 mW. We did so because it allowed us to achieve a more stable trapping position. The majority of trapping and backscatter radiation collection was performed with these laser parameters.

Posterior analysis of the tweezer in an optical microscope showed no alteration in the gold layer. Of course, we could only affirm it with certainty with a SEM analysis, however, as a consequence of the destruction of the tweezers during the optical trapping experiments, no further observations could be conducted. Nonetheless, as no significant alteration in trapping behaviour was noticed during their functioning period, it is likely that if it existed, the damage was neglectable.

4.3.2.2 No trapping with large apertures - the dominance of the scattering force

As could be seen in figure 4.17 (F), one of the tweezers had an aperture with a diameter significantly above $1\mu m$, $\approx 1.7\mu m$, to be specific. Given the fragility of the tweezers and our inexperience in dealing with them, we began our experiments with this more robust one. Besides allowing us to grow more acquainted with the handling of this type of tweezers, it also confirmed some of the simulation predictions in what optical trapping is concerned.

In chapter 3, we had observed that for larger aperture diameters (above 800 nm), trapping of 500 nm particles could no longer occur. So, when we initiated the experiments with tweezer 6 and polystyrene particles of $1\mu m$ in diameter, we were not expecting traping to occur. In fact, it did not. Instead, we observed the pulling away of the particle once the laser was turned on with a current of 100 mA. If we look closely at the sequence of images presented in 4.22, we can see that not only was the particle drawn away from the tweezer in the focus plane (xy plane), it also starts to look smaller and smaller, indicating a displacement in the z-axis.

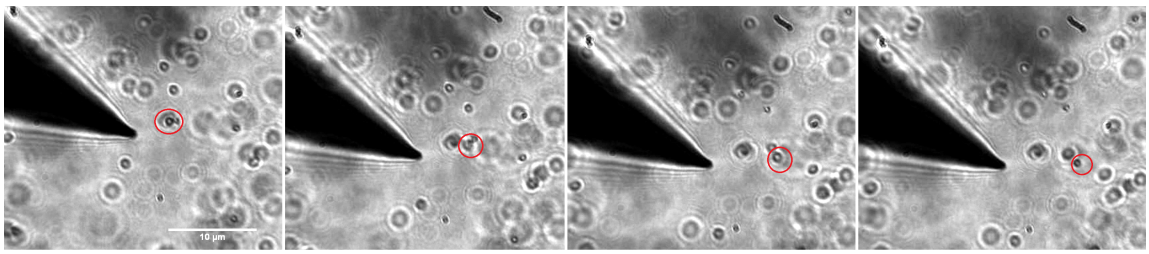


FIGURE 4.22: Sequence of images showing the displacement of a particle of polystyrene with a diametre of $1\mu m$ being pulled away from the tweezer.

To completely verify the trapping possibilities for this tweezer we performed tests on larger particles, having average diameters of $4\mu m$ and $5.2\mu m$. We again observed a pulling of the particle, only this time was slower and in-plane. The displacement is shown in figure 4.23 for a particle of $5.2\mu m$ in diameter.

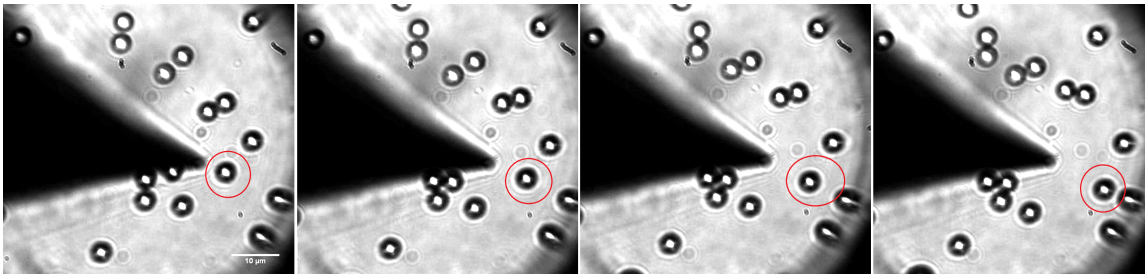


FIGURE 4.23: Sequence of images showing the displacement of a particle of polystyrene with a diametre of 5.2μm being pulled away from the tweezer.

The fact that particles with diametres well above light wavelength could not be trapped, intrigued us, in face of the previous experience with polymeric tweezers. As such, the tweezer was simulated in COMSOL, so we could better understand its output field profile. The result is presented in figure 4.24, and the answer to our question turned out to be quite simple. Even though we found a maximum gradient value in the same order of those found for the polymeric tips simulations, in the present case we have a divergent field, and not a focused one, as it happens in the lens like tweezers. As a result, the scattering force, responsible for pulling the particle away, is always dominant over the gradient component, hence the observed effects.

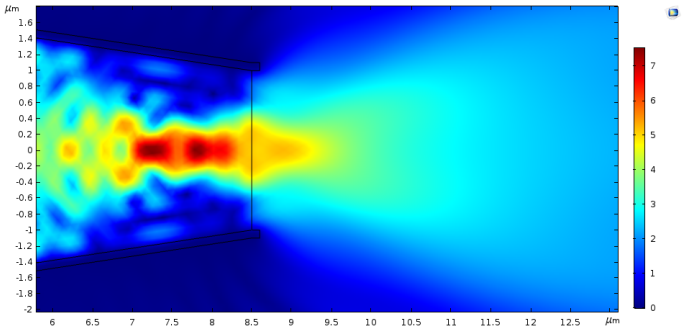


FIGURE 4.24: Output optical field of tweezer 6.

4.3.3 Optical trapping of polystyrene beads

Optical trapping with this set of tweezers was, as predicted by simulations, obtained when we experimented with tweezers having smaller apertures. We experimented with polystyrene particles with diameters of 500 nm and 1μm. Unfortunately, all of the tweezers available were damaged before we could ever experiment with smaller particles, i.e. 100 nm, as we had initially planned in chapter 3. We hope to be able to perform such tests in the near future.

Using the setup already presented in figure 4.21, tweezer 1, which has a diameter of 990.8 nm, was dipped in a solution of $1\mu m$ polystyrene particles at an angle of 45º with the planar surface. Since we were using a x60 objective, this particles could still be perfectly discernible with the camera and videos of the optical trapping of $1\mu m$ polystyrene particles were acquired - see figure 4.25 for a sequence of images.

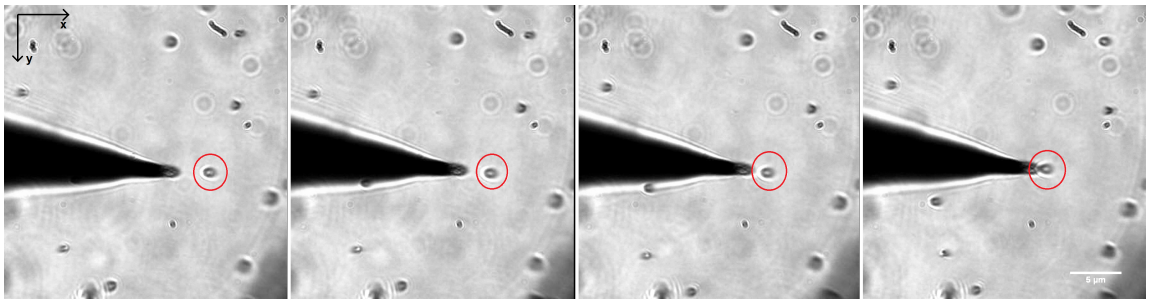


FIGURE 4.25: Sequence of images of the optical trapping of a $1\mu m$ polystyrene bead using tweezer 1.

Although visual confirmation of the trapping event is very important in the early stage of this work, we also want to make sure that other monitoring techniques are just as effective in identifying such event. For when the time comes to experiment with much smaller particles, we will no longer be able to observe them. As the setup is already equipped with a backscatter radiation acquisition segment, we used it to collect the signal during these experiments.

We hopped to observe a variation in signal level, that would be an indicator of the presence of the particle in the trap position. Since the scattering intensity is directly proportional to the difference between particle's and medium's refractive indexes, once the particle is in the trapping position, an increase in the overall refractive index observed by the tweezer will occur and thereby we expect to observe an increase in the collected signal.

We were able to confirm this experimentally. Analysing figure 4.26, we can clearly distinguish between the three different levels the signal presents. The red line shows the level corresponding to the moments the laser was off. Once it was turned on, there was an abrupt rise to the green level, where it remained until some particle was caught in the trapping position - the dark blue level. This signal level also displays larger signal fluctuations, that correspond to the random motion of the particle due to the thermal excitation of the trapping potential. It is worth pointing out the existence of a higher level in between 40s and 45s, that is not signalled in the plot. This corresponds to the presence

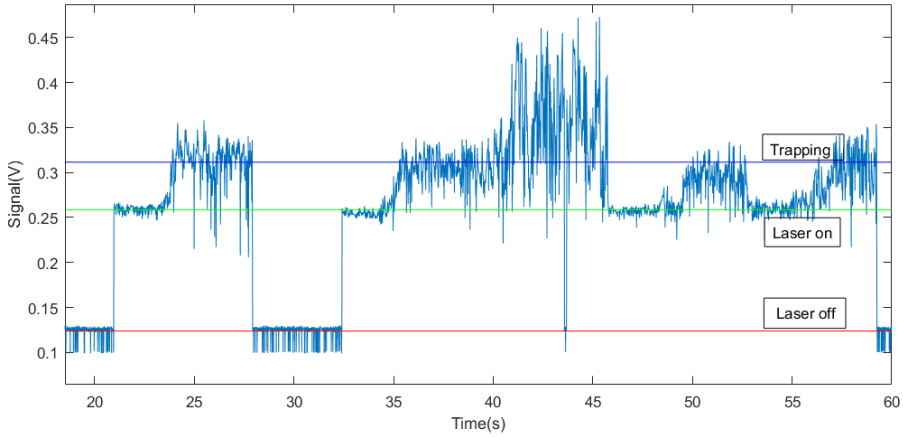


FIGURE 4.26: Signal collected during the optical trapping of a $1\mu m$ polystyrene bead. Three different signal levels are identified - laser off in red, laser on in green and trapping of a single bead in dark blue. The signal shows an aditional increase between 40s and 45s that corresponds to the presence of more than one bead in front of the aperture.

of more than one bead in the trapping position. In fact, thanks to image collection we can see that a cluster of 3 beads was present at that time - figure 4.27.

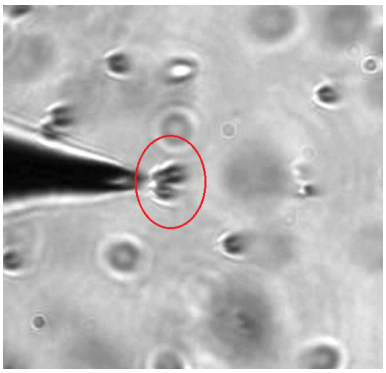


FIGURE 4.27: Cluster of particles in front of the tweezer.

Afterwards, we switched to 500 nm polystyrene particles. The differences were many. First of all, we could no longer see the particles with a good resolution. We were able to distinguish them in the image, but it was harder to focus and discern their edges. This hardened the task of finding a focus plane for both the particles and the tweezer simultaneously. More so, given the decrease in the particle's dimension, an increase in Brownian motion was visible in comparison to the larger particles.

We had, however, seen in chapter 3 that a tweezer with an aperture above 800 nm would not be able to guarantee the optical trapping of 500 nm particles. This was experimentally verified. No trapping occurred for these particles, with this tweezer.

Switching to smaller tweezers some broke even before we could verify if they could, or not, be used for trapping. Due to lack of experience handling such fragile devices, at first some tweezers broke while being assembled, others during tests. Given their small dimensions, sometimes it was hard to understand whether or not it was dipped enough into the solution to get a clear image. A wrong evaluation of that depth could result in diving the tweezer too far until it hit the surface of the glass slide, which happened once.

Finally, with tweezer 5 we obtained trapping of 500 nm polystyrene particles. However, here the focusing problem mentioned above was noticeable and finding a plane where both tweezer's tip and particle's edges were easy to discern turned out to be an impossible task. This resulted in the sequence of images presented in figure 4.28, where the particle appears blurred and not in the focus plane. This was the case for all events of trapping registered.

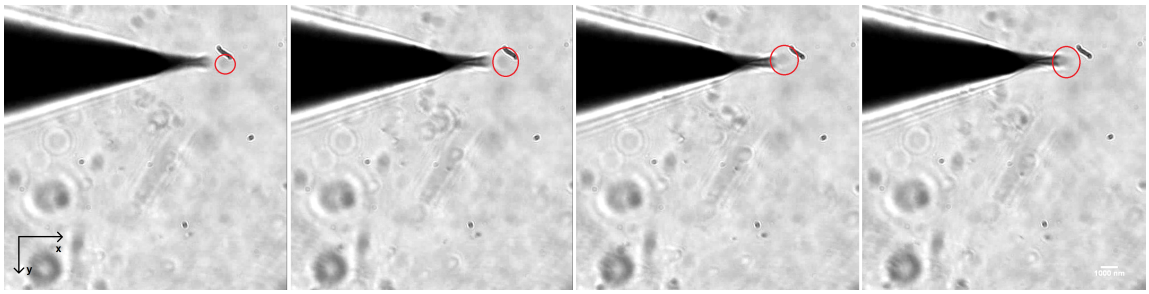


FIGURE 4.28: Sequence of images of the optical trapping of a 500 nm polystyrene bead using tweezer 5.

Although it was still possible to make use of the collected images to conclude that trapping was happening, we wanted to make sure that the same conclusion could be drawn from the collected signal, thus verifying its feasibility for 500 nm particles. In fact, we could see the signal variation again, indicating the optical trapping occurrence - see figure 4.29.

4.3.3.1 Experimental optical force measurement and stiffness determination

To provide a better quantitative analysis of the results, we wanted to determine the optical forces acting on the particles during the displacements, as well as the trapping stiffness of the optical fibre tweezer.

As described in chapter 2, we utilized the drag force method to determine the value of the force acting on the particle in each displacement. To do so, we considered that

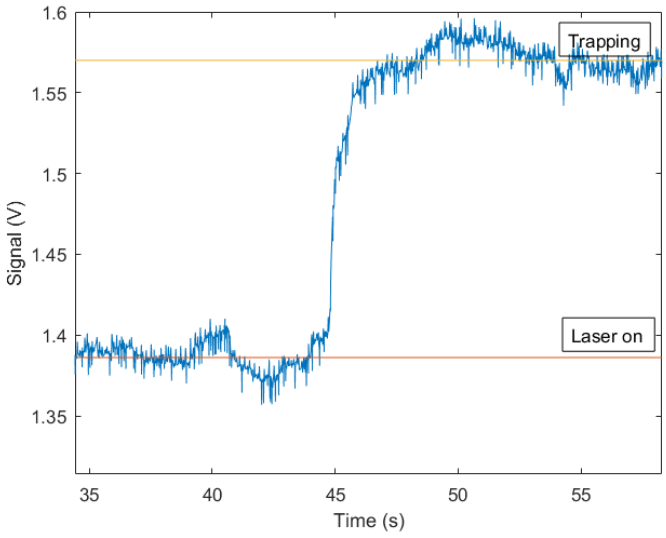


FIGURE 4.29: Signal collected during the optical trapping of a 500 nm polystyrene bead. Signal levels are identified - laser off in red and trapping of a single bead in yellows.

the centre of the particle was at a distance from the chamber equal to its diameter, hence $h = 2r$ and $\frac{r}{h} = \frac{1}{2}$. This corresponds to a correction factor of 1.386125.

Several displacement videos were collected. Initially, the laser is off and after it is turned on to 100 mA (which corresponds to $\approx 4.23mW$ entering the taper - figure 4.30), we observe the particle being attracted to the tweezer. Such displacements were recorded in three directions. These 3 directions were positive and negative $y - axis$ and negative $x - axis$. Positive $x - axis$ was not taken into consideration because, given the proximity of the trapping point to the tweezer itself (only a few nanometres), the optical resolution we have with the camera does not suffice to guarantee that the particle is not just being pulled by contact with the tip of the tweezer.

With the acquired videos, the particle's trajectory was determined and fitted to a Langevin equation - see figure 4.31 (A) - from where the velocity was calculated and then used to determine the force according to equation 2.9 - see figure 4.31 (B).

This procedure was repeated for each of the recorded displacements and in every case the form of the results is similar. Taking a closer look into figure 4.32, the reader can see a curve resulting from the analysis of two different displacements in the transversal direction: $-y$ and y. The graphic demonstrates an attractive force that results in the displacement of the polystyrene particle towards the stable position - the direction of this force is represented in red in the plot.

These measurements allowed us to calculate the force values along the axial and

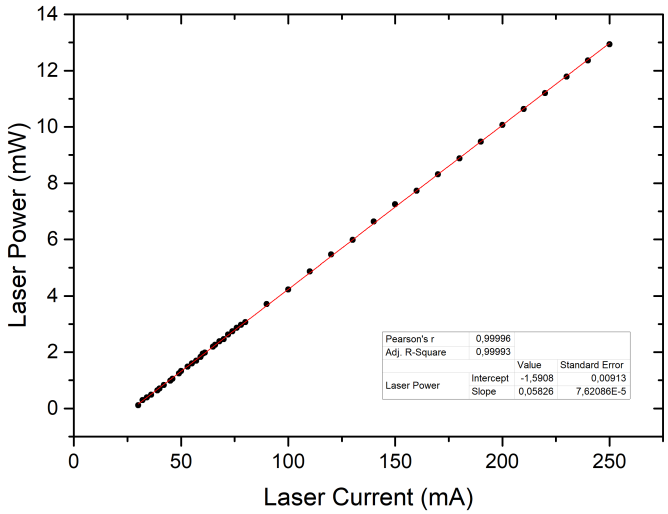
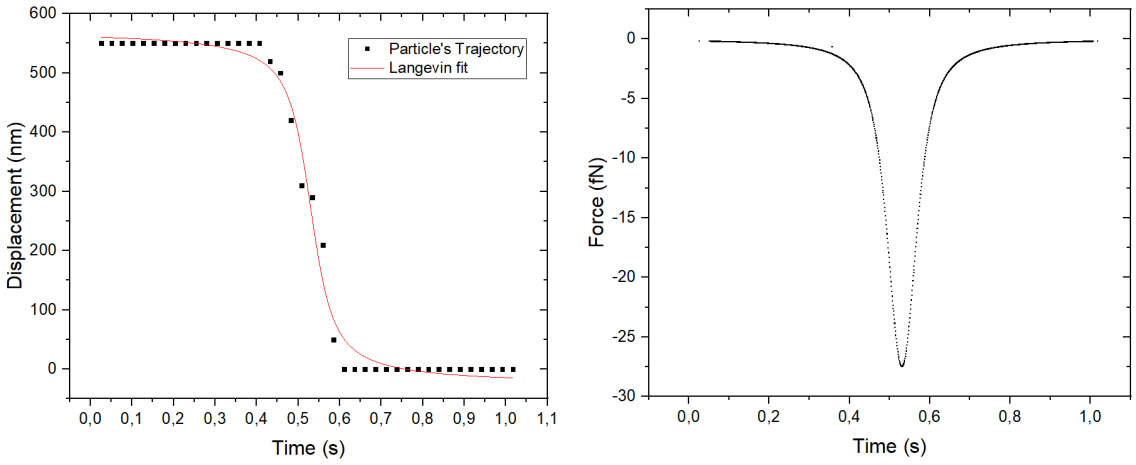


FIGURE 4.30: Laser characterization: power measured at the output of a cleaved optical fibre as a function of applied current. The black dots are the experimental data and the red line the linear fit.



(A) (B)

FIGURE 4.31: (A) Trajectory of a polystyrene particle fitted to a Langevin equation. (B) Force calculated from the data in graphic (A).

transversal directions for tweezer 1 and along the axial direction for tweezer 5. Transversal measurements were not made for tweezer 5, because the tweezer broke during the axial experiments. The results can be seen in table 4.3. They are all within the same order of magnitude, the femtoNewton (fN) range, which was expected given the information presented in chapter 1. Both tweezers present similar values of axial force, as they both have an aperture diametre close to the dimensions of the particle they were trapping. Although no observations can be made for tweezer 5 in what regards the transversal force, we can see that there is an asymmetry present in tweezer 1. Most likely this is the consequence of not having a perfectly circular aperture. As was noted earlier on in this chapter,

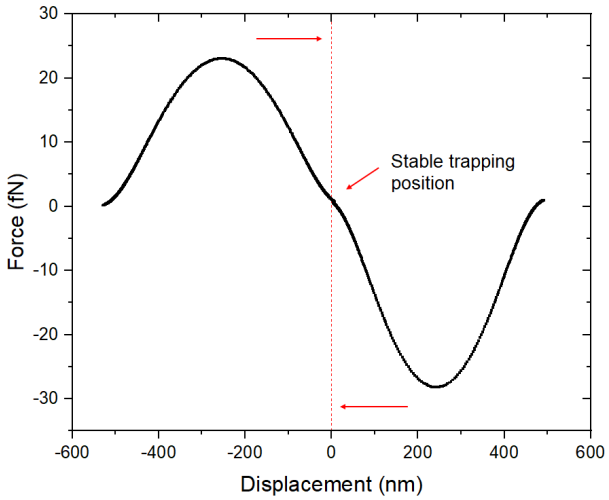


FIGURE 4.32: Optical force as a function of the displacement relative to the stable trapping position. The red dashed line represents the stable trapping position. These results were acquired fot the transversal direction (y).

the etching process does not have an ideal reproducibility, and as such the resulting taper may be asymmetric itself, thus influencing the final tweezer and the outcome of the experiment. Notwithstanding, they are both within the same order of magnitude.

Polystyrene $1\mu m$ (Tweezer 1)			Polystyrene $0.5\mu m$ (Tweezer 5)
F_{-x} (fN)	F_{-y} (fN)	F_y (fN)	F_{-x} (fN)
-21.58 ± 3.01	-51.48 ± 16.35	30.25 ± 2.04	-19.58 ± 4.04

TABLE 4.3: Experimentally measured optical forces for a power of $4.23mW$ injected into the taper. Forces were calculated using the drag force method.

As for the stiffness determination, we made use of the collected backscattered radiation and proceeded to analyse it in accordance with references [47, 94]. As was already shown in figures 4.26 and 4.29, the signal presents an abrupt transition when a particle is trapped in front of the tweezer. This transient can be fitted to an exponential equation, from where its decay time, τ, can be determined.

Now, as the reader may remember, the motion of a particle under Brownian motion and a drag force is described by a Langevin equation [47]:

$$\frac{dx(t)}{dt} = \frac{\kappa}{\gamma}x(t) + \left(\frac{2k_BT}{\gamma}\right)^{\frac{1}{2}}\zeta \tag{4.1}$$

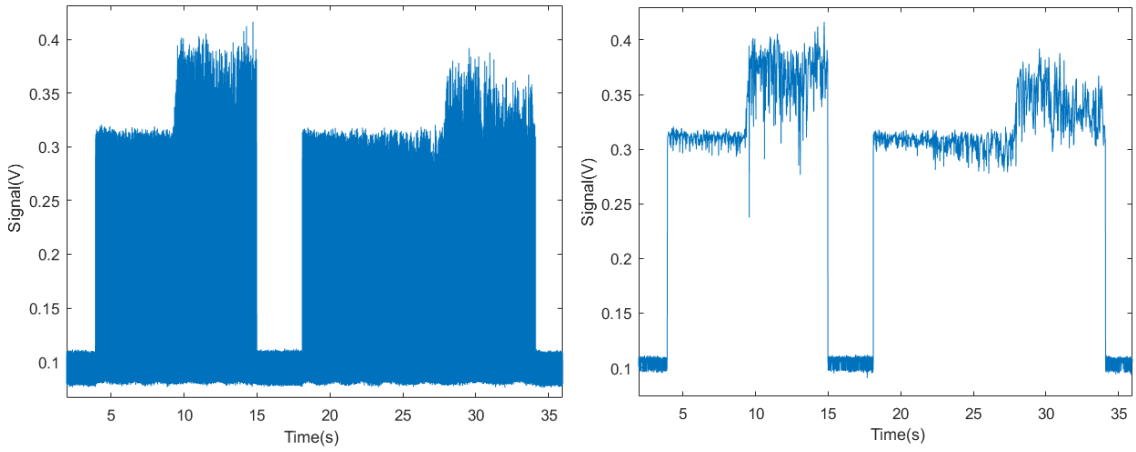
where $x(t)$ is the particle's trajectory, κ is the stiffness of the trap, γ is the Stokes drag coefficient and ζ represents white noise. The following relation can then be taken from here:

$$\tau = \frac{\gamma}{\kappa} \tag{4.2}$$

where the Stokes drag coefficient can be estimated using the Faxen's law, similar to what we have seen in chapter 2:

$$\gamma = \frac{6\pi\eta r}{1 - \frac{9}{16}\left(\frac{r}{h}\right) + \frac{1}{8}\left(\frac{r}{h}\right)^3 - \frac{45}{256}\left(\frac{r}{h}\right)^4 - \frac{1}{16}\left(\frac{r}{h}\right)^5} \tag{4.3}$$

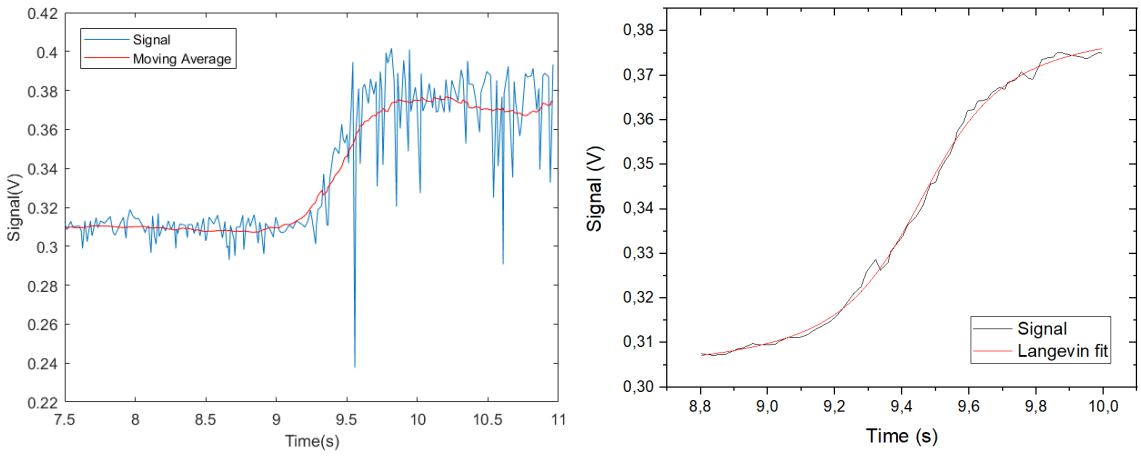
We thus have a way of determining the stiffness of the optical trap from the signal we have collected. This, of course, demands a little manipulation of the data. The signals presented in figures 4.26 and 4.29 have already suffered some processing. Since the laser was modulated using a frequency of 1kHz, it is the envelop of this carried frequency that contains the power fluctuations we wish to monitor - see figure 4.33 (A). However, as we need to fit the signal variation to an exponential curve, we focused our attention in the upper part of the signal, where the signal increases are clear. In order to record the fluctuations, the maxima of the signal were selected, allowing us to perform a fitting of the envelope in the desired section - figure 4.33 (A) (similar to figures 4.26 and 4.29).



(A) (B)

FIGURE 4.33: (A) Signal as collected. (B) Signal processed to present only the variations of the envelope.

A closer look at figures 4.33 (A) and (B) allows us to identify the occurrence of two different trapping events, the first one between 9s and 10s and the second somewhere in between 27s and 30s. These are exactly the sections of the signal we need to analyse. To do so, after selecting the time interval of interest, a matlab pre-defined moving average low pass filter was applied to that signal - see figure 4.34 (A). The moving average was



(A) (B)

FIGURE 4.34: (A) Collected signal of a trapping event (in blue) and the moving average of the signal (red). (B) Langevin fit of the signal from figure (A).

$\kappa_{Tweezer1}\ (fN.nm^{-1})$	$\kappa_{Tweezer5}\ (fN.nm^{-1})$
0.045315	0.035367

TABLE 4.4: Tweezer's stiffness for a power of $4.23mW$ injected into the taper. The tweezer 1 value was determined for a polystyrene particle of $1\mu m$ and the tweezer 5 value for a polystyrene particle of 500 nm.

used to allow for the convergent fit of the data set to an exponential function in Origin software - figure 4.34 (B).

Once the fit was performed, the value for τ was determined, and from the direct use of equation 4.2, the value of trap stiffness could be determined. All trapping events acquired were analysed, and the determined values can be found in table 4.4, and seem to be in accordance with the values presented in reference [94], for a single circular aperture. Be aware that each value not only belongs to a certain tweezer, but it was also determined for a specific particle's diameter. Moreover, if we use them to calculate the force acting on a particle for a given displacement, we find force values within the order of magnitude of those found with the drag force method - about a few dozen femtoNewtons.

4.4 Discussion

In this chapter, we have presented a full description of the fabrication results of the tweezers and of all the difficulties we ran across along the way. We were able to improve the reproducibility of the fibre etching process, to a point where we felt an acceptable taper shape had been achieved, and then carried on to the gold coating and aperture

milling of the tweezer. Due to an experimental limitation, we were only able to open the apertures with a FIB cut made in a transversal direction relative to the tweezer axis. This in terms limited the diameters we were able to work with, since the number of tweezers that made it to the final fabrication step was limited, due to all the equipment constraints we bumped into along the way and the limited time frame.

Nonetheless, even with the limited number of tweezers, we were able to obtain stable trapping of polystyrene particles with diameters of $1\mu m$ and 500 nm. We found force values within the expected order of magnitude and the trap stiffness determined seems to meet the values found in the literature. We have, thus, been able to introduce into the group a new optical trapping technique that will enable us to study a new range of particles.

Chapter 5

Final remarks and future work

The purpose of this thesis was to bring into the investigation group a new technique that would allow the optical trapping and manipulation of sub-micrometre particles. The needs for the introduction of this new technique came from previous work. We were making use of polymeric optical fibre tweezers to trap large particles while simultaneously collecting the radiation those particles reflected into the tip. This allowed us to identify and differentiate particles, as the backscattered radiation is considered a gold-standard technique for single-cell characterization. The problem came when the group started to experiment with exosomes. They are tiny vesicles our cells release and that may help identify different types of tumours, provided we are able to differentiate them. However, they have sizes ranging from 30 to 300 nm, as was already pointed out. For this particle size, polymeric tweezers are no longer able to trap them, and we can only collect the backscattered radiation from the total solution where the exosomes lay. Even though the radiation collected from the solution has proven to suffice in the differentiation of the exosomes, we want to understand if the optical trapping of the specimen can improve that identification and provide for a more robust method.

With the work developed so far, we were able to bring a functioning new technique into the group and successfully trap polystyrene particles as small as 500 nm in diameter. We also demonstrated that even though the apertures are small, they still collect enough backscattered radiation that we can later analyse. Overall, as a preliminary work, we can say it was a success. Notwithstanding, there is still a long way to go. In this short amount of time, and given all the technical problems involved, we were only able to fabricate a very reduced quantity of tapered tweezers, thus limiting the conclusions we were able to reach. Since communications between labs have been established, and equipment has

been fixed, we now have the time and the means to proceed with the fabrication of more and more varied tweezers - in angle and in aperture diameter. With these new tweezers we hope to be able to experiment on a large range of particle's sizes, especially particles with diameters lower than 500 nm and also experimentally verify the influence the taper angle has on the optical force exerted on the particles, something we were not able to do in the domains of this thesis.

The final step would then be to test these tweezers for exosome trapping and backscattered radiation collection and verify if they do improve the technique, providing for better differentiation and, hopefully in the future, for a better diagnostic.

Appendix A

Laser specifications

Parameter	Specification			Unit
Control current range[1,2]	0.015 – 0.5	0.030 – 1.0	0.060 – 2.0	A
Current limit[1,2]	0.2 – 0.5	0.2 – 1.0	0.2 – 2.0	A
Current reading resolution	0.5	1.0	2.0	mA
Compliance voltage	> 4.8			VDC
Photodiode current range[1]	Five ranges from 5 to 5000 (selectable in the software control application)			µA
Maximum TEC current Constant regime Transient regime	 3.0 4.0			 A A
TEC current limit[1]	0.4 – 4.0			A
Modes of operation[1]	(a) Constant average current (b) Constant average output power (c) External modulation (bandwidth 500kHz@3dB for sinusoidal modulation)			- - -
Temperature control loop parameters (Proportional - K_p, and Integral - T_i) [1]	Three ranges (selectable in the software control application)			-
External power supply	+5 VDC, 5A (included)			-
Power consumption	typ. <25			W
Dimensions (WxDxH)	135x200x54			mm
Computer controlled operation – via provided software control application Stand alone operation – via built-in keypad and display				
Built-in USB port – required for initial configuration and computer controlled operation				

(1) User configurable via Software Control Application (GUI)
(2) DIL mount is rated 1A continuous current

FIGURE A.1: Compact Laser Diode Driver (cLDD) specifications.

Bibliography

[1] T. H. Maiman, *Stimulated Optical Radiation in Ruby Masers*, Nature , 493 (1960).

[2] A. Ashkin, *Accelaration and Trapping of Particles by Radiation Pressure*, Physics Review Letters **24**, 156 (1970).

[3] A. Ashkin and J. M. Dziedzic, *Observation of a single-beam gradient force optical trap for dielectric particles*, Optics Letters **11**, 288 (1986).

[4] R. S. R. Ribeiro, R. B. Queirós, C. Ecoffet, O. Soppera, A. Oliva, A. Guerreiro, and P. A. S. Jorge, *Rapid fabrication of polymeric micro lenses for optical fiber trapping and beam shaping*, Proceedings of SPIE (2014).

[5] R. S. R. Ribeiro, R. Queirós, O. Soppera, A. Guerreiro, and P. A. S. Jorge, *Optical Fiber Tweezers Fabricated by Guided Wave Photo-Polymerization*, Photonics , 634 (2015).

[6] R. S. R. Ribeiro, O. Soppera, A. Guerreiro, and P. A. S. Jorge, *Polymeric Optical Fiber Tweezers as a tool for single cell micro manipulation and sensing*, Proc. of SPIE (2015), 24th International Conference on Optical Fibre Sensors.

[7] J. S. Paiva, R. S. R. Ribeiro, J. P. S. Cunha, C. C. Rosa, and P. A. S. Jorge, *Single Particle Differentiation through 2D Optical Fiber Trapping and Back-Scattered Signal Statistical Analysis: An Exploratory Approach*, Sensors **18** (2018).

[8] J. S. Paiva, R. S. R. Ribeiro, P. A. S. Jorge, C. C. Rosa, M. M. Azevedo, P. Sampaio, and J. P. S. Cunha, *Experimental and theoretical evaluation of the trapping performance of polymeric lensed optical fibers: single biological cells versus synthetic structures*, Proc. SPIE (2018), biophotonics: Photonic Solutions for Better Health Care VI.

[9] J. S. Paiva, P. A. S. Jorge, R. S. R. Ribeiro, P. Sampaio, C. C. Rosa, and J. P. S. Cunha, *Optical fiber-based sensing method for nanoparticle detection through supervised*

back-scattering analysis: a potential contributor for biomedicine, International journal of nanomedicine , 2349 (2019).

[10] T. Steinbichler, J. Dudás, H. Riechelmann, and I. Skvortsova, *The role of exossomes in cancer metastasis*, Seminars is cancer biology , 170 (2017).

[11] J. Welsh, J. Holloway, J. Wilkinson, and N. Enlyst, *Extracellular vesicle flow cytometry analysis and standardization*, Frontiers in Cell and Developmental Biology **5** (2017).

[12] H. Zhang, D. Freitas, and H. S. K. et al, *Identification of distinct nanoparticles and subsets of extracellular vesicles by asymmetric field-flow fractionation*, Nature Cell Biology **20** (2018).

[13] K. C. Neuman and S. M. Black, *Optical trapping*, Review of Scientific Instruments **75** (2004).

[14] A. Ashkin, *Forces of a single-beam gradient laser trap on a dielectric sphere in the ray optics regime*, Biophys. J. , 569 (1992).

[15] R. S. R. Ribeiro, *Optical fiber tools for single cell trapping and manipulation*, Ph.D. thesis, Faculdade de Ciências da Universidade do Porto (2017).

[16] *Modular Tweezers OTKB(/M) User Guide*, Thorlabs (2018).

[17] M. Sarshar, W. T. Wong, and B. Anvari, *Comparative study of methods to calibrate the stiffness of a single-beam gradient-force optical tweezers over various laser trapping powers*, Journal of Biomedical Optics **19(11)**, 115001 (2014).

[18] N. Malagnino, G. Pesce, A. Sasso, and E. Arimondo, *Measurements of trapping efficiency and stiffness in optical tweezers*, Optics Communications **214**, 15 (2002).

[19] A. van der Horst and N. R. Forde, *Power spectral analysis for optical trap stiffness calibration from high-speed camera position detection with limited bandwidth*, Optics Express **18**, 7670 (2010).

[20] L. Novotny and B. Hecht, *Principles of Nano-Optics* (Cambridge University Press, 2012) 2nd edition.

[21] K. Svoboda and S. M. Block, *Optical trapping of Rayleigh particles*, Optics Letters **19**, 930 (1994).

[22] L. Bosanac, T. Aabo, P. M. Bendix, and L. B. Oddershede, *Efficient Optical Trapping and Visualization of Silver Nanoparticles*, Nano Letters **8**, 1486 (2008).

[23] J. K. C. Toussaint, M. Liu, M. Pelton, J. Pesic, M. J. Guffey, P. Guyot-Sionnest, and N. F. Scherer, *Plasmon resonance-based optical trapping of single and multiple Au nanoparticles*, Optics Express **15**, 12017 (2007).

[24] C. Selhuber-Unkel, I. Zins, O. Schubert, C. Sonnichsen, and L. B. Oddershede, *Quantitative optical trapping of single gold nanorods*, Nano Letters **8**, 2998 (2008).

[25] L. Jauffred, A. C. Richardson, and L. B. Oddershede, *Three-dimensional optical control of individual quantum dots*, Nano Letters **8**, 3376 (2008).

[26] O. M. Maragò, P. G. Gucciardi, F. Bonaccorso, G. Calogero, *et al.*, *Optical trapping of carbon nanotubes*, Physica E **40**, 2347 (2008).

[27] Y. Pang and R. Gordon, *Optical trapping of a single protein*, Nano Letters **12**, 402 (2012).

[28] S. Wheaton and R. Gordon, *Molecular weight characterization of single globular proteins using optical nanotweezers*, Analyst **140**, 4799 (2015).

[29] A. Kotnala and R. Gordon, *Double nanohole optical tweezers visualize protein p53 unzipping of single DNA-hairpins*, Biomedical Optics Express **13**, 1886 (2014).

[30] A. A. A. Balushi, A. Zehtabi-Oskuie, and R. Gordon, *Observing single protein binding by optical transmission through a double nanohole aperture in a metal film*, Biomedical Optics Express **4**, 1504 (2013).

[31] O. M. Maragò, P. H. Jones, P. G. Gucciardi, G. Volpe, and A. C. Ferrari, *Optical trapping and manipulation of nanostructures*, Nature Nanotechnology **8**, 807 (2013).

[32] S. Kawata and T. Sugiura, *Movement of micrometer-sized particles in the evanescent field of a laser beam*, Optics Letters **17**, 772 (1992).

[33] L. Novotny, R. X. Bian, and X. S. Xie, *Theory of Nanometric Optical Tweezers*, Physical Review Letters **79**, 645 (1997).

[34] K. Okamoto and S. Kawata, *Radiation Force Exerted on Subwavelength Particles near a Nanoaperture*, Physical Review Letters **83**, 4534 (1999).

[35] G. Volpe, R. Quidant, G. Badenes, and D. Petrov, *Surface Plasmon Radiation Forces*, Physical Review Letters **96**, 238101 (2006).

[36] R. Quidant, D. Petrov, and G. Badenes, *Radiation forces on a Rayleigh dielectric sphere in a patterned optical near field*, Optics Letters **30**, 1009 (2005).

[37] M. Sergides, V. G. Truong, and S. N. Chormaic, *Highly tunable plasmonic nanoring arrays for nanoparticle manipulation and detection*, Nanotechnology **27**, 365301 (2016).

[38] M. Righini, P. Ghenuche, S. Cherukulappurath, V. Myroshnychenko, F. J. G. de Abajo, and R. Quidant, *Nano-optical trapping of Rayleigh particles and escheria coli bacteria with resonant optical antennas*, Nano Letters **9**, 3387 (2009).

[39] A. N. Grigorenko, N. W. Roberts, M. R. Dickinson, and Y. Zhang, *Nanometric optical tweezers based on nanostructured substrates*, Nature Photonics **2**, 365 (2008).

[40] X. Han, V. G. Truong, and S. N. Chormaic, *Nano-ring arrays for sub-micron particle trapping*, Proc. of SPIE **10252**, 102520R (2017).

[41] K. Wang, E. Schonbrun, P. Steinvurzel, and K. B. Crozier, *Scannable plasmonic trapping using a gold stripe*, Nano Letters **10**, 3506 (2010).

[42] M. L. Juan, M. Righini, and R. Quidant, *Plasmon nano-optical tweezers*, Nature Photonics **5**, 349 (2011).

[43] W. Zhang, L. Huang, C. Santschi, and O. J. F. Martin, *Trapping and sensing 10 nm metal nanoparticles using plasmonic dipole antennas*, Nano Letters **10**, 1006 (2010).

[44] B. J. Roxworthy, K. D. Ko, A. Kumar, K. H. Fung, *et al.*, *Application of plasmonic bowtie nanoantenna arrays for optical trapping, stacking, and sorting*, Nano Letters **12**, 796 (2011).

[45] M. L. Juan, R. Gordon, Y. Pang, F. Eftekhari, and R. Quidant, *Self-induced back-action optical trapping of dielectric nanoparticles*, Nature Physics **5**, 915 (2009).

[46] R. Gordon, *Biosensing with nanoaperture optical tweezers*, Optics and Laser Technology **109**, 328 (2019).

[47] A. Kotnala and R. Gordon, *Quantification of high-efficiency trapping of nanoparticles in a double nanohole optical tweezer*, Nano Letters **14**, 853 (2014).

[48] N. M. Hameed, A. E. Eter, T. Grosjean, and F. I. Baida, *Stand-alone three-dimensional optical tweezers based on fibred bowtie nanoaperture*, IEEE Photonics Journal **6**, 4500510 (2014).

[49] E. Kwak, T. Onuta, D. Amarie, R. Potyrailo, *et al.*, *Optical Trapping with Integrated Near-Field Apertures*, J. Phys. Chem. B **108**, 13607 (2004).

[50] Y. Pang and R. Gordon, *Optical trapping of 12 nm dielectric spheres using double-nanoholes in a gold film*, Nano Letters **11**, 3763 (2011).

[51] N. Hacohen, C. J. X. Ip, and R. Gordon, *Analysis of egg white protein composition with double nanohole optical tweezers*, ACS Omega **3**, 5266 (2018).

[52] M. Braibanti, D. Vigolo, and R. Piazza, *Does thermophoretic mobility depend on particle size?*, Physical Review Letters **100**, 108303 (2008).

[53] J. Wu and X. Gan, *Three dimensional nanoparticle trapping enhanced by surface plasmon resonance*, Optics Express **19**, 27619 (2010).

[54] K. Wang, E. Schonbrun, P. Steinvurzel, and K. B. Crozier, *Trapping and rotating nanoparticles using a plasmonic nano-tweezer with an integrated heat sink*, Nature Communications **2**, 469 (2011).

[55] A. H. J. Yang, S. D. Moore, B. S. Schmidt, M. Klug, M. Lipson, and D. Erickson, *Optical manipulation of nanoparticles and biomolecules in sub-wavelength slot waveguides*, Nature Letters **457**, 71 (2009).

[56] F. Vollmer, S. Arnold, and D. Keng, *Single virus detection from the reactive shift of a whispering-gallery mode*, PNAS **105**, 20701 (2008).

[57] J. M. Ward, Y. Yang, and S. N. Chormaic, *Nanoparticle trapping and control in a hollow whispering gallery resonator*, Proc. of SPIE **10252**, 102520X (2017).

[58] S. Arnold, D. Keng, S. I. Shopova, S. Holler, W. Zurawsky, and F. Vollmer, *Whispering gallery mode carousel - a photonic mechanism for enhanced nanoparticle detection in biosensing*, Optics Express **17**, 6230 (2009).

[59] G. Zhang, Z. Zhu, Y. Li, G. Xia, and Q. Lin, *Numerical analysis of near-field optical trapping using tapered fiber probe*, Proceedings of SPIE **4082**, 321 (2000).

[60] L. Novotny and C. Hafner, *Light propagation in a cylindrical waveguide with a complex, metallic, dielectric function*, Physical Review E **50**, 4094 (1994).

[61] B. Hecht, B. Sick, U. P. Wild, V. Deckert, R. Zenobi, O. J. F. Martin, and D. W. Pohl, *Scanning near-field optical microscopy with aperture probes: Fundamentals and applications*, Journal of Chemical Physics **112**, 7761 (2000).

[62] L. Novotny, D. W. Pohl, and B. Hecht, *Scanning near-field optical probe with ultrasmall spot size*, Optics Letters **20**, 970 (1995).

[63] C. Bouwkamp, *On Bethe's theory of diffraction by small holes*, Philips Research Reports **5**, 321 (1950).

[64] J. Tinguely, M. Ding, G. Brambilla, A. Hohenau, J. R. Krenn, and O. G. Helleso, *Nanostructured fibre tip for trapping of nanoparticles*, Proc. of SPIE **8999**, 89991D (2014).

[65] J. Berthelot, S. S. Acimovic, M. L. Juan, M. P. Kreuzer, J. Renger, and R. Quidant, *Three-dimensional manipulation with scanning near-field optical nanotweezers*, Nature Nanotechnology **9**, 295 (2014).

[66] A. E. Eter, N. M. Hameed, F. I. Baida, R. Salut, *et al.*, *Fiber-integrated optical nanotweezer based on a bowtie-aperture nano-antenna at the apex of a SNOM tip*, Optics Express **22**, 10072 (2014).

[67] R. M. Gelfand, S. Wheaton, and R. Gordon, *Cleaved fiber optic double nanohole optical tweezers for trapping nanoparticles*, Optics Letters **39**, 6415 (2014).

[68] T. W. Ebbesen, H. J. Lezec, H. F. Ghaemi, T. Thio, and P. A. Wolff, *Extraordinary optical transmission through sub-wavelength hole arrays*, letters to nature **391**, 667 (1998).

[69] F. Medina, J. A. Ruiz-Cruz, F. Mesa, J. M. Rebollar, J. R. Montejo-Garai, and R. Marqués, *Experimental verification of extraordinary transmission without surface plasmons*, Appl. Phys. Lett. **95**, 071102 (2009).

[70] L. Neumann, Y. Pang, A. Houyou, M. L. Juan, R. Gordon, and N. F. van Hulst, *Extraordinary optical transmission brightens near-field fiber probe*, Nano Letters **11**, 355 (2011).

[71] J. M. Ehtaiba and R. Gordon, *Template-stripped nanoaperture tweezer integrated with optical fiber*, Optics Express **26**, 9607 (2018).

[72] D. R. Turner, "Etch procedure for optical fibers," United State patent (1984).

[73] Y. Zaatar, D. Zaouk, J. Bechara, A. Khoury, C. Llinaress, and J.-P. Charles, *Fabrication and characterization of an evanescent wave fiber optic sensor for air pollution control*, Material Science and Engineering B **74**, 296 (2000).

[74] D. J. Monk, D. S. Soane, and R. T. Howe, *A review of the chemical reaction mechanism and kinetics for hydrofluoric acid etching of silicon dioxide for surface micromachining applications*, Thin Solid Films **232**, 1 (1993).

[75] H. S. Haddock, P. M. Shankar, and R. Mutharasan, *Fabrication of biconical tapared optical fibers using hydrofluoric acid*, Material Science and Engineering B **97**, 87 (2003).

[76] K. M. Takahashi, *Meniscus shapes on small diameter fibers*, Journal of Colloid and Interface Science **134**, 181 (1990).

[77] A. Sayah, C. Philipona, P. Lambelet, M. Pfeffer, and F. Marquis-Weible, *Fiber tips for scanning near-field optical microscopy fabricated by normal and reverse etching*, Ultramicroscopy **71**, 59 (1998).

[78] Z. Wang and Z. Zhang, *Electron Beam Evaporation Deposition* (In Advanced Nano Deposition Methods (eds. Y. Lin and X. Chen), 2016).

[79] K. S. S. Harsha, *Principles of Physical Vapor Deposition of Thin Films* (Elsevier, 2006) 1st edition.

[80] *BOC Edwards Auto 306 E-beam Evaporator Operating Instructions*, Edwards, rev. 1 ed. (2008).

[81] *Helios NanoLab 450S Product Data*, FEI, ds0071 04-10 ed. (2010).

[82] L. Reimer, *Scanning electron microscopy: Physics of image formation and microanalysis*, 2nd ed., Vol. 45 (Springer, 1998).

[83] K. Svoboda and S. M. Block, *Biological applications of optical forces*, Annual Review of Biophysics and Biomolecular Structure **23**, 247 (1994).

[84] I. F. Sbalzarini and P. Koumoutsakos, *Feature point tracking and trajectory analysis for video imaging in cell biology*, Journal of structural biology **151**, 182 (2005).

[85] *COMSOL Multiphysics User's Guide*, COMSOL, 4th ed. (2012).

[86] R. S. R. Ribeiro, P. A. S. Jorge, and A. Guerreiro, *Computational Models for New Fiber Optic Tweezers*, Photonic Sensors **3**, 57 (2013).

[87] R. S. R. Ribeiro, P. A. S. Jorge, and A. Guerreiro, *New developments on the design and modeling of fiber optical tweezers*, 8th Iberoamerican Optics Meeting and 11th Latin American Meeting on Optics, Lasers, and Applications **Proc. of SPIE Vol. 8785**, 8785F9 (2013).

[88] S. M. Barnett and R. Loudon, *On the electromagnetic force on a dielectric medium*, J. of Phys. B: At. Mol. Opt. Phys. **39**, S671 (2006).

[89] L. Novotny, D. W. Pohl, and P. Regli, *Light propagation through nanometer-sized structures: the two-dimensional-aperture scanning near-field optical microscope*, J. Opt. Soc. Am. A **11**, 1768 (1994).

[90] J. D. Jackson, *Classical Electrodynamics* (John Wiley Sons Inc, 1999) 3rd edition.

[91] J. Vancea, G. Reiss, F. Schneider, K. Bauer, and H. Hoffmann, *Substrate effects on the surface topography of evaporated gold films - A scanning tunneling microscopy investigation*, Surface Science **218**, 108 (1989).

[92] R. Stockle, C. Fokas, V. Deckert, R. Zenobi, B. Sick, B. Hecht, and U. P. Wild, *High-quality near-field optical probes by tube-etching*, Appl. Phys. Lett. **75**, 160 (1999).

[93] R. Xu, *Principle characterization: light scattering methods*, Vol. 13, Particle Technology Series (Springer Science & Business Media, 2001).

[94] R. M. Simmons, J. T. Finer, S. Chu, and J. A. Spudich, *Quantitative measurements of force and displacement using an optical trap*, Biophysical Journal **70**, 1813 (1996).